THESIS

DEVELOPMENT OF A POLARIMETRIC RADAR BASED HYDROMETEOR CLASSIFICATION ALGORITHM FOR WINTER PRECIPITATION

Submitted by

Elizabeth Jennifer Thompson

Department of Atmospheric Science

In partial fulfillment of the requirements

For the Degree of Masters of Science

Colorado State University

Fort Collins, Colorado

Fall 2012

Master's Committee:

Advisor: Steven A. Rutledge

Brenda Dolan
V. Chandrasekar
Susan van den Heever

ABSTRACT

DEVELOPMENT OF A POLARIMETRIC RADAR BASED HYDROMETEOR CLASSIFICATION ALGORITHM FOR WINTER PRECIPITATION

The nation-wide WSR-88D radar network is currently being upgraded for dual-polarized technology. While many convective, warm-season fuzzy-logic hydrometeor classification algorithms based on this new suite of radar variables and temperature have been refined, less progress has been made thus far in developing hydrometeor classification algorithms for winter precipitation. Unlike previous studies, the focus of this work is to exploit the discriminatory power of polarimetric variables to distinguish the most common precipitation types found in winter storms without the use of temperature as an additional variable. For the first time, detailed electromagnetic scattering of plates, dendrites, dry aggregated snowflakes, rain, freezing rain, and sleet are conducted at X-, C-, and S-band wavelengths. These physics-based results are used to determine the characteristic radar variable ranges associated with each precipitation type. A variable weighting system was also implemented in the algorithm's decision process to capitalize on the strengths of specific dual-polarimetric variables to discriminate between certain classes of hydrometeors, such as wet snow to indicate the melting layer.

This algorithm was tested on observations during three different winter storms in Colorado and Oklahoma with the dual-wavelength X- and S-band CSU-CHILL, C-band OU-PRIME, and X-band CASA IP1 polarimetric radars. The algorithm showed success at all three frequencies, but was slightly more reliable at X-band because of the algorithm's strong dependence on K_{DP}. While plates were rarely distinguished from dendrites, the latter were

satisfactorily differentiated from dry aggregated snowflakes and wet snow. Sleet and freezing rain could not be distinguished from rain or light rain based on polarimetric variables alone. However, high-resolution radar observations illustrated the refreezing process of raindrops into ice pellets, which has been documented before but not yet explained. Persistent, robust patterns of decreased ρ_{HV}, enhanced Z_{DR}, and an inflection point around enhanced Z_H occurred over the exact depth of the surface cold layer indicated by atmospheric soundings during times when sleet was reported at the surface. It is hypothesized that this refreezing signature is produced by a modulation of the drop size distribution such that smaller drops preferentially freeze into ice pellets first. The melting layer detection algorithm and fall speed spectra from vertically pointing radar also captured meaningful trends in the melting layer depth, height, and mean ρ_{HV} during this transition from freezing rain to sleet at the surface. These findings demonstrate that this new radar-based winter hydrometeor classification algorithm is applicable for both research and operational sectors.

ACKNOWLEDGEMENTS

First and foremost, I would like to thank my advisor, Dr. Steven Rutledge, for this learning opportunity as well as his enthusiasm and leadership. I am extremely grateful for Dr. Brenda Dolan because of the generosity with which she shared her expertise, experience, sense of humor, and time with me. The data processing and interpretation provided by Dr. V. Chandrasekar and his students, including Mr. Haonan Chen, were invaluable to the completion of this project. Thanks to Dr. Susan van den Heever as well for her tutoring both in and out of the classroom. In particular, we shared many conversations that helped me understand the context and potential impact of this work within the greater scientific community.

I thank Dr. Boon Leng Cheong for providing OU-PRIME data. OU-PRIME is maintained and operated by the Advanced Radar Research Center (ARRC) of the University of Oklahoma. I also acknowledge Mr. Patrick C. Kennedy (CSU-CHILL National Weather Radar Facility) for providing CHILL radar data in addition to assistance with data processing and correction techniques. Paul Hein (CSU) supplied invaluable encouragement as well as technical help with management and processing of radar data. Useful discussions with Dr. Earle Williams (MIT) and Dr. Raquel Evaristo (Valparaiso University) helped clarify several aspects of my analysis and results. Conversations with my research group members and classmates were also greatly appreciated, particularly with Dr. Nick Guy, Dr. David Lerach, Dr. Angela Rowe, and Mr. Ted Letcher. Finally, thanks to many family members and friends for direct and indirect support throughout this process.

This work was supported primarily by the National Science Foundation Engineering Research Center for Collaborative Adaptive Sensing of the Atmosphere subcontract UM#04-

002341 B10 PO0001203233 from the University of Massachusetts. Any opinions, findings, conclusions, or recommendations expressed in this material are those of the authors and do not necessarily reflect those of the National Science Foundation. A Graduate Research Fellowship from the American Meteorological Society provided additional funding.

TABLE OF CONTENTS

CHAPTER ONE

Introduction

1.1 Polarimetric radar properties of winter storms

Reducing uncertainty associated with winter storm precipitation type, accumulation and timing is a paramount forecasting challenge (Ralph et al. 2005). These rapidly evolving mesoscale systems (usually as part of extratropical cyclones) will be better understood with the national dual-polarized radar upgrade through use of fuzzy-logic hydrometeor identification (Liu and Chandrasekar 2000). Cold season microphysical processes observable by dual-polarized radars and whose origins are generally well agreed upon include dendritic ice crystal growth (Kenndey and Rutledge 2011), ice particle density and shape modulations caused by riming and aggregation (Vivekanandan et al. 1994), as well as hydrometeor melting (Ryzhkov et al. 1998). While radar signatures of freezing rain and sleet have not been identified prior to this study, the near-surface phase change from either rain or freezing rain to sleet is discernable with polarimetric radars (Ryzhkov et al. 2011). However, the physical explanation for this refreezing signature is still unknown.

Information about the distribution of sizes, orientations, shapes, and diversity of hydrometeors within a particular radar bin can be garnered from the differential reflectivity (Z_{DR}), correlation coefficient (ρ_{HV}), and specific differential phase (K_{DP}) (Straka et al. 2000, Bringi and Chandrasekar 2001). The radar reflectivity factor (Z_H) also gives an indication of hydrometeor size and concentration. This thesis focuses on automatically classifying the dominant winter hydrometeor types/processes based on the discriminatory power of these polarimetric radar variables, which are explained in more detail in Section 1.4.

1.2 Purpose of hydrometeor classification studies

There are several motivations for discriminating hydrometeor types and precipitation transition processes with radar. One of the leading weather-related safety (Smith et al. 2012) and socioeconomic (Nygaard et al. 2011) hazards is aircraft icing in freezing temperatures when the air is saturated with respect to water. Radar detection of dendritic ice crystals, which also require this level of saturation, provides a necessary but insufficient indicator of super cooled liquid water (SCLW). Plate crystals grow at the same temperature ranges as dendrites but when the air is *unsaturated* with respect to water, so remote sensing discrimination between plates and dendrites could potentially characterize the environment's saturation level (Williams et al. 2011). Most weather radars are incapable of directly sensing super cooled liquid drops due to their long wavelength relative to typical drop diameters (< 0.5 mm). SCLW also often exist simultaneously with larger ice crystals that dominate the returned radar signal. Satellites and space-borne cloud radars are better suited for SCLW detection, but only on spatial scales as fine as the entire radar domain. This is inadequate for making local aircraft operation decisions.

A second winter hazard addressed by hydrometeor identification algorithms is enhanced production and subsequent aggregation of dendritic crystals aloft. More numerous large crystals resulting from these processes can lead to heavy surface precipitation rates, degradation of visibility, and disruptive snowfall accumulations (Fujiyoshi and Wakahama 1985, Kennedy and Rutledge 2011). Z_H-snowfall relationships for quantitative precipitation estimation/forecasts and ice water content calculations may also be improved if the winter hydrometeor type is first determined (Vivekanandan et al. 1994, Mitchell et al. 1996, Wolfe and Snider 2012). The variable density of ice crystals is a major source of uncertainty in these techniques.

Routine, nation-wide dual-polarized radar observations that resolve cloud microphysical processes and discriminate winter precipitation type will also provide a foundation for evaluating and improving semi-melted/frozen hydrometeor microphysical parameterization schemes in numerical models (Cotton et al. 2011). Secondary ice formation processes are currently not well understood, measured, or represented in weather prediction models (Baumgardner et al. 2012, Thériault et al. 2006). The radar-derived vertical distribution, prevalence, and partitioning of ice and liquid species in clouds could be assimilated into these numerical models for better performance. Realistic simulations of warm- and cold-season weather systems require proper representation of mixed-phase precipitation in the model framework (Cotton et al. 2011). Knowledge of ice species within clouds gained from dual-polarized radars could also help evaluate cloud radiative properties and therefore climate feedbacks (Stephens 2005).

Finally, the potential socioeconomic impacts and safety concerns associated with rain, freezing rain, and sleet are drastically different but the thermodynamic processes determining this precipitation transition are incredibly subtle (Ralph et al. 2005). Freezing rain produces a severe safety hazard to transportation and can topple trees and power lines from the weight and brittleness of glaciated ice (Cortinas et al. 2004). Conversely, sleet produces a much more muted socioeconomic impact, but one that is still greater than snow because accumulation of dense, high water content, frozen slush is difficult to remove (Gibson et al. 2009). The range of these hazards depends upon many competing, multiscale factors. These include the depth and temperature of the surface cold and elevated warm layers organized on the synoptic scale, mesoscale circulations and gradients of humidity and temperature, and the microscale latent heating caused by melting, refreezing, and evaporation (Stewart et al. 1990b). Rauber et al. (2001) suggest that the key to developing a mixed-phase precipitation forecast is to incorporate

more complex phase change physics, including the effect of different ice particle habits falling through the melting layer.

Hydrometeor classification can also elucidate the connection between winter storm kinematics and thermodynamics. Some studies have hypothesized that dendritic growth and the existence of supercooled water are both controlled by a critical minimum updraft speed under proper temperature and moisture conditions (Auer and White 1982, Rauber and Tokay 1991). Parcels will moisten adiabatically during ascent, perhaps raising the saturation level enough to support rapid depositional growth. If small ice particles cannot accommodate the excess vapor, super cooled liquid water drops may form near cloud top. Vertical velocities within these regions can be derived with the horizontal wind fields from two or more Doppler radars (Davies-Jones 1979). Hydrometeor classification and dual- or triple-Doppler wind fields from the CASA IP1 X-band radar network (Dolan and Rutledge 2010) used in this study could help characterize the relationship between updraft speed and dendritic growth zones. Fall speed spectra from vertically pointing radars can also help identify regions where particles are melting, aggregating, and riming (Chandrasekar et al. 2011).

1.3 Thesis objectives

This study focuses on radar classification of winter storm hydrometeor type since surface mesonet and automated surface observing stations (ASOS), rapidly disseminated model output, and upper-air soundings cannot discriminate between different snow crystal types, rain, freezing rain, or sleet with much confidence for several reasons. ASOS instruments lack heated, tipping rain buckets so they do not autonomously measure or discriminate between semi- or completely frozen precipitation. Nearby stations often disagree greatly, contrary to coincident human

observations (Elmore et al. 2011). Sounding and forecast model output also lack spatiotemporal resolution on scales necessary to detect low-level, local, rapidly evolving precipitation type and intensity transitions. These methods also do not indicate which hydrometeor types may exist aloft, which certainly has implications for determining surface weather conditions.

Hydrometeor classification algorithms using atmospheric soundings with X-, C-, and S-band polarimetric radar observations have been successful for warm-season, convective precipitation (Liu and Chandrasekar 2000, Zrnic et al. 2001, Ryzhkov et al. 2005a, Dolan and Rutledge 2009, Park et. al 2009, Chandrasekar et al. 2011). An atmospheric sounding is mostly sufficient to describe thermodynamic conditions relevant to hydrometeor classification in this meteorological regime because the freezing level does not vary much in space or time. This is not the case for winter precipitation though, which has motivated use of a polarimetric radar based melting layer detection algorithm and perhaps additional steps to discern precipitation types below and above this bright band layer (Giangrande et al. 2004, Boodoo et al. 2010).

To date, wintertime polarimetric algorithms using a radar-based melting layer detection algorithm and external temperature information from either a sounding or numerical model forecast have attempted to identify winter storm hydrometeor types with varying levels of success (Kouketsu and Uyeda 2010, Elmore et al. 2011, Schuur et al. 2012). Elmore et al. (2011) showed that the radar's inability to identify the refreezing of raindrops and errors in the melting layer detection algorithm led to HCA failures and poor overall performance. Schuur et al. (2012) produced satisfactory results using an algorithm based on Rapid Update Cycle (RUC) model output temperature and moisture fields along with dual-polarized radar data. The methodology presented in Schuur et al. (2012) is particularly valuable in regions beyond the radar domain, at far ranges where the radar resolution is degraded, and below the lowest elevation angle scan

where surface weather conditions cannot be diagnosed by the radar at all. However, this study did not explore classification of various snow types such as dendrites, plates, and dry aggregated snowflakes. The recently discovered refreezing signature has not been implemented into a hydrometeor classification scheme either. It is important to note that both of these phenomena have been validated with external temperature in previous studies (Kennedy and Rutledge 2011, Ryzhkov et al. 2011), but they do not require temperature information for detection in real-time. Furthermore, none of these previous winter HCA studies have fully exploited the potential uses of K_{DP} (especially at shorter radar wavelengths), which is extremely useful for distinguishing different ice crystal habits.

Polarimetric signatures of various winter storm types/processes can be determined from theoretical electromagnetic scattering simulations, tested with radar observations, and validated with external temperature sources. Without in-situ observations of hydrometeor types from ground-based or aircraft data to compare with radar observations, this is the most objective methodology for building a robust HCA. Previous winter HCAs could then be greatly improved if these derived polarimetric signatures prove robust enough to not require temperature for real-time detection (Zrnic et al. 2001). This approach is potentially very valuable since temperature information is not available at the same update frequency or spatial scale as radar data, which refreshes approximately every 5-10 minutes for domains ranging 100-250 km. Special soundings and fine scale model output can also be expensive and time consuming to acquire and use, whereas dual-polarized radars provide pertinent temperature information with a melting level detection algorithm at no additional cost.

After identifying several steps of worthy research from this literature review, the three main hypotheses of this thesis are:

1) Dual-polarimetric radar signatures of winter storms are sufficient to identify the dominant classes of frozen and melting hydrometeors as well as the microphysical processes governing the near surface transition between frozen and liquid precipitation types *without the use of external temperature information*.
2) When combined with radial velocity spectra from vertically pointing radar, the microphysical information gained from a hydrometeor classification algorithm could further elucidate precipitation processes such as ice crystal growth, riming, melting and aggregation.
3) Shorter wavelength dual-polarimetric radars are superior to longer wavelength systems for determination of winter storm hydrometeor type when using K_{DP} since this variable scales inversely with wavelength.

In order to develop such a hydrometeor classification algorithm, scattering simulations of dual-polarimetric variables at X-, C-, and S-band wavelengths based on the physical properties of dendrites, plates, dry aggregated snow, rain, freezing rain, and sleet are performed and discussed in Chapter 2. We build a melting layer detection and hydrometeor classification algorithm based on these theoretical results in Chapter 3. Chapter 4 uses these algorithms to explore precipitation microphysical processes observed during three different winter storms that exhibited a melting zone, precipitation transition zone, dendritic growth zone, and refreezing zone (freezing of liquid drops into ice pellets near the surface). Chapter 5 discusses the operational viability of this hydrometeor classification algorithm at various wavelengths as well as the microphysical conclusions drawn from this new radar analysis on winter storms.

1.4 Explanation of radar variables

Under simplified Rayleigh scattering conditions, the radar reflectivity factor (Z_H) increases with number concentrations and drop diameter according to equation (1), where N_i is the particle concentration of drops with diameter D_i. Subscripts (H,V) denote the transmitted and received polarization, respectively. Z_H is strongly weighted by the size and density of the largest particles (Vivekanandan et al. 1994). Conversion to logarithmic units of dBz is accomplished by taking $10\log_{10}(Z_H)$ in (1).

(1) $Z_H = Z_{HH} = \sum_{i=1}^{n} N_i D_i^6 \quad (\mathrm{mm}^6\,\mathrm{m}^{-3})$ (Bringi and Chandrasekar 2001: Eq. 3.166)

As precipitation particles intercept electromagnetic radiation in both the horizontal and vertical direction, a differential phase shift and/or differential power return may occur between each polarization channel. Differential reflectivity is calculated as (2), and indicates whether a population of hydrometeors is mostly oblate ($Z_{DR} > 0$), prolate ($Z_{DR} < 0$), or spherical ($Z_{DR} \sim 0$).

(2) $Z_{DR} = 10 \log_{10} [Z_{HH} / Z_{VV}]$ (Selinga and Bringi 1976)

It is important to note that equations (1) and (2) are derived from Rayleigh scattering assumptions for spherical targets, but Rayleigh-Gans theory demonstrates that both Z_H and Z_{DR} still depend on the density and phase of oblate hydrometeors through the dielectric factor, K (Atlas et al. 1953). The power received by the radar is proportional to the modulus of K, or $|K|^2$ (Bringi and Chandrasekar 2001).

An oblate particle will also produce a larger phase shift in the horizontal polarization than the vertical. This produces a positive differential propagation phase shift (ϕ_{DP} in units of degrees) across the range gate as expressed in (3).

(3) $\phi_{DP} = \phi_{HH} - \phi_{VV}$ (Rhinehart 2004: Eq. 10.5)

Apart from non-Rayleigh scattering, which causes additional phase fluctuations by contributions from the backscattering differential phase (δ), the range (r in km) derivative of ϕ_{DP} can be calculated as the specific differential phase, K_{DP}, according to (4).

(4) $$K_{DP} = \frac{\phi_{DP}(r_2) - \phi_{DP}(r_1)}{2(r_2 - r_1)}$$ (Hubbert and Bringi 1995)

K_{DP} is expressed in terms of degrees of phase shift per kilometer along the radar beam. It can also be derived as the product of rain water content (W in units of g m^{-3}) and the deviation of the mass-weighted mean axis ratio ($\bar{r}$) from unity, as shown in (5) where $C \sim 3.75$ for liquid hydrometeors. This relationship also illustrates K_{DP}'s inverse relationship to the radar wavelength, λ, in meters.

(5) $$K_{DP} = \frac{180}{\lambda}\ 10^{-3}\ C\ W\ (1 - \bar{r}\ )$$ (Bringi and Chandrasekar 2001: Eq. 7.17)

W is given by (6) where ρ_W is the density of water in g m^{-3}.

(6) $$W = \frac{\pi}{6}\ \rho_W \int_0^{\infty} D^3\ N(D)\ dD$$ (Bringi and Chandrasekar 2001: Eq. 7.11)

For ice particles, (7) is used, where ρ_p is the assumed ice particle bulk density, $C \sim 1.6$, IWC is the ice water content, and r is the axis ratio (a/b) of the minor (vertical) to the major (horizontal) particle dimensions ranging from [0,1].

(7) $$K_{DP} = 10^{-3}\ \frac{180}{\lambda}\ \rho_p\ C\ (IWC)\ (1 - r)$$ (Bringi and Chandrasekar 2001: Eq. 7.101)

Positive K_{DP} is produced in regions of the cloud where high water content and/or oblate particles exist. Vertically aligned ice crystals, sometimes indicative of strong electric fields, cause K_{DP} and $Z_{DR} < 0$ (Carey and Rutledge 1998).

Specific differential phase is immune to radar calibration, so this variable is often used to improve attenuation correction, rainfall, and ice water content estimation methods (Ryzhkov et al. 1998, Bringi and Chandrasekar 2001). K_{DP} calculation is difficult and not widely available though so its use in weather phenomenon studies is less documented relative to Z_{DR} and ρ_{HV} (discussed below). Moreover, K_{DP} values at S-band are limited to a small magnitude due to its inverse wavelength dependence, which makes K_{DP} seem less informative for operational (S-bamd) forecasting purposes. However, this argument also provides that K_{DP} is about 3 times greater at X-band (3.2 cm) than at S-band (11 cm) for a given precipitation type, which helps distinguish meteorological values from background noise. This study explores the use of K_{DP} in a hydrometeor classification algorithm (HCA) at X-, C- (5.5 cm), and S-band wavelengths.

The co-polar correlation coefficient, ρ_{HV}, between copolar H and V channels gives a measure of particle shape, composition, and size diversity within the radar bin according to (8). Elements of the radar covariance matrix for each transmitted and received polarization are expressed by permutations of S while n represents the number of particles per unit volume.

$$(8)\ |\rho_{HV}| = \frac{| < n\, S_{HH} S_{VV}^{*} > |}{(< n\, |S_{HH}|^2 > < n\, |S_{VV}|^2 >)^{1/2}} \qquad \text{(Ryzhkov 2001)}$$

The numerator of (8) increases as S_{HH} and S_{VV}, the returned signal in each polarization, become less alike while the denominator normalizes ρ_{HV} between 0 and 1. Therefore, the correlation coefficient decreases from unity as hydrometeor diversity increases, such as in the melting layer, or when signal strength decreases due to radar constraints and non-meteorological echo (Ryzhkov and Zrnic 1998b).

CHAPTER TWO

Theoretical Electromagnetic Scattering Simulations of Winter Precipitation Types

2.1 Methods: T-matrix and Mueller-matrix

In order to develop a hydrometeor classification algorithm for application to cold season precipitation, T-matrix and Mueller-matrix scattering models were used to calculate the expected dual-polarimetric radar variable ranges for various winter hydrometeor types (Waterman 1965, Barber and Yeh 1975, Vivekanandan et al. 1991). The T-matrix model computes the radar backscattering cross section of particular hydrometeors for a given wavelength based on particle temperature, bulk density, axis ratio, and diameter range. Bulk density is defined as the ratio of the particle's mass to its volume. Illustrated in Fig. 2.1, the axis ratio is assumed to be the ratio between the minor (vertical basal face) and major (horizontal prism face) dimensions of a particle (a/b), where values approach one for spheres. These particles are simply modeled as oblate spheroids instead of their actual branched or irregular shapes. This sufficiently represents various ice crystals and raindrops at X-, C-, and S-band weather radar wavelengths (Bringi and Chandrasekar 2001).

The Mueller-matrix model calculates polarimetric radar (PR) variables for a parameterized distribution of each hydrometeor type. The radar bin is assumed to be filled with a homogeneous population of hydrometeors with a single specified phase: either partially frozen (constant air/ice/liquid mixture), completely frozen, or pure liquid. A population of particles undergoing various stages of melting or containing different hydrometeor types was not simulated in this case. The model uses the radar's wavelength (λ) and elevation angle, the particles' mean canting angle (θ_M) and standard deviation of canting angle (σ), as well as the

particle size distribution (PSD) type, mass-weighted median volume drop diameter (D_0, calculated/input by T-matrix PSD parameters), slope parameter (Λ) for exponential PSD or size parameter (μ) for normalized gamma PSD (Ulbrich 1983, Bringi and Chandrasekar 2001), and number concentration (N_0 for exponential or N_W for normalized gamma PSD). The CANTMAT module is used for normalized gamma distribution simulations. CANTMAT is an interactive program that also calculates electromagnetic scattering properties and radar variables. The most important consideration for choosing D_{MIN} and D_{MAX} in these model is that they are considerably lower or higher than D_0, respectively. This will ensure that the PSD shape and most of the distribution's tail are represented.

2.2 Radar and microphysical parameterizations for T-matrix and Mueller-matrix

The microphysical parameters used in the T-matrix and Mueller-matrix simulations of raindrops, sleet, dry aggregated snowflakes, dendritic ice crystals, and plate-like ice crystals are summarized in Table 2.1. Freezing raindrops were modeled exactly like raindrops except at -1°C. Raindrops can exist at temperatures much lower than 0°C, but in order to discriminate rain vs. freezing rain (occurring at a cooler temperature than rain) below the melting layer, these temperature ranges are sufficient. Sleet is frequently referred to as an ice pellet and the two names are used interchangeably in this study. Wet or melting snow was modeled using a two-layer T-matrix model by Dolan et al. (2012) similar to Depue et al. (2007). The wet snow category is used in a melting layer detection algorithm (Giangrande et al. 2008) to distinguish hydrometeors above and below this level, and is discussed in Chapter 3. Graupel is not currently included in this algorithm because it was not observed during the Oklahoma and Colorado winter storms studied here, but it is known to occur in other winter storms around the world (Takahashi

and Fukuta, 1988; Takahashi et al. 1999; Reinking 1975). A graupel category should be added in the future. Bullet, rosette, and stellar crystal shape extensions are too complex to be resolved by K- through S- band frequency radar systems (Vivekanandan et al. 1994). In addition to needle columnar crystals, these pristine ice particles do not pose a significant winter weather related hazard with which to motivate their inclusion in this hydrometeor classification algorithm. Given these considerations, we have attempted to model the appropriate range of hydrometeors expected from conceptual models of winter storms with consideration for the radar's ability to distinguish such precipitation types.

Higher radar elevation angles can degrade differential measurements such as Z_{DR} and K_{DP} (Ryzhkov et al. 2005b) when the radar beam is no longer oriented along the major (horizontal) particle axis. This will produce lower magnitude Z_{DR} and K_{DP} for oblate ice crystals (Evans and Vivekanandan 1990, Dolan and Rutledge 2009). Elevation angles of 30° (maximum angle for radars used in this study) and 1° were simulated to determine how the radar would realistically perceive such ice particles. Sleet and rain are only expected to exist below the melting level in the stratiform winter precipitation systems we are concerned with in this study. This assumption provides that low radar elevation angles are primarily responsible for interrogating these particles, so they are simply modeled with a horizontal radar viewing angle of 0° (default value for the CANTMAT module utilized to simulate rain, freezing rain, and sleet). Since the parameters used to model raindrops were quite broad, simulations using this single, low-level scanning angle sufficiently described what might otherwise happen at higher elevation angles utilized in reality.

To represent the natural variability of falling precipitation in turbulent background flow, the canting angle of all hydrometeor types is represented as a Gaussian distribution about a mean

canting angle (θ_m) of zero (Beard and Jameson 1983, Hendry et al. 1976, Spek et al. 2008). Canting angles within a few degrees of zero are not thought to contribute to variables such as Z_{DR} and ρ_{HV}, but can significantly affect the linear depolarization ratio, L_{DR} (Ryzhkov et al. 2001). However, L_{DR} is not studied or computed here since the simultaneously transmitting dual-polarized radars deployed by the National Weather Service and in the CASA IP1 network cannot retrieve this quantities. Furthermore, many studies have shown that the discriminatory power of L_{DR} in hydrometeor classification algorithms is redundant to that already provided by Z_{DR}, ρ_{HV}, and K_{DP} (Zrnic et al. 2001).

Pristine snow crystals and snowflakes with large diameters and irregular shapes usually have fluttering or wobbling secondary motions as they fall that resemble helical or spiral motion, axial rotation, or glide-pitch swinging motions (Pruppacher and Klett 1997, henceforth PK97). This is represented by a standard deviation of the canting angle (σ) between 3-30° (Matrosov et al. 1996). Raindrops larger than 1 mm diameter deform into an equilibrium oblate spheroid shape as they fall so their σ values are relatively lower at 1-10° (Ryzhkov et al. 2001). Sleet, similar to small, solid graupel, is rigid and more irregularly shaped than rain and therefore rotates around its major horizontal axis and tumbles erratically during decent, especially if multiple ice pellets are fused together (Spengler and Gokhale 1972). Correspondingly high σ values between 60-80° typically used for hail (Knight and Knight 1970, Kennedy et al. 2001) were adapted for sleet. These irregular fall patterns decrease the effective axis ratio of the particles as scanned by the radar (Bringi et al. 2003b). Canting behaviors of various precipitation types may vary greatly from cloud-to-cloud or within time/space, but in the interest of distinguishing bulk hydrometeor types, we chose σ angles which best characterized how each particle type might fall *differently* than another type.

2.3 Scattering Simulations

Fig. 2.2 shows the K_{DP}, Z_{DR}, and Z_H ranges for X-, C-, and S-band between the 5 major hydrometeor types modeled in this study: dendrites, plates, dry aggregated snowflakes, sleet, and rain based on theory alone. ρ_{HV} is not shown since modeled ρ_{HV} values were all above 0.99, which is not entirely representative of reality. This is the result of only parameterizing homogeneous mixtures of a single precipitation type, while various precipitation types usually coexist and may be undergoing various degrees of melting/freezing within the same radar gate. These simple ρ_{HV} simulations do not lend any inherent discriminatory power towards the hydrometeor classification algorithm except to say that relatively high ρ_{HV} should be expected everywhere except mixed phase regions or where different hydrometeor types coexist. It is noteworthy that the differences between K_{DP} ranges for each precipitation type at X-band are higher magnitude than for other wavelengths. This makes each hydrometeor's polarimetric variable range more exclusive and may lead toward more successful hydrometeor classification, which is discussed at length in Chapters 3 and 4. Simulated differences amongst ice categories and liquid categories are now examined with respect to the input parameters chosen for this microphysical model.

2.3.1 Dendrite and plate crystal theory

The temperature and saturation level with respect to both ice and water determine a crystal's growth habit (Figs. 2.3 and 2.4 from PK97: Fig. 2-36(b) and Fig. 2-37). Since the saturation vapor pressure over ice is lower than that over water, a volume of air may be saturated with respect to ice but unsaturated with respect to water. When the air is only saturated with respect to ice and for temperatures between 0° to -40°C, columnar crystals may form. As the

relative humidity increases toward water saturation (ice supersaturation) and beyond, columns become less common and, particularly between the temperature ranges of -10° to -25°C, plate, sheath, needle, sector plate, and dendrite formation is favored (Fig. 2.5 from PK97: Plate 2). Dendritic growth requires large vapor density gradients toward the crystal, which peak between -13° to -17°C where the difference between the saturation vapor pressure over ice and that over water is greatest.

Because of their skeletal framework and abundance of air in between crystalline branches and sectors, dendrites are modeled as oblate spheres with low bulk density between 0.3-0.5 g cm^{-3} (Fig. 2.6 from Heymsfield (1972): Fig. 5 and Fig. 2.7 from Fukuta and Takahashi (1999): Fig. 12). Their low density and oblate shape determines that dendrites tend to fall very slowly with their maximum dimension oriented horizontally (Fig. 2.8 from PK97: Fig. 10-42). Dendritic branches and stellar arms/sectors determine that these crystals flutter substantially during descent, represented by a 15° standard deviation of canting angle (Matrosov et al. 1996). These factors allow for more residence time in an environment with favorable dendritic growth conditions and for collisions between multiple dendrites to form large, irregular or elongated aggregates as their branches interlock. Thus, individual dendrites can have diameters from 0.03 cm to at least 1.2 cm (Mitchell et al. 1996, PK97, Kennedy and Rutledge 2011). The minimum diameter modeled was 0.01 cm, while the maximum diameter allowed in the T-matrix simulations was only 1 cm.

Similar to the T-matrix inputs for individual dendrites represented in Kennedy and Rutledge (2011), the axis ratios were modeled between 0.135 and 0.2. Any axis ratio of increasing oblateness beyond 0.135 caused unstable model results that would not converge (Matrosov et al. 2012). Finally, the PSD observed by Lo and Passarelli (1982) for pristine

dendrites prior to the onset of aggregation was applied in the model. Many studies have confirmed that an exponential PSD is sufficient to describe populations of dendrites, plates, and dry aggregated snowflakes (PK97).

In reality, ice supersaturation and water saturation increase as updrafts supply vapor rich air upwards due to adiabatic moistening during ascent. The crystal growth regime might gradually transition between thick plates, thin plates, sector plates, and finally to dendrites if the moisture and temperature gradients are gradual, or the transition could be abrupt if there are localized regions of the cloud that become supersaturated quickly or are more favored by a dominant updraft region. However, this study's hydrometeor scattering approach only represents the "extremes" of expected ice crystals between pristine dendrites and solid, hexagonal plates.

Plates are modeled with the bulk density of pure ice, 0.9 g cm^{-3} (PK97). Plates have decreased collection efficiency and growth rates due to their geometry and lower ice supersaturation environments (Foster and Hallett 2008), so their maximum and minimum horizontal dimensions do not reach that of dendrites (Mitchell et al 1996). However, plates and dendrites should have a similar vertical thickness since they are growing exclusively in the horizontal (prism, a-axis) mode. This implies that plates are slightly less oblate than dendrites, which matches observations presented in Fig. 2.9 by Auer and Veal (1970: Fig. 11). They show that the axis ratio between the maximum vertical and horizontal dimensions produce a/b values as low as 0.0009 for 1 cm diameter dendrites, 0.03 for 0.25 cm diameter hexagonal plates, and 0.45 for 0.05 cm diameter thick plates. While our simulation setups qualitatively follow the data from Auer and Veal (1970), our microphysical model is not designed to handle such small a/b values. Therefore, plates are modeled with axis ratios just above the values accepted for dendrites (Kennedy and Rutledge 2011), at 0.2 – 0.5 (Williams et al., 2011).

There is evidence from aircraft observations that N_0 should be higher for populations of plate crystals than for dendrites because decreased aggregation and stinted growth rates allow for more prevalent, smaller sized drops (Bader et al. 1987). Accordingly, the plate PSD has a smaller minimum and maximum diameter (Mitchell 1996), which produces a higher slope parameter (Ryan 2000). This characterizes the exponential plate distribution with a lower D_0, equal to $3.67*\lambda^{-1}$. Observed diameter ranges and D_0 from samples of unrimed plate populations (Fig. 2.10 from PK97: Fig. 2-53) match D_0 values produced in these scattering simulations (Table 2.1).

Under sufficient supersaturations and in the presence of supercooled liquid water drops, crystals of sufficient size may also grow by riming (Fig. 2.11 from PK97: Plate 4, Fujiyoshi and Wakahama 1985). This can change the crystals' fall behavior, increase crystal bulk density, and therefore increase terminal velocity beyond 2 ms^{-1} (Zawadzki et al. 2001; Moismann 1995; Fig. 2.12 from PK97: Fig. 10-44). However, riming has similar effects as aggregation and melting to the snowflake shape, making it appear more spherical to the radar by thickening the crystal and increasing its axis ratio toward unity. These competing effects contribute toward uncertainty in discerning crystal characteristics and therefore crystal growth environment (temperature and moisture levels) using dual-polarized radar. Results from the scattering simulations of plates and dendrites, and thus our ability to use radar to distinguish then, are now discussed.

2.3.2 Dendrite and plate crystal scattering model results

The simulated ranges of K_{DP}, Z_{DR}, and Z_H for dendrites at X-, C-, and S-band frequencies are presented in Fig. 2.13 with S-band comparison ranges for dendrites from Kennedy and Rutledge (2011), Trapp et al. (2001), Ryzhkov et al. (2005a), and Straka et al. (2000). The S-band simulated values from this study agree very well with those from previous works, as the

ranges overlap within reason. It should be noted that values from Straka et al. (2000) are based on many sources for both dendrites *and* plates. As will be discussed later, the high K_{DP} from this study is indicative of dendrites but the higher Z_{DR} return may be more representative of plates, which extends beyond the modeled Z_{DR} values for dendrites.

There is a slight increase in Z_H and slight decrease in Z_{DR} with increasing wavelength, which has been explained by Matrosov et al. (2005) as non-Rayleigh scattering effects of oblate spheroids. This argument also justifies why the K_{DP} simulated at X-band is actually 3.7 times greater than at S-band even though the wavelength is only shorter by a factor 3.4. Scattering simulations of warm-season precipitation particles at X- and S- band by Dolan and Rutledge (2009) also produced similar results. These two non-Rayleigh scattering phenomena are evident in all our simulations of ice and liquid hydrometeors.

These model results suggest that the ~0.6° km^{-1} maximum K_{DP} values for dendrites observed at S-band by Kennedy and Rutledge (2011) are nearly the maximum values possible for this wavelength. S-band K_{DP} beyond 0.6-0.7° km^{-1} would likely be due to increased $D > 1$ cm, which the T-matrix and Mueller-matrix models cannot simulate but are known to occur in nature. Operational S-band dual-polarized radars must be designed to detect such small phase shifts and calculate K_{DP} with high precision in order to confidently interpret K_{DP} values as indicative of pristine, oblate ice crystals. K_{DP} observations through dendritic growth zones at X-, C-, and S-band from three different winter storms are compared to these scattering simulations in Ch. 4.

It is common knowledge that while K_{DP} is dominated by particle axis ratio according to equations (5) and (7) in Chapter 1, there are additional competing factors at play. Fig. 2.14 shows the sensitivity of K_{DP}, Z_{DR}, and Z_H for dendrites to variable input parameters from Table 2.1. K_{DP} increases as bulk density, D_0, and N_0 increase or as axis ratio decreases. K_{DP} is often described as

being independent of number concentration, but every particle in the PSD simulation was oblate. Accordingly, any increase in the number of *oblate* particles results in a positive contribution to K_{DP}. These scatter plots also show that a change in axis ratio between 0.2-0.135 does not produce much increase in K_{DP}, which remains high for all modeled a/b values. For these very oblate simulations, K_{DP} actually appears more sensitive to changes in bulk density, D_0, and N_0.

Also taken as a crude measure of oblateness, Z_{DR} for dendrites increases for increasing bulk density and decreasing axis ratio. There is no dependence on N_0 or D_0 because this quantity is the ratio of reflectivity between the horizontal and vertical channels as expressed in (2), so PSD information effectively cancels between the numerator and denominator. The same cannot be said for Z_H, which is the most sensitive variable to D_0, and secondarily to bulk density according to these plots. The variable density of pristine and aggregated ice crystals is known to complicate the differential radar returns without appreciable differences in Z_H (Trapp et al. 2001). Reflectivity and therefore differential reflectivity have a D^6 dependence according to (1) and (2), but Z_{DR} is less dependent on diameter because this relationship is logarithmic. Specific differential phase has a D^3 dependence through factors of liquid/ice water content (expressed in units of mass per unit volume) and deviation of the mass-weighted mean axis ratio from unity in equations (5), (6), and (7).

With slightly different microphysical parameterizations, simulated K_{DP}, Z_{DR}, and Z_H for plates shown in Fig. 2.15 differ from that of dendrites. For instance, the maximum simulated Z_{DR} is about 1.25 dB greater for plates than dendrites at all wavelengths, while the minimum values are only 0.5 dB greater. So the expected range of Z_{DR} values is shifted upwards and slightly broadened between the two crystal types. K_{DP} is doubled for dendrites compared to plates at all wavelengths while the minimum values for both categories are slightly greater than zero. Wolde

and Vali (2001) and Williams et al. (2011) provide observations of Z_{DR} and Z_H for plates at X- and C-band, respectively, also provided in Fig. 2.14, which generally contain the simulated values from our microphysical model. Straka et al. (2000) gives S-band values of K_{DP}, Z_{DR}, and Z_H for a population containing plates *and dendrites*. As previously discussed, their high K_{DP} is more representative of dendrites but their high Z_{DR} corresponds well with plate simulations. Fig. 2.16 illustrates the relationships between polarimetric radar (PR) variables and microphysical parameterizations for plates, which correspond to the same relationships observed for dendrites.

Even though Z_H varies very little between ice categories according to Fig. 2.2, dendrites have higher Z_H than plates because D_{MAX} and D_0 are greater. This size factor evidently outweighs the role of density, which would otherwise tend to increase Z_H for plates. Plates have higher density and are less oblate but have lower K_{DP} and higher Z_{DR} than dendrites. Figs. 2.14 and 2.16 help explain the meaning behind this inverse Z_{DR}-K_{DP} relationship.

There is an integration of the PSD involved in the *IWC or W* and $\bar{r}$ terms of the K_{DP} equations so increasing D_0 and N_0 contribute to greater K_{DP} by *both* terms. The shape effect is important for determining K_{DP} between plates and dendrites, but this factor is also weighted by mass so D_0 and the shape of the *PSD* are also important considerations. Furthermore, the K_{DP} return from the most oblate plates hardly even approaches the K_{DP} from the lease oblate dendrites, both at a/b = 0.2. This reveals that while lower axis ratio contributes to higher K_{DP} for dendrites as opposed to plates, it is not the only critical factor.

K_{DP} increases significantly for increasing N_0, but N_0 values modeled for plates were much higher than for dendrites (as previously explained). However, the highest N_0 for plates barely produced a K_{DP} as large as the lowest N_0 for dendrites. So N_0 is not the deciding factor between the inverse Z_{DR}-K_{DP} relationship either.

Bulk density is higher for plates, which should increase W and therefore K_{DP} since these variables are directly proportional. From this mathematical standpoint, one might expect that a doubling of the density might at least double the K_{DP} for plates compared to dendrites for nearly the same axis ratios. For instance, 0.5 g cm^{-3} maximum ρ_{bulk} for dendrites produces nearly 2.5 times the K_{DP} return as the 0.3 g cm^{-3} minimum ρ_{bulk} for dendrites, and plate bulk density is still much greater than this, at 0.9 g cm^{-3} (not simulated for dendrites because this would never occur in nature). Surprisingly, K_{DP} is still higher for low-density dendrites than high-density plates.

Examining the remaining microphysical differences between these two particle types, D_0 is 50% smaller for plates than dendrites, and perhaps not coincidentally, K_{DP} is 50% smaller. The median volume drop diameter, D_0, bisects the volume of particles within the distribution. It seems that the PSD shape, where the mass is situated among sizes, matters most in this case; more than N_0, bulk density, and even axis ratio. The increased D_0 produces *larger* oblate dendrites that actually overcome the expected enhancement of K_{DP} by higher-density, more numerous plate crystals. This is most likely because D_0 and therefore D_M (the mean mass-weighted volume diameter, which is proportional to and usually larger than the median mass-weighted volume diameter D_0 according to Ulbrich 1983) are factors in both the W and mass-weighted axis ratio terms within the liquid K_{DP} equation (5), or density and IWC terms of the frozen K_{DP} equation (7).

It is significant that these simple parameterizations produced radar results that are consistent with cloud microphysical theory. The physical explanation lies in the vapor depositional growth rate equations. The mass and diameter rate of change with time are both proportional to the diameter of the crystal such that a larger crystal can incorporate more vapor into its ice lattice structure. Furthermore, dendrites grow at higher saturation conditions, which

promote higher growth rates and resultant maximum diameters. While thick plates, hexagonal plates, and dendrites may all originate as small ice germs, they accordingly grow at different rates and achieve different maximum diameters. Dendritic arms also provide additional structures onto which vapor can collect, so that, again, dendrites can achieve larger diameters than plates. It follows that plates also have more numerous smaller particles in the distribution because these did not grow to longer dimensions. Although our microphysical model does not include any of these growth processes, the parameters used capture these important particle distribution characteristics and how the radar should perceive each snow crystal differently.

Yet to be explained, plates have higher Z_{DR} than dendrites despite their slightly increased axis ratio toward sphericity. Straka et al. (2000) suggests that plates should have the highest Z_{DR} because of their geometry. Z_{DR} is the reflectivity weighted mean axis ratio of the particle size distribution (Jameson 1983), so all other factors remaining equal, Z_{DR} should increase for increasing oblateness. However, dendrites still have lower characteristic Z_{DR} even though they are more anisotropic than plates. This is consistent with Bringi and Chandrasekar (2001), who argue that Z_{DR}'s logarithmic dependence on axis ratio in (2) weakens its sensitivity to shape compared to K_{DP}. The decrease in Z_{DR} that should occur due to higher a/b for plates is evidently outweighed by an increase in ρ_{bulk}. It is intriguing that of the competing factors, density seems most important for determining higher Z_{DR} for plates than dendrites since this variable is so often taken as a proxy for hydrometeor shape.

Dolan and Rutledge (2009) found that Z_{DR} and K_{DP} could decrease by as much as 0.5 dB and 0.1° km^{-1}, respectively, when the radar viewing angle is increased from 1° to 30° for a monodisperse population of small, spherical, monodisperse rain drops at X- and S-band. Evans and Vivkeanandan (1990) found a more significant elevation angle effect on K_{DP} and Z_{DR} for

plates at Ka-band. K_{DP} decreased by 8° km^{-1} while Z_{DR} was diluted by 4 dB for this same difference in elevation angle because the major (horizontal) axis of the oblate crystal was no longer oriented along the beam in order to maximize the differential power return and phase shift. When examining a vertical cross section (Range Height Indicator – RHI) or quasi-horizontally oriented sweeps from a full volume scan (Plan Position Indicator – PPI), this effect would manifest itself as a gradual non-meteorological lowering of Z_{DR} and K_{DP} with height from one elevation angle to the next, not with increasing range (height) along a single sweep. However, the latter could be occurring simultaneously due to non-uniform beam filling effects as the beam broadens with range, especially for shorter radar wavelengths (Ryhzkov et al. 2007).

The maximum possible elevation angle for the radar systems used in this study is 30° and 20° was the highest actually utilized. Fig. 2.17, 2.18, and 2.19 show how Z_{DR} and K_{DP} would behave at 30° compared to 1° (both angles were used in all previous figures). Maximum K_{DP} for oblate crystals (Fig. 2.17) decreases more for shorter wavelengths: 0.48, 0.286, and 0.143° km^{-1} difference for dendrites and 0.227, 0.131, and 0.065° km^{-1} difference for plates at X-, C-, and S-band wavelengths, respectively. The minimum K_{DP} values only decrease by 0.1° km^{-1} or less, which does not have an impact on the hydrometeor classification procedures. Since all K_{DP} values decrease, the ranges between plates, dendrites, and dry aggregated snowflakes (incredibly low anyway) are still exclusive enough to classification purposes. The discriminatory power of K_{DP} needed to distinguish the two oblate crystal habits is still lessened though, and more so at shorter wavelengths for which K_{DP} is expected to be more informative.

Fig. 2.18 shows that more significant Z_{DR} changes occur for increasing elevation angle that might preclude successful discrimination between plates and dendrites. At 1° elevation angle, plates had 1.31 dB higher Z_{DR} than dendrites and dendrites had 0.4 lower Z_{DR} than plates.

These different ranges of expected values are more exclusive and more useful for hydrometeor classification than those at 30°, whereby Z_{DR} for plates is only 0.8 dB greater than dendrites and the dendrites only have 0.3 dB lower Z_{DR} than plates. In this way, the expected Z_{DR} value ranges for plates and dendrites narrow and overlap more at higher elevation angles. The Z_{DR} and K_{DP} expected value ranges for all hydrometeor types at 30° viewing angle only are presented in Fig. 2.19, which can be compared to Fig. 2.2. When both elevation angles are simulated, the expected value ranges for each oblate ice crystal are more mutually exclusive.

To summarize, plates might be present in a particular radar bin, but Z_{DR} might not increase beyond the dendrite range because the elevation angle dependence is dominating over the microphysics to determine the differential radar variables. Similarly, K_{DP} might decrease because plates are more prevalent than dendrites and/or because the elevation angle has increased. Both dendrites and plates have reduced K_{DP} and Z_{DR} at higher slant viewing angles, but in the case of dendrites, this effect could simply be indicative of smaller diameter, lower density, and/or less oblate dendrites. These issues will still allow for successful classification of dendrites, whereas the elevation angle problem reduces the possibility of plate classification apart from dendrites. These issues are further complicated by decreasing radar power and thus decreasing signal to noise ratio (*SNR*) with range, such that Z_{DR} may increase due to non-meteorological reasons near the echo top or echo fringe where $SNR < 5$ dB (Ryzhkov et al. 2005a). This is also unfortunately where oblate crystals usually grow. Perhaps a more advanced version of the hydrometeor classification algorithm discussed in Ch. 3 could incorporate elevation angle into the decision process to account for these issues.

The PR differences between plates and dendrites are important because distinguishing these two ice categories is of great interest from a nowcasting perspective. Unlike plates,

dendrites can coagulate and then delay or prolong the melting process below. Accordingly, dendritic growth aloft could be associated with semi-melted or slushy particles below the melting layer which can promote the production of sleet over freezing rain in the presence of a sufficiently cold/deep layer of air (Thériault et al. 2006). More intense precipitation rates can also occur at the surface when aggregated snowflake diameters are larger or particles are more numerous (Kennedy and Rutledge 2011). The water-saturated conditions for dendritic growth may also be supportive of supercooled liquid water drops that are hazardous to aircraft, as opposed to benign conditions associated with only ice saturated conditions for plates.

While it is of potentially great value to differentiate these two ice crystal types for the aforementioned reasons, it may not be a feasible goal for most radar systems. This is because 1) longer wavelength systems have a less distinguishing Z_{DR}-K_{DP} relationship and lower magnitude K_{DP} signals all together, 2) Z_{DR} must be well-calibrated and the K_{DP} calculation must be very precise for the radar to resolve small changes in these variables associated with different crystal habits, 3) *SNR* must be greater than 5-10 dB for Z_{DR} to be trustworthy, and 4) the elevation angle must be relatively low so that Z_{DR} and K_{DP} are not "diluted" by non-parallel beam-to-crystal orientation. The most difficult of these constraints to overcome are the last two, since plates and dendrites are inherently native in the upper (colder) regions of winter storms, which require high slant-range viewing angles to resolve. Spek et al. (2008) postulated that when dendrites and plates have similar radar cross sections (for small diameters) the other microphysical properties (axis ratio and density) are similar enough that there is no possibility to differentiate them. From this analysis we conclude that even the largest dendrites and plates may not be distinguishable.

2.3.3 Dry aggregated snowflake theory

Snowflake aggregation is most prolific when temperatures approach 0°C and -15°C because 1) quasi-liquid layers form and promote sticking of individual crystals as well as the fusing of colliding particles between ice necks, and 2) dendritic ice crystals have high collection efficiencies from their slow fall speeds and long interlocking branches, respectively. For the latter reason, planar crystals with dendritic features are the most common components of aggregates (Fig. 2.20 from PK97: Plate 3, Jiusto and Weikmann 1973). PK97 affirm that bundles of needles are also observed, but aggregated snowflakes of simple, thick ice plates and short columnar crystals are rare, most likely due to unfavorable geometry. Since individual dendrites can reach at least 1.2 cm D_{MAX}, aggregates of these crystals can easily exceed 2 cm. However, the highest D_{MAX} in T-matrix is 1.0 cm. These snowflakes were modeled at -1° and -6°C to account for the sticking formation mechanism. We did not lower the temperature further because this would produce a negligible change in the dielectric constant and therefore the radar variables.

A power law relationship was required to describe the bulk density of snowflakes as a function of size. Clumps of dendrites with very large combined diameters have extremely low bulk density because there are many air pockets in between branches and the mass is distributed across a larger volume. However, some smaller, compacted aggregates will have higher bulk density. Fig. 2.21 illustrates this well-established diameter-density relationship with multiple empirically derived formulas from observations (Magono and Nakamura 1965, Holroyd 1971, Locatelli and Hobbs 1974, Fabry and Szyrmer 1999, Hogan et al. 2000, Brandes et al. 2007). The majority of naturally occurring, larger aggregates should have $\rho_{bulk} \sim 0.05$ g cm^{-3}, while bulk density could range anywhere from 0.01 to 0.2 g cm^{-3}. Only the smallest snowflakes will approach $\rho_{bulk} > 0.15$ g cm^{-3} (PK97). The Hogan et al. (2000) relationship was used in this

microphysical model because of its derivation from aggregated snowflake observations. However, a sensitivity study confirmed that any of these exponential formulas (except Magono and Nakamura 1965) produce nearly the same electromagnetic scattering result. It should be noted that Zhang et al. (2011) used dual-polarimetric radar and 2-dimensional video disdrometer (2DVD) observations of snowflakes in Oklahoma to determine that these accepted formulas (Brandes et al. 2007 in particular) may underestimate the bulk density of snowfall in particular geographic regions or during certain storms. We remain confident in our choice of scattering parameterizations though because simulated D_0 values (Table 2.1) agree well with many snowflake size distribution observations (Locatelli and Hobbs 1974, Lo and Passarelli 1982, Herzegh and Jameson 1992, Vivekanandan et al. 1994, Barthazy et al. 1998, Spek et al. 2008).

Aggregates tend to cant over larger angles or tumble more dramatically than pristine crystals because of their longer diameter and more irregular shape (Kajikawa 1982). The σ value for aggregates was accordingly doubled from that of dendrites and plates to 30° (Matrosov et al. 1996, Kennedy and Rutledge 2011). Instead of modeling aggregates with even lower, very oblate axis ratios and extremely high standard deviation of canting angle (perhaps more true to nature), the axis ratios are raised to effectively represent a nearly spherical particle with moderate σ (manual approximation of nature). Effective axis ratios then range between 0.7 – 0.9 after many literature examples (Barthazy 1998, Vivekanandan et al. 1994, Herzegh and Jameson 1992, Dolan and Rutledge 2009, Kennedy and Rutledge 2011).

The PSD of aggregated snowflakes is “flattened” compared to that of their pristine component crystals. This is accomplished by decreasing N_0, decreasing the slope parameter, increasing D_0, and increasing D_{MIN} (Lo and Passarelli, Spek et al. 2008). This process can be explained physically by the aggregation (consumption) of many smaller sized crystals into larger

ones. Mass is accordingly shifted from smaller to larger size intervals (Spek et al. 2008, Lo and Passarelli 1982).

2.3.4 Dry aggregated snowflake scattering model results

Fig. 2.22 presents the polarimetric radar variable ranges for dry aggregates. These values correspond well to those given in Ryzhkov et al. (2005a), Dolan and Rutledge (2009), and Straka et al. (2000) for aggregates at both X- and S-band radar frequencies. Recall that Z_H is insensitive to axis ratio but depends strongly on D^6 (Vivekanandan et al. 1994). Since snowflakes have the largest D_0 of all frozen hydrometeors simulated in this study, it is no surprise that Fig. 2.2 illustrates these hydrometeors with the highest modeled Z_H (Ohtake and Hemni 1970, Ryzkhov and Zrnic 1998a, Boucher and Wieler 1985). Ironically, snowflakes also produce the lowest K_{DP} and Z_{DR}.

The Z_{DR} range for aggregates is extremely low and mutually exclusive from other hydrometeor types according to Fig. 2.2, which will aid in the classification algorithm. Ryzhkov et al. (2005a) suggest that Z_{DR} tends to decrease as Z_H increases, or as aggregation progresses and diameters of coagulated snowflakes increase. Trapp et al. (2001) confirms that, compared to pristine crystals, Z_{DR} should be substantially lower for aggregates because of their decreased density and erratic fall behavior.

Simulated K_{DP} for snowflakes is near zero but still contained within the ranges for other ice crystals, providing less discriminatory power for hydrometeor classification than Z_{DR}. The radar variables associated with aggregates are expressed as a function of microphysical parameters in Fig. 2.23. These scatter plots illustrate that K_{DP} increases for decreasing axis ratio, increasing N_0, and increasing D_0, consistent with previous arguments for component ice crystals.

Z_{DR} also has a slight dependence on D_0, which is not exhibited by plates or dendrites. The greatest variation in Z_H for aggregates is actually produced by variable N_0 as opposed to D_0. The sensitivity of radar variables to bulk density of snowflakes was not analyzed because these values are intrinsic to the program through use of the empirical formula. However, a hypothetical scattering simulation showed that a majority of the high Z_{DR} and K_{DP} contributions are made by the highest density aggregates.

2.3.5 Rain, freezing rain, and sleet theory

Raindrops falling at terminal velocity with diameters greater than 1 mm deform into oblate spheroids due to aerodynamic drag forces (PK97, Beard and Chuang 1987). The CANTMAT module allowed use of empirically derived drop shape models to express the axis ratios of sleet and raindrops in terms of their diameter (Pruppacher and Pitter 1971; Figs. 2.24 and 2.25 from Beard and Chuang 1987: Fig. 7 and 10; Andasager et al. 1999; Thurai and Bringi 2005; Huang et al. 2008). A normalized gamma drop size distribution was utilized to more accurately represent the natural variability of stratiform rain and sleet below the melting level (Ulbrich 1983; Willis 1984; Bringi et al. 2003a; Fig. 2.26 from Gibson et al. 2009: Fig. 10).

Stratiform rain has a characteristically different DSD than convective rain, a phenomenon first investigated for its enhanced radar bright band (Waldvogel 1974). The convective rain DSD owes its existence to quickly falling graupel and hail particles formed by strong updrafts that fall and melt in warm subcloud temperatures. This rain regime does not necessarily produce a significant radar bright band. Conversely, stratiform rain is associated with gentler upward vertical velocities and the generation of pristine ice crystals which aggregate as they fall toward the melting level. The gradual, and therefore radar observable, melting (wetting) of these large

aggregates where T > 0°C produces a population characterized by more numerous larger raindrops, fewer smaller sized drops, lower N_W, lower size parameter (μ), and larger D_0. The combined effects of aggregation and melting modulate the exponential PSD of snow crystals and snowflakes to a normalized gamma distribution for rain with μ between 0.5 - 2.0 (Fig. 2.27 from Ulbrich 1983: Fig. 2).

Raindrops and wet snowflakes freeze into ice pellets either individually at subzero temperatures (IP-a type), or by colliding with snowflakes, ice pellets or other suitable freezing nuclei (IP-b type, Thériault et al. 2006; Fig. 2.28 from Thériault et al. 2010: Fig. 1). Every raindrop is expected to have the potential to turn into an ice pellet in favorable freezing conditions (Gibson et al. 2009), but the IP-b formation process is not a one-to-one conversion, which might increase D_0 and decrease N_w. Nevertheless, the stratiform rainfall DSD was used for sleet because the parameters in Table 2.1 are broad enough to account for both refreezing mechanisms.

The resultant sleet shape can be quasi-spherical and similar to that of raindrops, but more often than not these hydrometeors have bulges, spicules, spikes, or are fused together by ice-necks (Gibson and Stewart 2007). A frozen drop's thin ice shell can rupture or crack shortly after freezing begins, allowing supercooled water from the interior to fuse the two freezing/frozen particles together and/or become frozen into an irregular protuberance (Spengler and Gokhale 1972). This nonspherical, rigid shape induces erratic tumbling, which is represented in the scattering simulations by an increased standard deviation of the canting angle as previously described. As will be illustrated later, the decreased dielectric factor and increased canting of these irregular particles dominates their polarimetric radar variable ranges, so the sleet diameter range was not extended to reflect the coagulation of multiple frozen drops or snow pellet fusions.

Furthermore, previous studies have not conclusively documented sleet's increased maximum size beyond that of rain or an alternative PSD outside the natural variability of rainfall (Gibson et al. 2009, Stewart et al. 1990b). Ice pellets were therefore modeled as completely frozen oblate spheroids with the same diameter-shape relationships and diameter ranges as rain.

Sleet has been observed to form at a variety of subfreezing temperatures (Gibson et al. 2009), while -4°C is recognized as the temperature that distinguishes clear from opaque ice pellets (Spengler and Gokhale 1972). When drops freeze very quickly or at T < -4°C, they are often opaque because more air bubbles remain trapped within the ice structure.

2.3.6 Rain, freezing rain, and sleet scattering model results

The modeled polarimetric variables for rain at various wavelengths are compared to literature examples of stratiform rain (Straka et al. 2000 at S-band for DSDs characterized by various D_{MAX} values), convective rain, and drizzle (Dolan and Rutledge 2009 at X- and S-band) in Fig. 2.29. Since convective rainfall according to Dolan and Rutledge (2009) is characterized by higher N_0 (up to 100,000 cm^{-1} m^{-3}) and D_0 (up to 0.35 cm), our stratiform rainfall scattering results have slightly lower Z_{DR} and Z_H values. Raindrops produced by melted snow typically have diameters less than 3 mm (Stewart et al. 1984). With this interpretation in mind, the model results agree well with these related studies. K_{DP} values derived for raindrops are also reasonable compared to observations (Bringi and Chandrasekar 2001, Straka et al. 2000) and are discussed later with Fig. 2.35.

K_{DP}, Z_{DR}, and Z_H for ice pellets at X-, C-, and S-band radar wavelengths are compared with literature results for high-density graupel in Fig. 2.30 since sleet was modeled as pure ice. No polarimetric radar observations of sleet are available with which to directly test the

microphysical parameterizations or scattering results. As expected, sleet polarimetric radar (PR) variables simulated in this study are much lower than that derived or observed for high-density, rimed graupel, whose D_0 range is much higher: between 0.3-0.75 cm (Dolan and Rutledge 2009 at X-and S-band, Straka et al. 2000 at S-band). Graupel was not modeled or including in the hydrometeor classification algorithm, but these literature examples suggest that the distinguishing factor between graupel and other winter hydrometeor types discussed so far would be very high Z_H, beyond what is expected for rain, dry aggregates, or wet snow, combined with high ρ_{HV}. Z_{DR} and K_{DP} for graupel would be contained within the ranges for oblate crystals and rain, so these variables likely would not be as helpful in the fuzzy-logic process.

Fig. 2.31 shows the relationships of PR variables at X-band derived for rain (and sleet in a qualitative sense) to the microphysical parameters from Table 2.1. Z_{DR} and K_{DP} do not vary much between the σ values used. More σ-related PR variability is noted for sleet than rain because sleet σ ranges were wider. K_{DP} seems most sensitive to changes in D_0 and N_0, while Z_{DR} and Z_H depend mostly on D_0. Figs. 2.32 and 2.33 illustrate the nonlinear behavior between these three PR variables and the standard deviation of the canting angle for rain at C-band, but not at other wavelengths or for sleet. These results are reminiscent of non-Rayleigh scattering by oblate raindrops at C-band frequency (Keenan et al. 2001, Zrnic et al. 2000), which may not occur for the ice medium. There is also a nonlinear relationship between D_0 and the three PR variables for both rain and sleet at all wavelengths, illustrated in both Fig. 2.31 and Fig. 2.34. K_{DP} is the only PR variable shown in the latter figure, but this effect is also consistent for Z_H and Z_{DR} across all wavelengths and for both hydrometeor types. This could be due to the parameterized shape of the normalized gamma particle distribution.

A sensitivity study was performed to test the radar's potential ability to differentiate rain, freezing rain, and sleet with two different fall behaviors. The sleet category was modeled as pure ice with raindrop shapes and PSDs at -4°C for X-, C-, and S-band wavelengths and either the low standard deviation of canting angles used for rain or for tumbling graupel. Freezing rain was modeled exactly as rain except at -1°C and only for C-band radar frequency since these preliminary results were sufficient for this exercise. Fig. 2.35 shows the K_{DP}, Z_{DR}, and Z_H scattering results for these hydrometeor test types.

The relative dielectric constant changes caused by 1) decreased dielectric factor, density, and temperature from rain (RN) to sleet (SL_1, with the same fall behavior as rain), and 2) only a decrease in temperature from rain to freezing rain (-RN) can be isolated from this subset of data. There was a negligible difference between PR variables for rain and freezing rain at C-band and a much larger difference between rain (RN) and sleet (SL_1). This shows that the density and composition difference between ice and water is more significant for determining the PR variables than the change in temperature alone. Water has higher polarizability from its permanent dipole moment and the enhanced readiness with which water molecules will align to an external (incident) electric field. Accordingly, the dielectric factor of ice is 20% of that for water and this reduces the radar backscattering cross section, which reduces each PR variable for sleet (SL_1) compared to rain.

However, Fig. 2.35 shows that the difference in PR variables between RN and SL_1 categories is not as significant as the decreases shown from RN to SL_2. The fall behavior of tumbling ice pellets (SL_2) accounted for an additional 53% decrease in maximum Z_{DR} and K_{DP} and only a 0.3% additional decrease in maximum Z_H than SL_1 at all three radar frequencies. Canting should only affect the differential measurements through their sensitivity to differential

phase shifts and backscattered power between the H and V channels. This quantitatively shows that fall behavior is an important factor, in addition to the dielectric factor and density, for determining the different polarimetric radar properties of sleet and rain.

This analysis also confirms that the differences between freezing rain, sleet, and rain are not large enough to distinguish these hydrometeors without the use of temperature. The radar values produced by freezing rain or sleet could simply be attributed to light rain. For instance, observations of rain by dual-polarimetric radars routinely exhibit a slight decrease in Z_H and K_{DP} with a negligible change in Z_{DR} toward the ground due to evaporation in subsaturated air (Kumjian and Ryzhkov 2010). Evaporation causes shrinking of all diameters, preferential evaporation of the smallest drops, and a decrease in number concentration. Furthermore, freezing rain is simply supercooled rain that glaciates upon contact with the earth's surface, which is often below even the lowest radar elevation angle scans. So it is still "rain" in the regions where it can be interrogated by the radar and therefore a radar-only hydrometeor classification algorithm cannot logically include freezing rain as a category. Nevertheless, incorporation of near-surface and surface temperature could lead to the reclassification of rain as freezing rain at these levels.

While the ambiguities implied by these scattering simulations negate the possibility for a radar to distinguish these precipitation types without external information, the actual freezing process might be identifiable. Sleet and rain were modeled separately here, as opposed to a more realistic mixture of frozen, partially frozen, and unfrozen drops (Fujiyoshi and Wakahama 1985). The rate of refreezing is controlled by the amount of water in the drops, so the drop size distribution of rain affects the refreezing process and vice-versa (Thériault et al. 2006). By this logic, the smallest precipitation sized drops and those that contain some portion of ice should freeze more quickly into sleet while the largest, liquid particles may remain unfrozen for much

longer fall distances through the surface cold layer. In this way, semi-melted particles below the melting layer promote the production of sleet instead of freezing rain.

This mixed phase particle population would be diverse with respect to densities (between that of pure ice and water ~ 0.9 to 1.0 g cm^{-3}), orientations (significantly different fall behaviors between liquid and frozen drops), compositions, and possibly even fall speeds. Raindrops are thought to fall faster than sleet when particle size is small since rain is denser, but sleet has the ability to coagulate and reach larger maximum diameters beyond the equilibrium size of raindrops dictated by hydrodynamic forces. Therefore, we expect large, heavier sleet particles to have a greater terminal velocity than raindrops beyond a certain diameter range (Spengler and Gokhale 1972). The number concentration and D_0 will also increase if type-b ice pellets form by colliding with supercooled drops. All or some of these factors could be manifested by characteristic trends in Z_{DR}, Z_H, ρ_{HV}, and/or K_{DP} within the refreezing zone just above the surface during a winter storm. The T-matrix and Mueller-matrix models were not used to model mixtures of different hydrometeors, so we must rely on observations to confirm this theory, which are presented in Chapter 4. More complex electromagnetic scattering simulations could be performed, but were beyond the scope of this thesis.

2.4 Summary

Radar constraints combined with nearly overlapping variable ranges complicate the ability of a polarized radar to confidently differentiate plates and dendrites. However, both oblate crystal types are certainly distinguishable from dry aggregated snowflakes through use of Z_{DR}, especially at shorter wavelengths where K_{DP} ranges for each pristine crystal are larger and therefore more exclusive. While homogeneous populations of rain, freezing rain, and sleet

appear nearly the same to a dual-polarized radar, the freezing process could be identifiable because of characteristic changes in the drop size distribution, composition, and fall behavior toward the ground.

These results show that the ultimate Z_H, Z_{DR}, and K_{DP} within a particular radar bin depends on many competing microphysical and radar scanning factors, some of which become more important than others at specific value ranges or environments. For instance, density, axis ratio, diameter, and number concentration compete to determine an inverse Z_{DR}-K_{DP} relationship between dendrites and plates. That plates have higher Z_{DR} while dendrites have higher K_{DP} was counterintuitive at first but is reasonable considering how these radar variables are calculated from first principles. Raindrops have significantly higher PR variables than sleet because of their higher dielectric constant (primarily due to density and liquid composition, and secondarily by lower temperature) and smoother fall behavior. Finally, the effects of mass-weighted D^3 and reflectivity-weighted D^6 factors also complicate the calculation of these polarimetric radar variables since they appear in some equations more than once and are not always apparently included in simplified forms of the equations.

This chapter has demonstrated the complexity and uncertainty involved in analyzing multiple polarimetric radar variables simultaneously during a winter storm to deduce dominant hydrometeor type. A hydrometeor classification algorithm is a useful way to automatically apply fuzzy-logic to this decision process (Liu and Chandrasekar 2000, Zrnic et al. 2001, Chandrasekar et al. 2011). Since we have verified these theory-based electromagnetic scattering results, we can now use them to develop such an algorithm. This will be the subject of the next chapter.

Table 2.1. Microphysical parameters for T-matrix and Mueller-matrix used to calculate dual-polarimetric radar variables for various hydrometeor types.

Hydrometeor Type	**Axis Ratio**	**Temp**	**ρ_{bulk}**	**D_{min}**	**D_{max}**	**ΔD**	**Mean Canting Angle (θ_m)**	**SD of Canting Angle (σ)**	**PSD Type**	**N_o or N_W**	**D_o**	**Slope (Λ) or Size Parameter (μ)**	**Radar Elev. Angle**
	a/b	*°C*	*g cm^{-3}*	*cm*	*cm*	*cm*	°	°		*cm^{-1} m^{-3}*	*cm*	*cm^{-1}*	°
Rain	1,3,4, 5,8 *	10	1.0	0.01	0.5	-	0	1 4 10	normalized gamma	2,000 8,000 20,000 60,000	0.05 0.1 0.15 0.2	0.5 1.0 1.5 2.0	0
Sleet	1,3,4, 5,8 *	-4	0.9169	0.01	0.5	-	0	60 70 80	normalized gamma	2,000 8,000 20,000 60,000	0.05 0.1 0.15 0.2	0.5 1.0 1.5 2.0	0
Dry Aggregated Snowflakes	0.7 0.8 0.9	-6, -1	Hogan et al. (2000)	0.08	1.0	0.001	0	30	exponential	20,000 40,000 60,000	0.334 0.306 0.282	11 12 13	1 30
Dendrites	0.135 0.15 0.2	-15	0.3 0.4 0.5	0.02	1.0	0.001	0	15	exponential	100,000 200,000 300,000	0.122 0.105 0.092	30 35 40	1 30
Plates	0.2 0.3 0.5	-13	0.9	0.0015	0.5	0.0005	0	15	exponential	100,000 300,000 600,000 900,000	0.061 0.052 0.046	60 70 80	1 30

*** selected drop shape models for Cantmat simulations:**

1 – Pruppacher and Pitter (1971)
3 – Beard and Chuang (1987)
4 – Andsager et al. (1999)
5 – Thurai and Bringi (2005) “ogimi”
8 – Huang et al. (2008) “bridge”

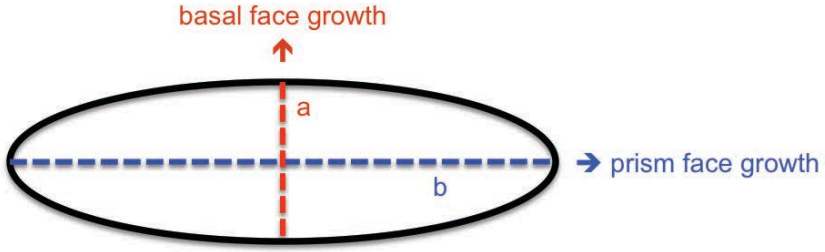

Fig. 2.1. Ice crystal dimension diagram.

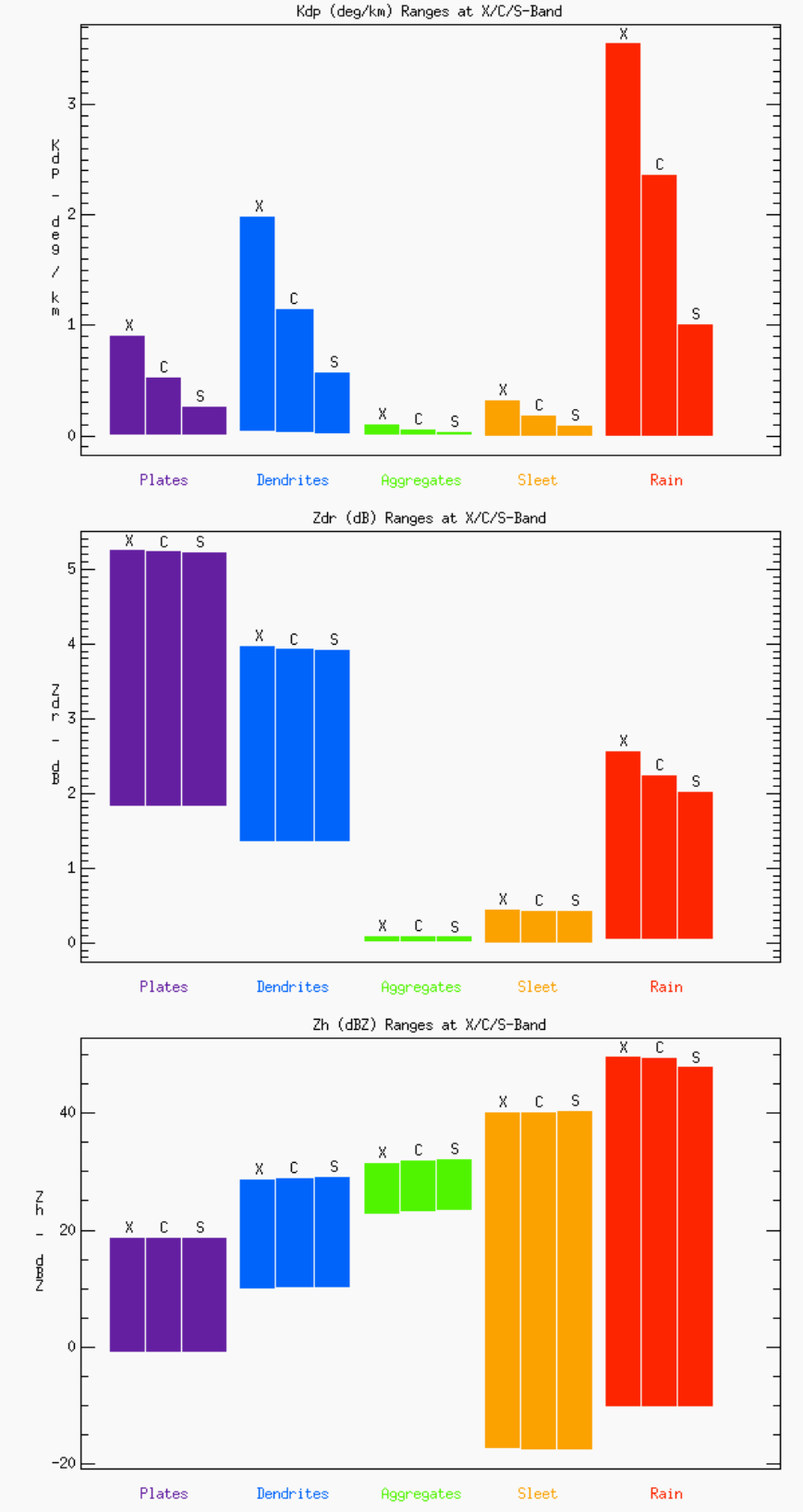

Fig. 2.2. Simulated K_{DP}, Z_{DR}, and Z_H for plates, dendrites, dry aggregated snowflakes, sleet, and rain from our electromagnetic scattering model at X-, C-, and S-band radar wavelengths.

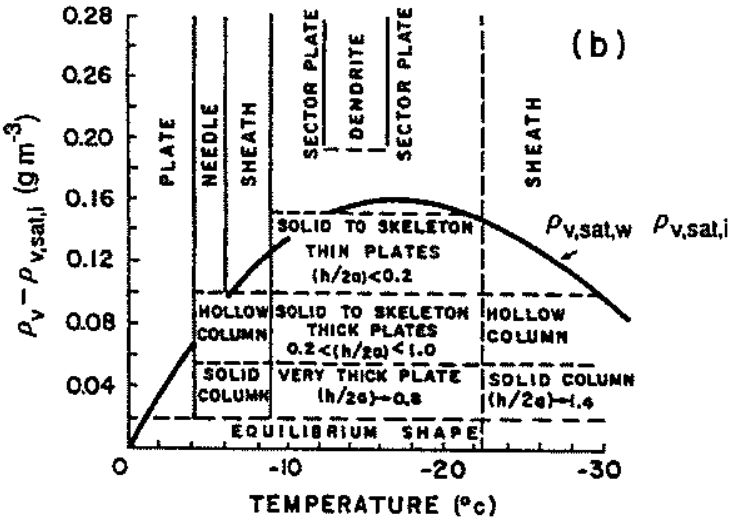

Fig. 2-36: b. Variation of ice crystal habit with temperature and vapor density excess. (Based on laboratory observations of Kobayashi, 1961; and Rottner & Vali, 1974.)

Fig. 2.3. From Pruppacher and Klett (1997).

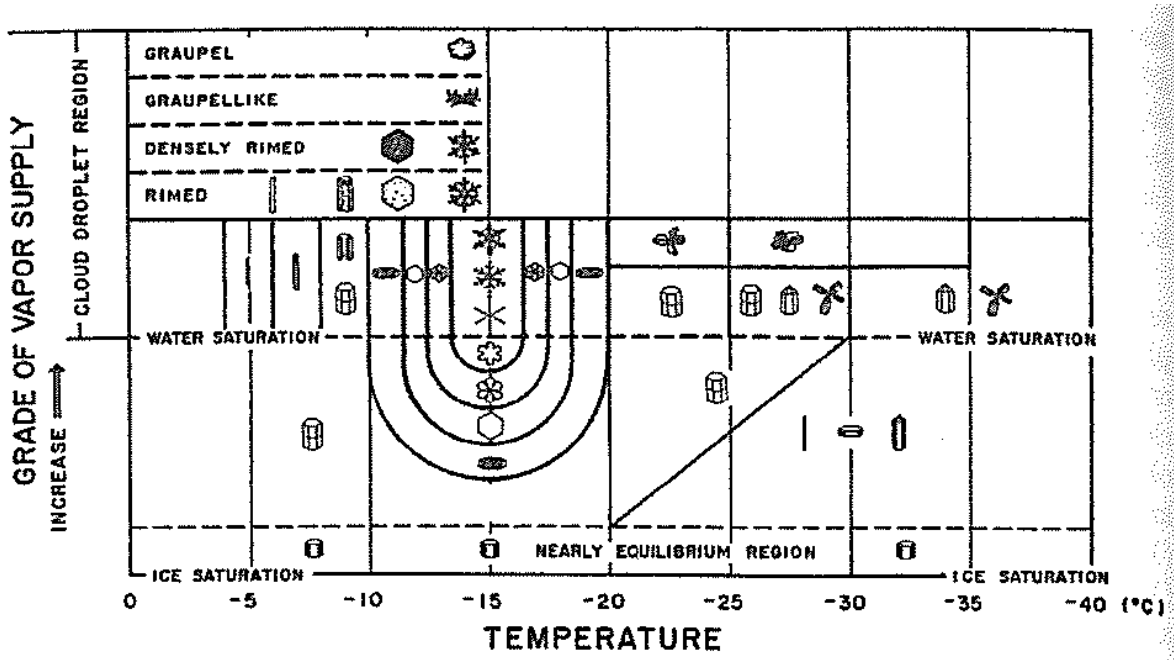

Fig. 2-37: Temperature and humidity conditions for the growth of natural snow crystals of various types. (From Magono and Lee, 1966; by courtesy of *J. Fac. Sci.*, Hokkaido University.)

Fig. 2.4. From Pruppacher and Klett (1997).

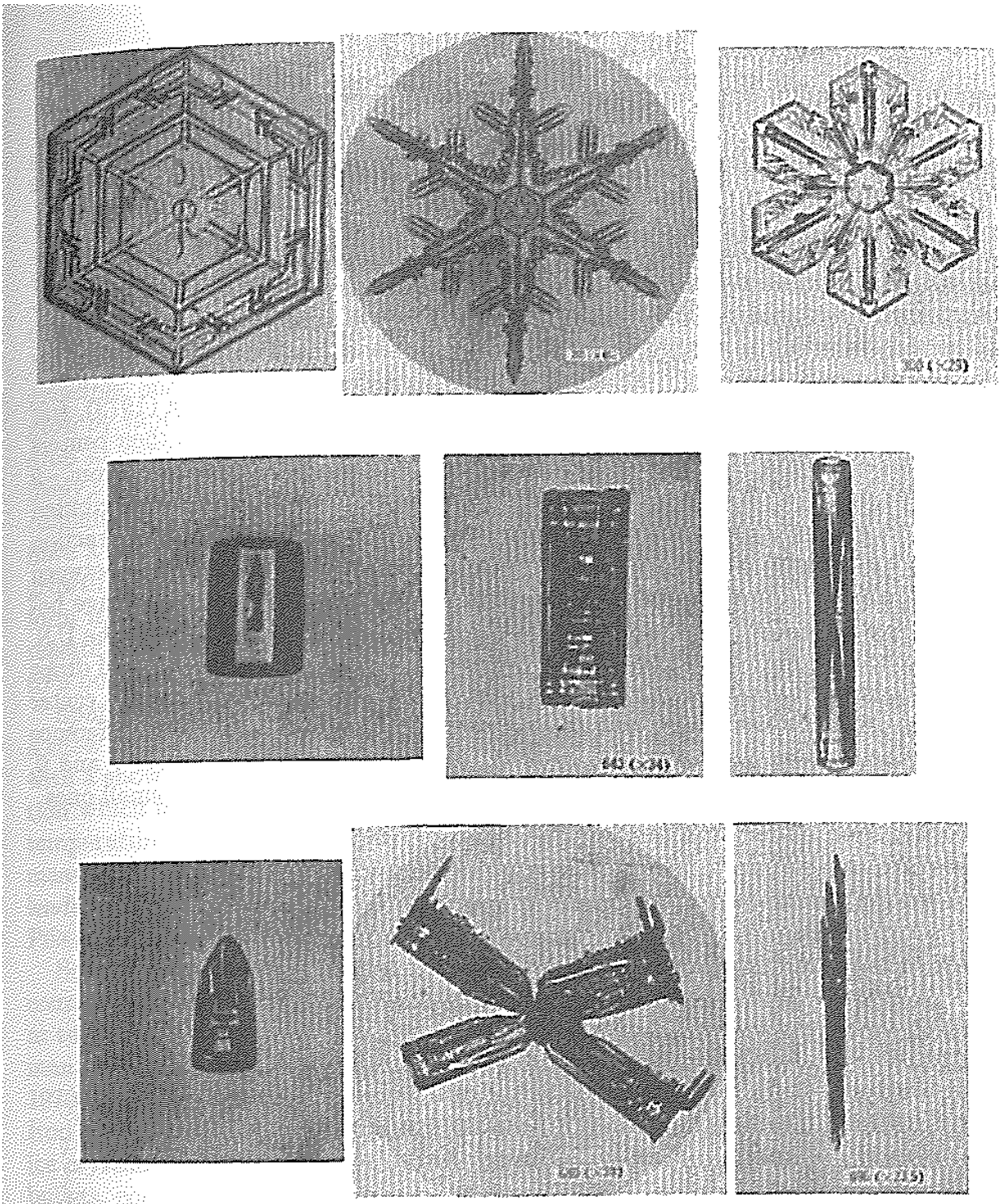

Plate 2. Major shapes of snow crystals: top row, from left to right: simple plate, dendrite, crystal with broad branches; second row, from left to right: solid column, hollow column, sheath; third row, from left to right: bullet, combination of bullets (rosette, Prismenbüschel), combination of needles. (From Nakaya, 1954; by courtesy of Harvard University Press, copyright 1954 by the President and Fellows of Harvard College.)

Fig. 2.5. From Pruppacher and Klett (1997).

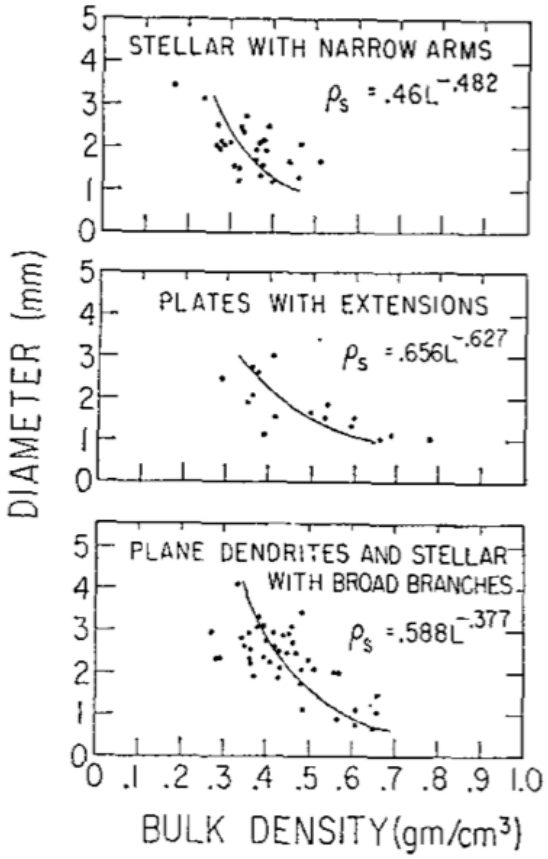

FIG. 5. Dendritic diameter vs density.

Fig. 2.6. From Heymsfield (1972).

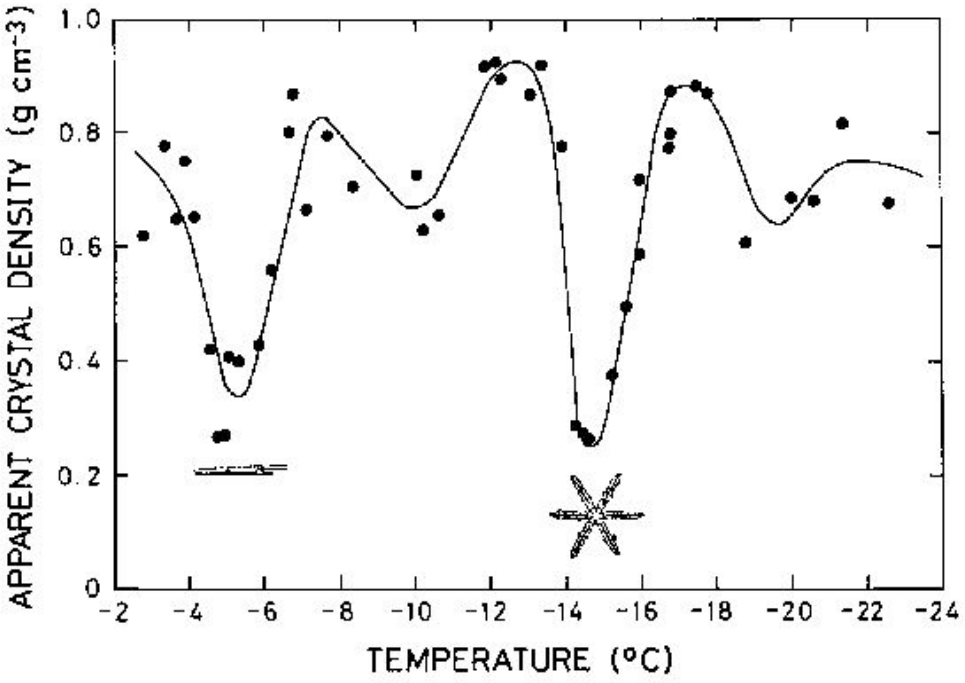

FIG. 12. Variation of apparent crystal density with temperature at the growth time of 10 min. The data were obtained by Takahashi et al. (1991).

Fig. 2.7. From Fukuta and Takahashi (1999).

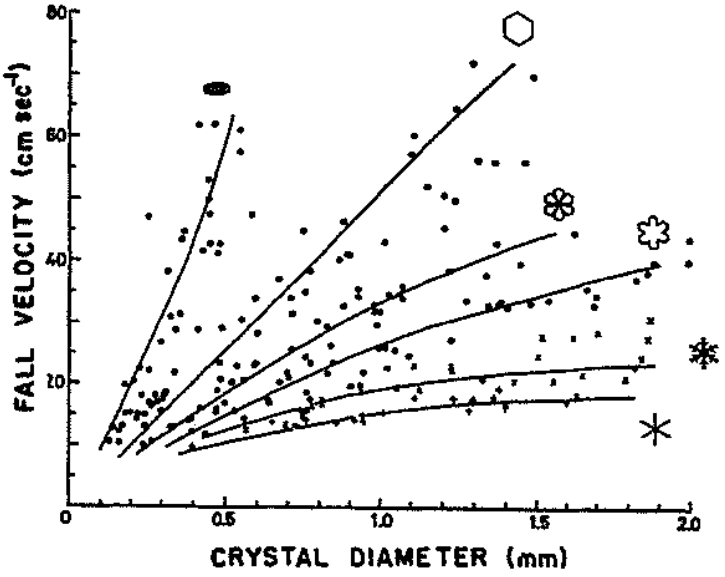

Fig. 10-42: Variation with size of observed terminal fall velocities (symbols) and velocities computed from drag data (lines) for ice crystals of various shapes, −10°C, 1000 mb. (From Kajikawa, 1972; by courtesy of *J. Meteor. Soc., Japan.*)

Fig. 2.8. From Pruppacher and Klett (1997).

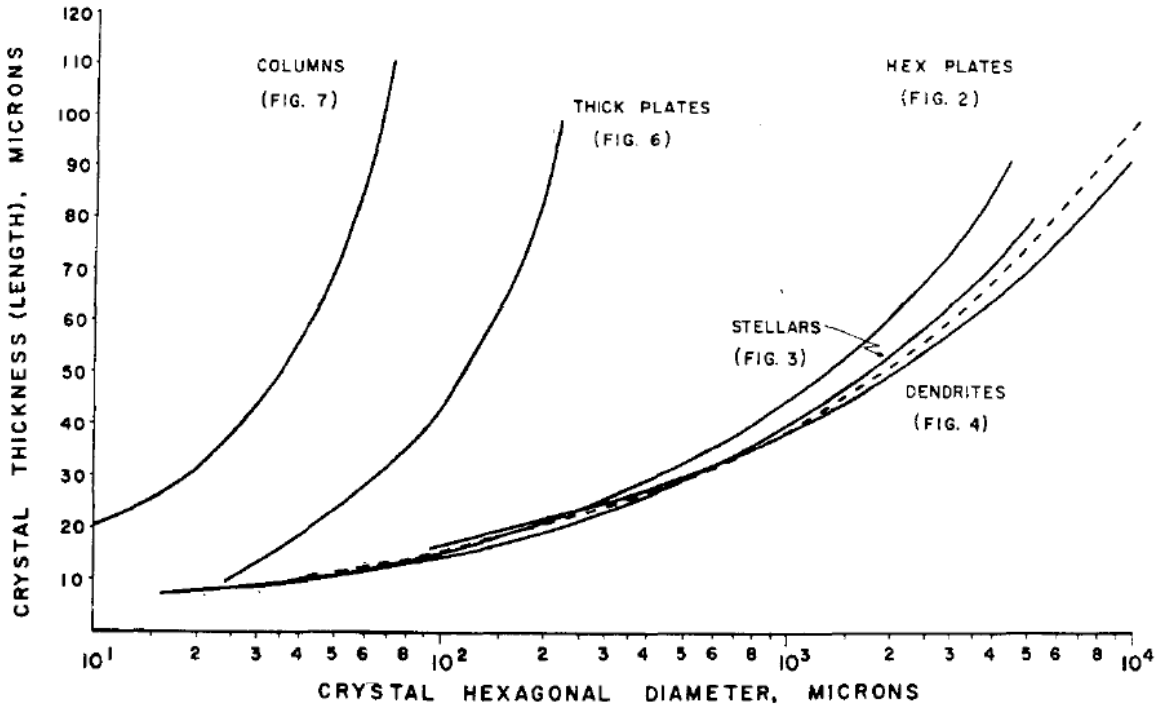

FIG. 11.—A comparison of the hexagonal diameter-thickness (length) relationships for hexagonal plates, stellars, dendrites, thick plates and columnar-type crystals. The dashed curve represents the composite plate family diameter-thickness relationship as shown in Fig. 1.

Fig. 2.9. From Auer and Veal (1970).

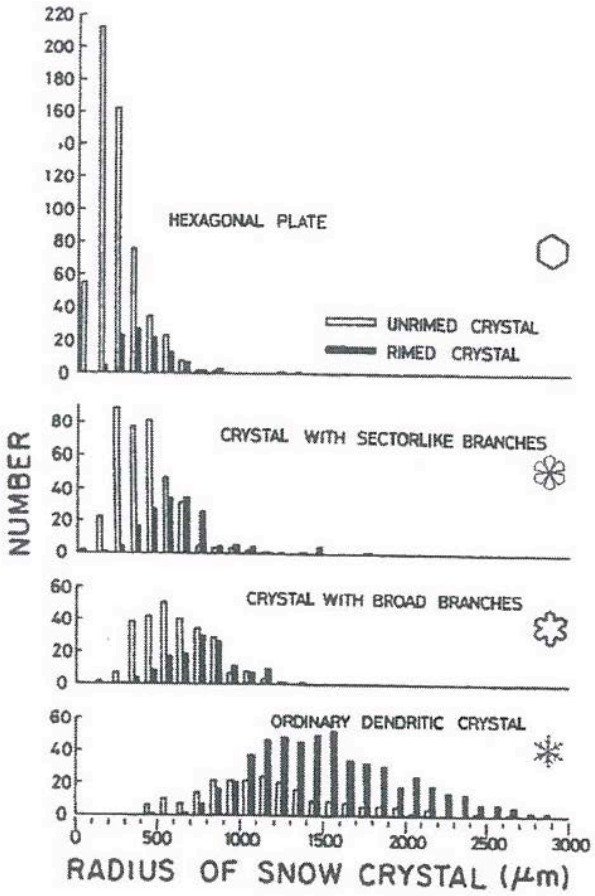

Fig. 2-53: Observed relationship between the onset of riming and the radius of planar snow crystals; open columns represent unrimed crystals; solid columns represent rimed crystals. (From Harimaya, 1975; by courtesy of the Jap. Meteor. Soc., and the author.)

Fig. 2.10. From Pruppacher and Klett (1997).

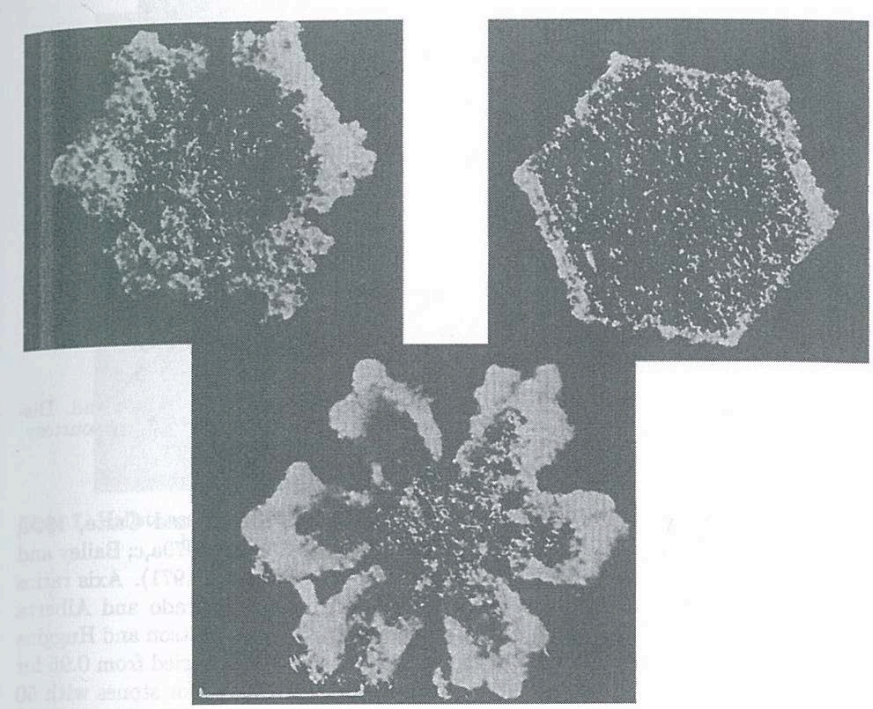

Plate 4. Rimed planar snow crystals of diameters between 2 and 3 mm. (From Hobbs et al., 1971; by courtesy of the authors.)

Fig. 2.11. From Pruppacher and Klett (1997).

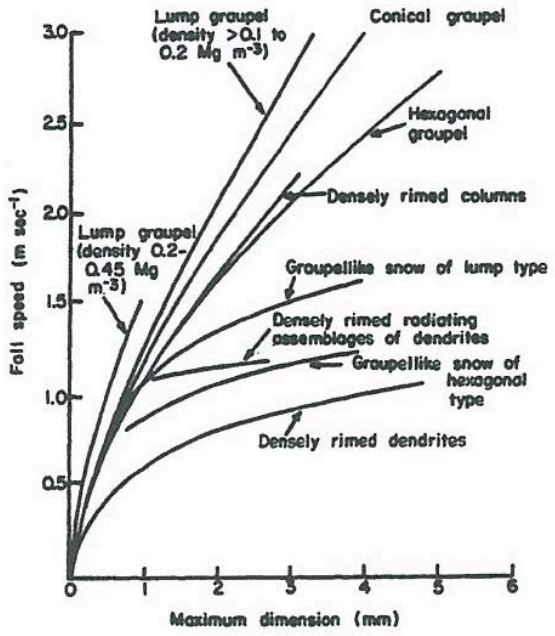

Fig. 10-44: Best fit curves for the fall velocity versus maximum dimension of graupel particles of various types. (From Locatelli and Hobbs, 1974; by courtesy of the authors; copyrighted by Am. Geophys. Union.)

Fig. 2.12. From Pruppacher and Klett (1997).

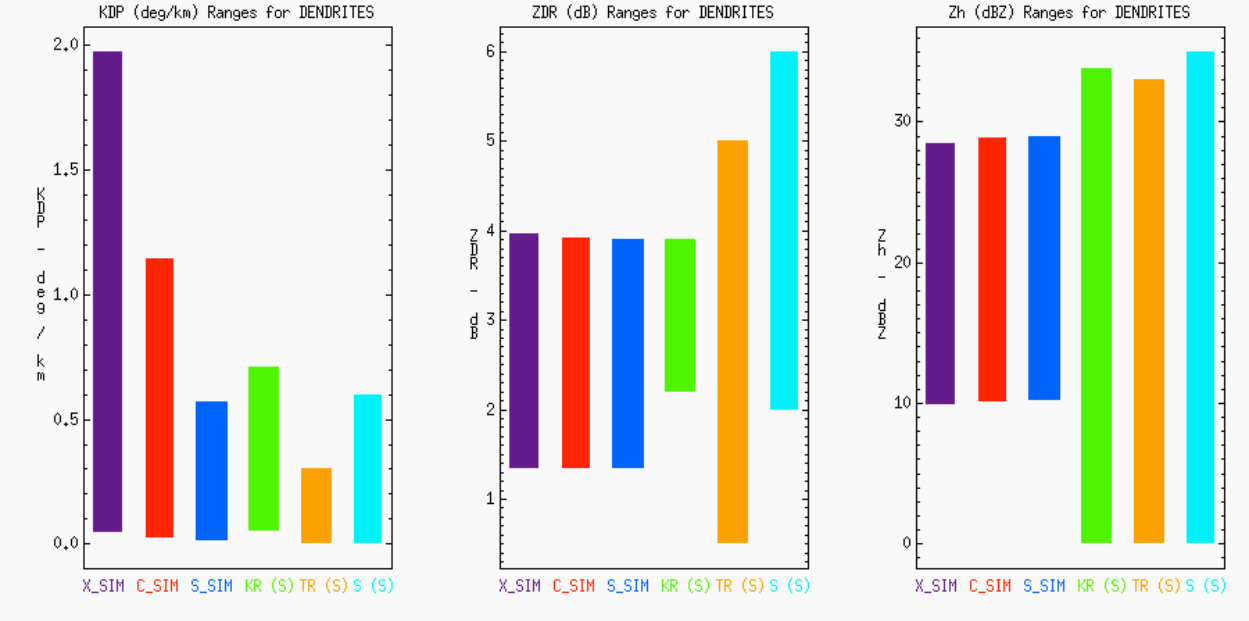

Fig. 2.13. Simulated ranges of K_{DP}, Z_{DR}, and Z_H for dendrites at X-, C-, and S-band wavelengths (X_SIM: purple, C_SIM: red, S_SIM: blue) compared to results from Kennedy and Rutledge (2011) for dendrites at S-band (green), Trapp et al. (2001) and Ryzhkov et al. (2005a) for dendrites at S-band (orange), and Straka et al. (2000) for dendrites and plates at S-band (cyan).

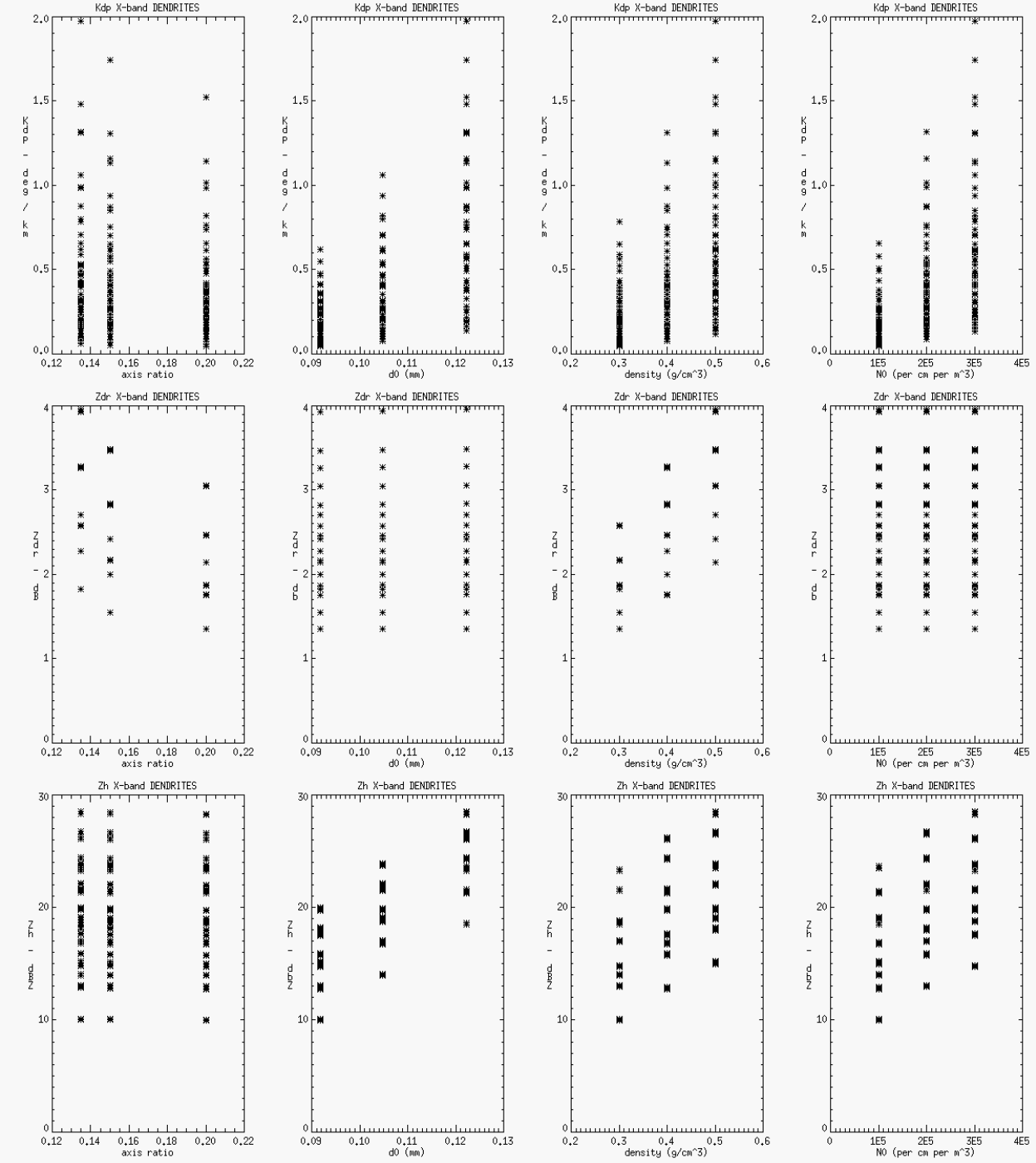

Fig. 2.14. Sensitivity scatter plots of simulated K_{DP}, Z_{DR}, and Z_H for dendrites to variable microphysical parameterizations from Table 2.1 at X-band wavelength.

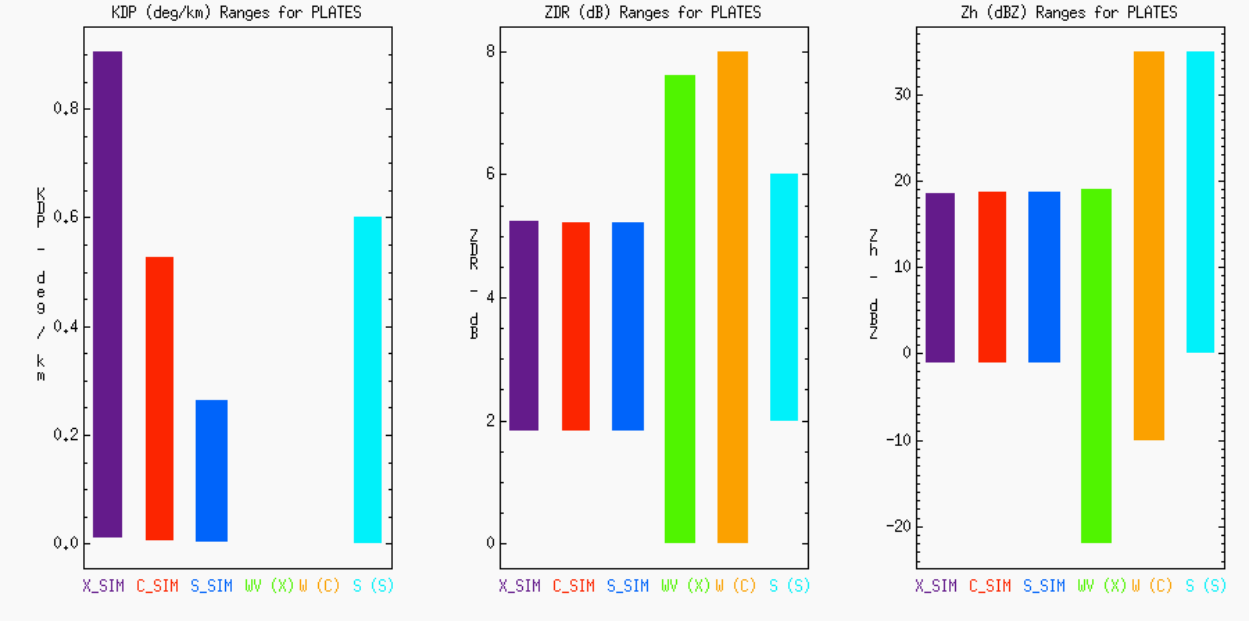

Fig. 2.15. Simulated ranges of K_{DP}, Z_{DR}, and Z_H for plates at X-, C-, and S-band wavelengths (X_SIM: purple, C_SIM: red, S_SIM: blue) compared to results from Wolde and Vali (2001) when available for plates at X-band (green), Williams et al. (2011) when available at C-band (orange), and Straka et al. (2000) for dendrites and plates at S-band (cyan).

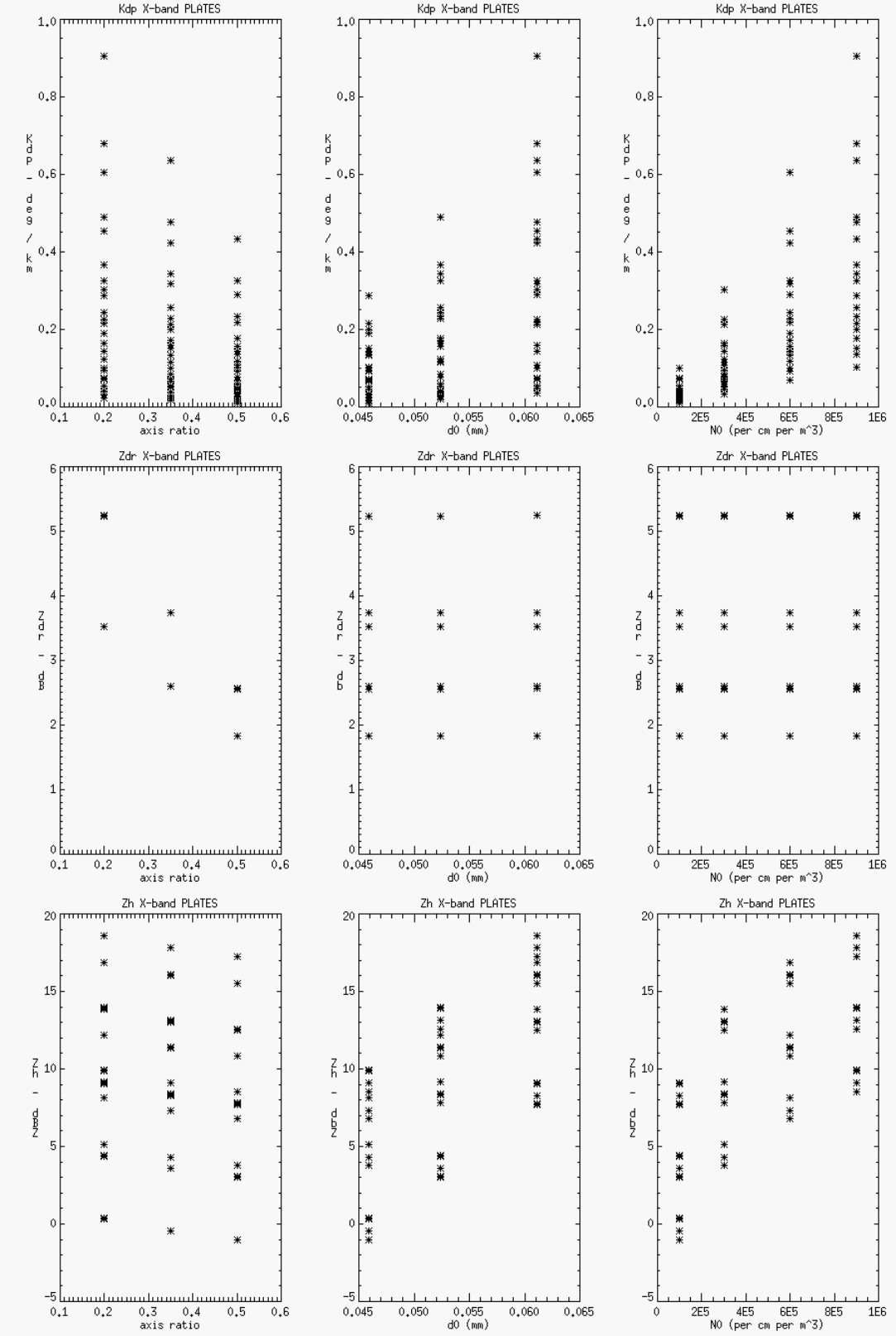

Fig. 2.16. Sensitivity scatter plots of simulated K_{DP}, Z_{DR}, and Z_H for plates to variable microphysical parameterizations from Table 2.1 at X-band wavelength.

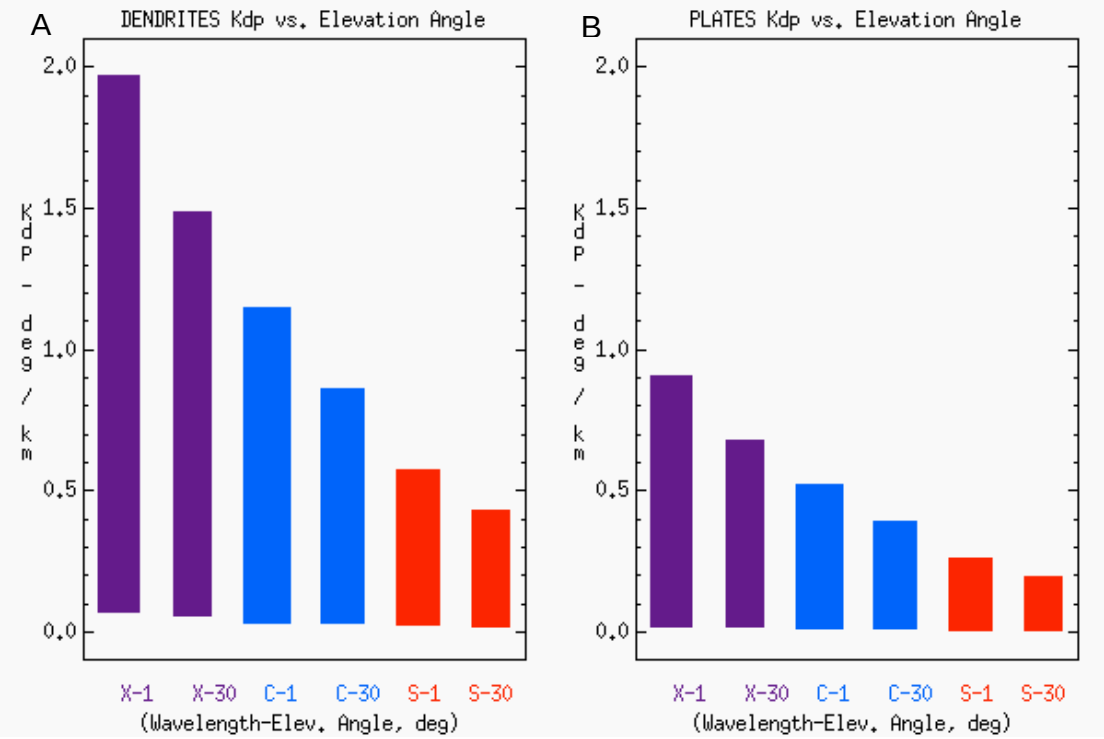

Fig. 2.17. K_{DP} dependence on simulated radar elevation angle for a) dendrites and b) plates at X-band (purple), C-band (blue), and S-band (red) wavelengths.

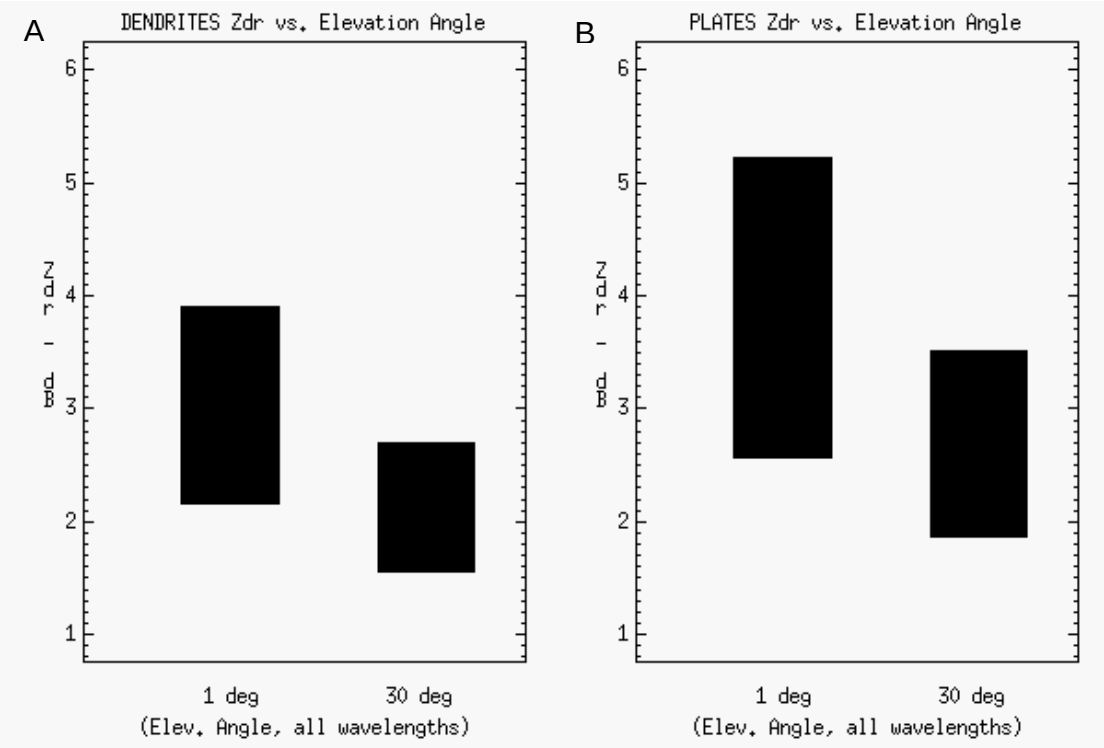

Fig. 2.18. Z_{DR} dependence on simulated radar elevation angle for a) dendrites and b) plates at X-band (purple), C-band (blue), and S-band (red) wavelengths.

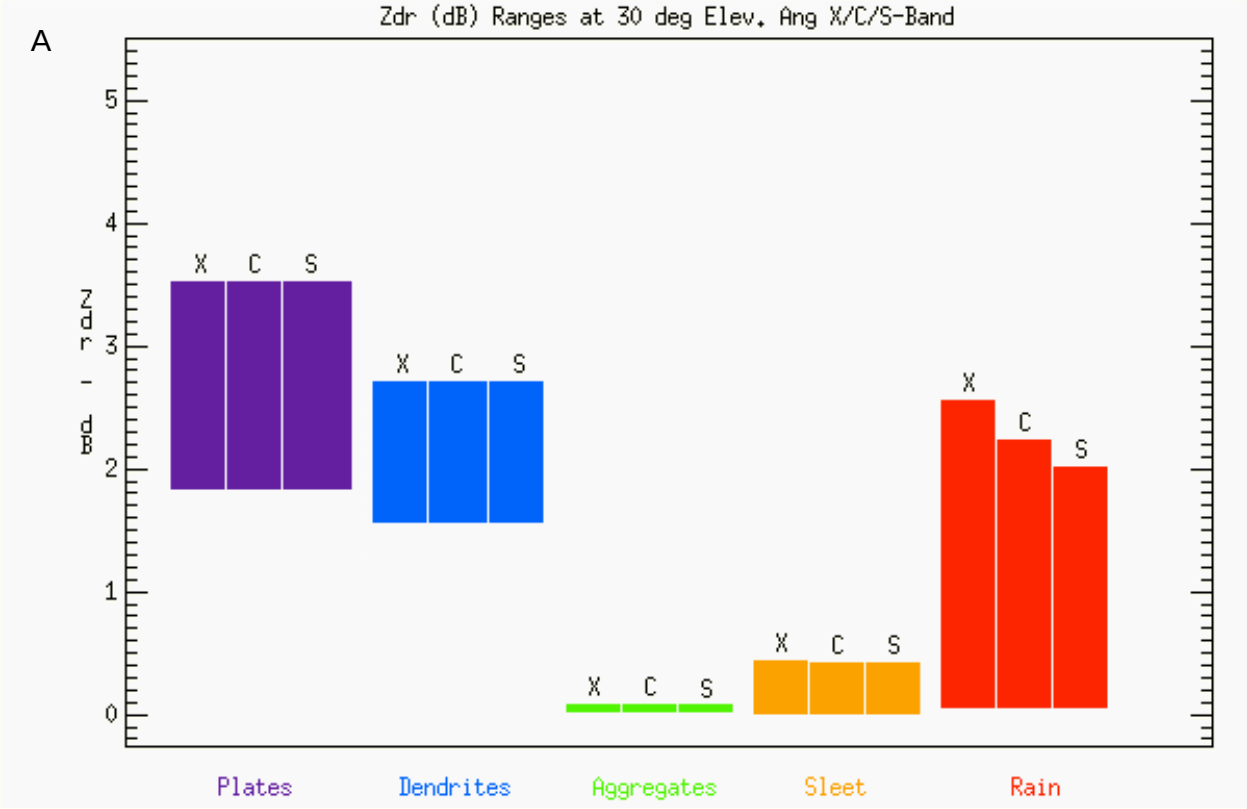

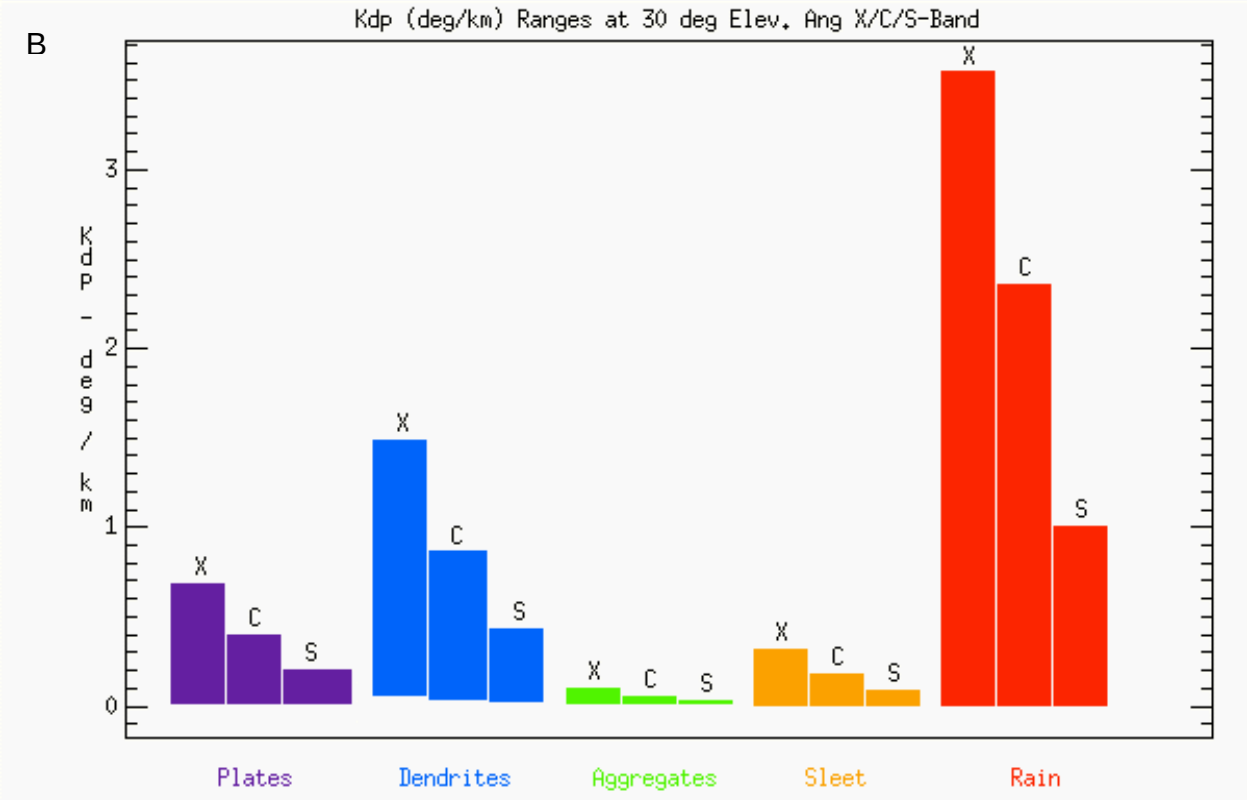

Fig. 2.19. Simulated a) K_{DP} and b) Z_{DR} for plates, dendrites, dry aggregated snowflakes, sleet, and rain from at X-, C-, and S-band radar wavelengths for 30° elevation angle only. Compare with Fig. 2.2 for scattering simulations at both 1° and 30° elevation angle.

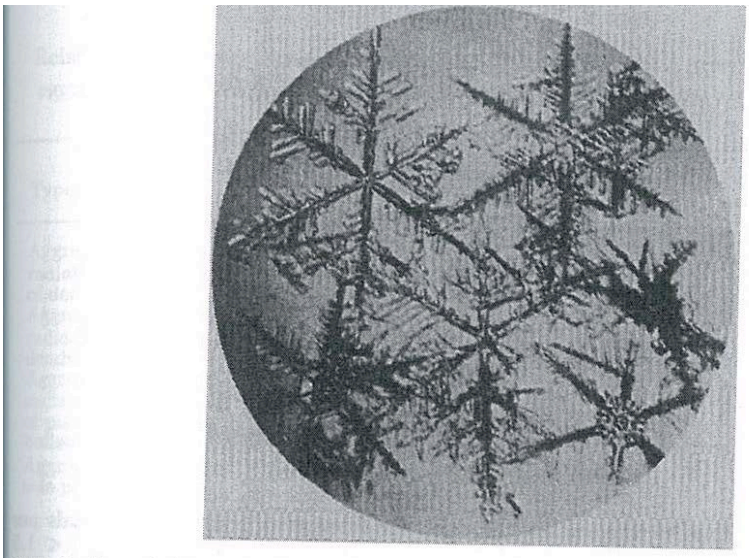

Plate 3. Snow flake consisting of dendritic crystals clinging together. (From Nakaya, 1954; by courtesy of Harvard University Press, copyright 1954 by the President and Fellows of Harvard College.)

Fig. 2.20. From Pruppacher and Klett (1997).

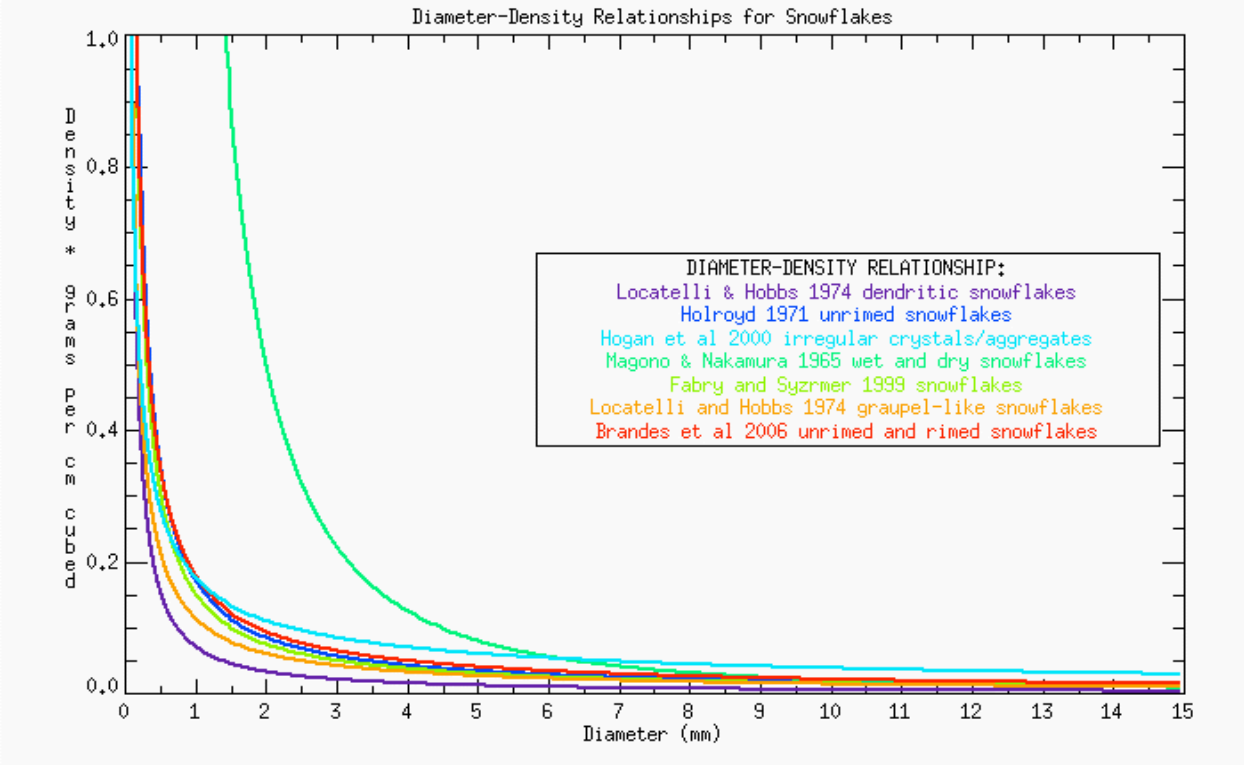

Fig. 2.21. Diameter-bulk density relationships derived from various studies.

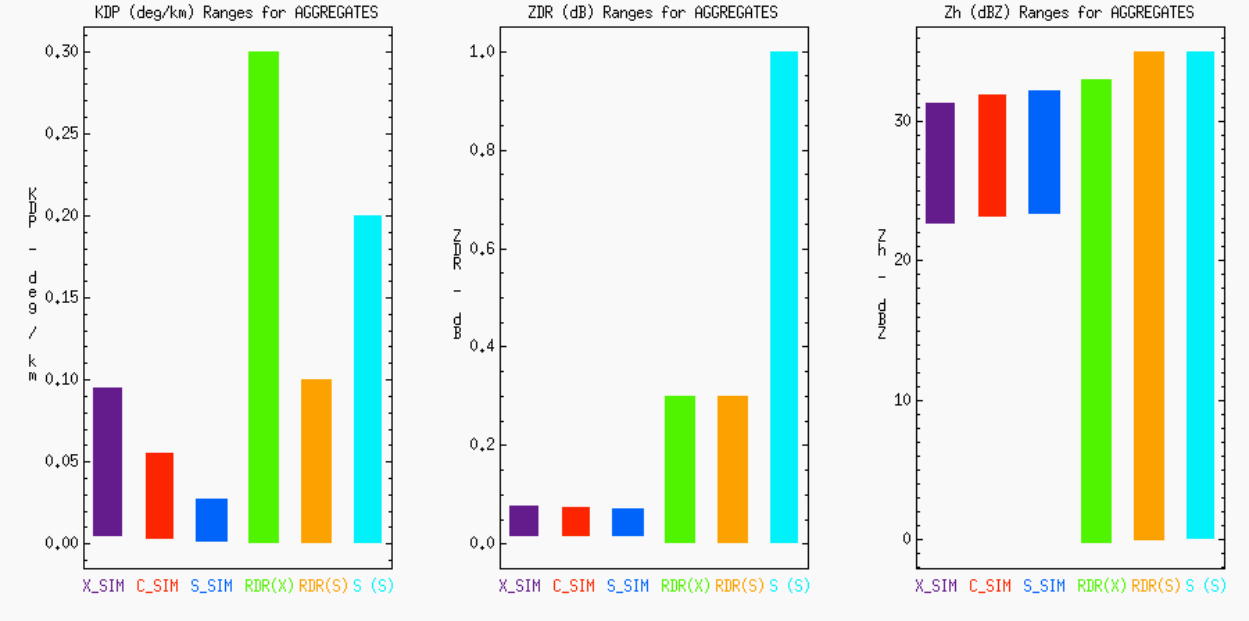

Fig. 2.22. Simulated ranges of K_{DP}, Z_{DR}, and Z_H for dry aggregated snowflakes at X-, C-, and S-band wavelengths (X_SIM: purple, C_SIM: red, S_SIM: blue) compared to results from Ryzhkov et al. (2005a) for aggregates at S-band combined where applicable with Dolan and Rutledge (2009) for aggregates at X-band (green) and S-band (orange) and Straka et al. (2000) for aggregates at S-band (cyan).

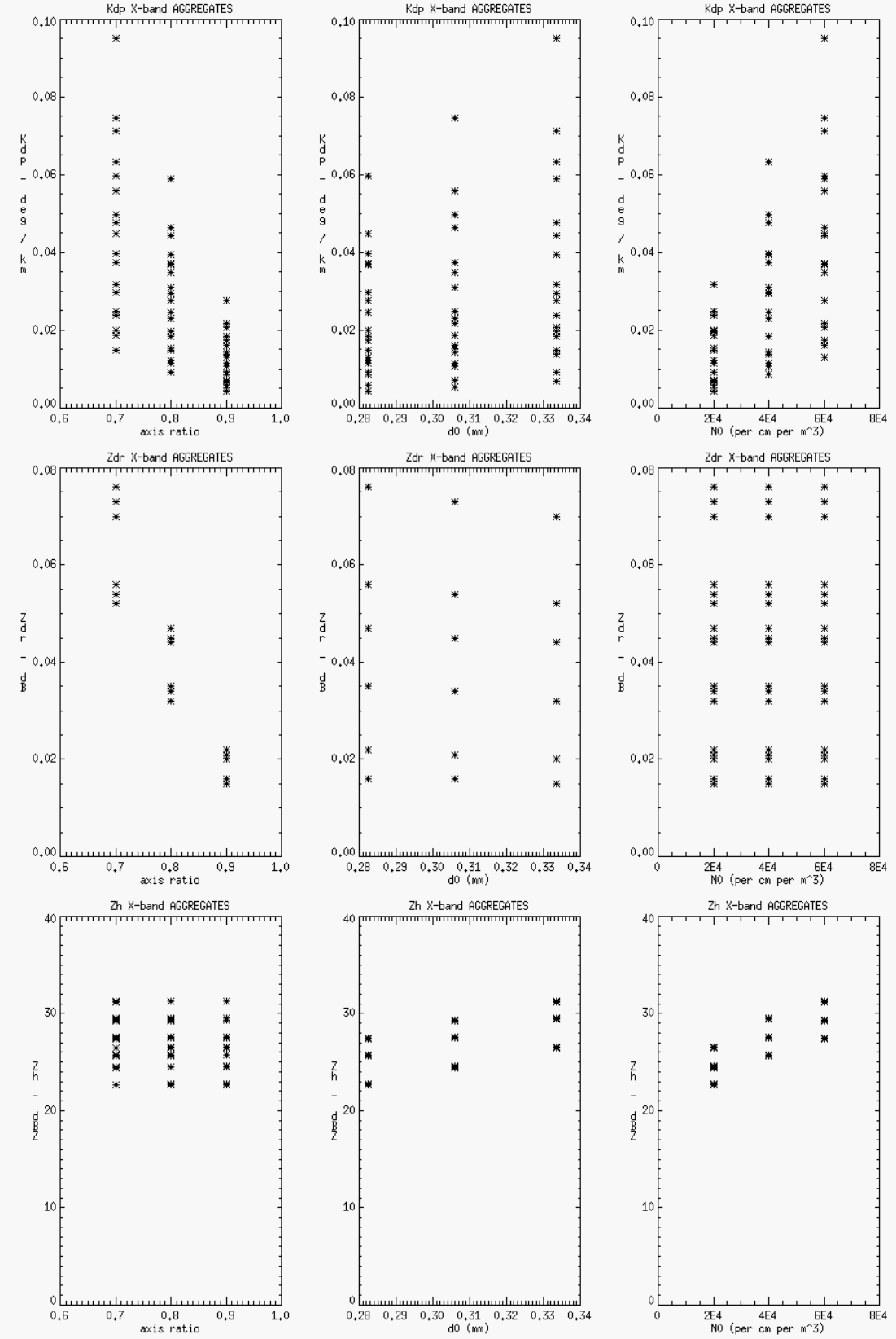

Fig. 2.23. Sensitivity scatter plots of simulated K_{DP}, Z_{DR}, and Z_H for dry aggregated snowflakes to various microphysical parameterizations from Table 2.1 at X-band wavelength.

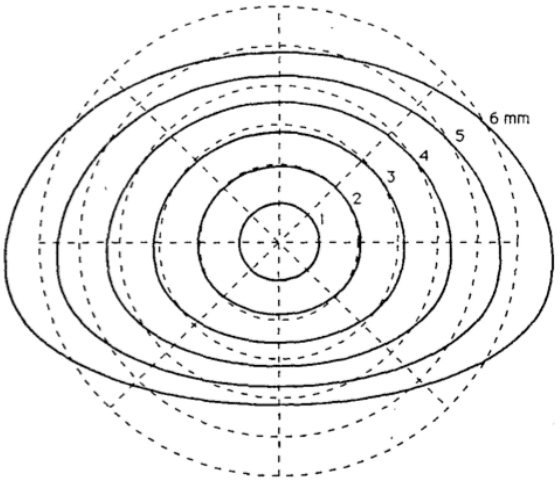

FIG. 7. Computed shapes for d = 1, 2, 3, 4, 5 and 6 mm with origin at center of mass. Shown for comparison are dashed circles of diameter d divided into 45 degree sectors.

Fig. 2.24. From Beard and Chuang (1987).

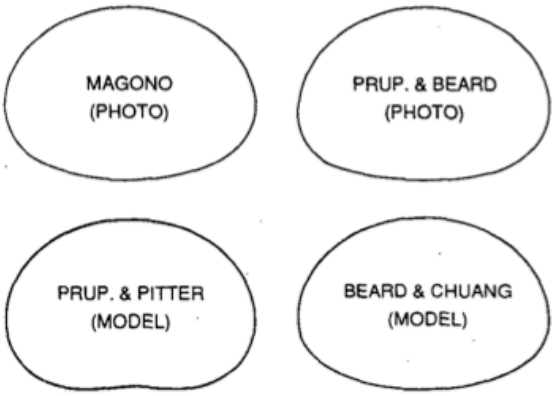

FIG. 10. Comparison of drop profiles (taken from photos) with model results for d = 5 mm.

Fig. 2.25. From Beard and Chuang (1987).

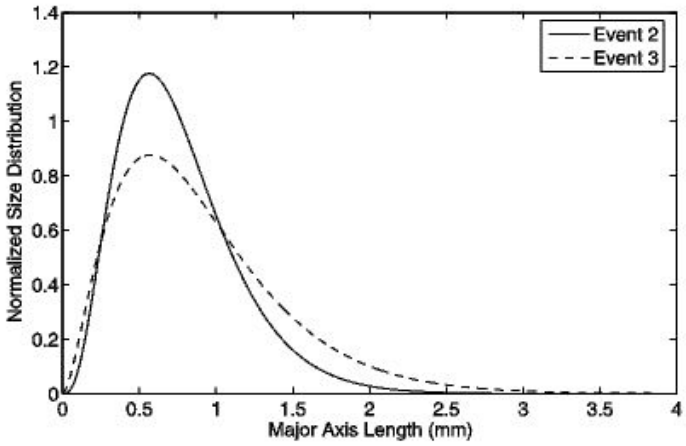

Figure 10. Normalized distribution of ice pellets (with respect to area under the curve) as a function of mean hydrometeor diameter (for Events 2 and 3.

Fig. 2.26. From Gibson et al. (2009).

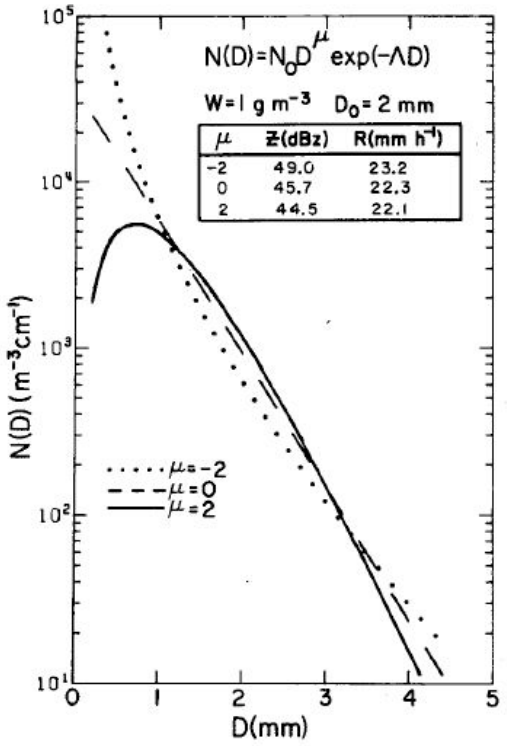

FIG. 2. Examples of the gamma raindrop size distribution for $\mu = -2$, 0 and 2 and with liquid water content $W = 1$ g m^{-3} and median volume diameter $D_0 = 2$ mm. The inset table shows the corresponding values of radar reflectivity factor (Rayleigh approximation) and rainfall rate.

Fig. 2.27. From Ulbrich (1983).

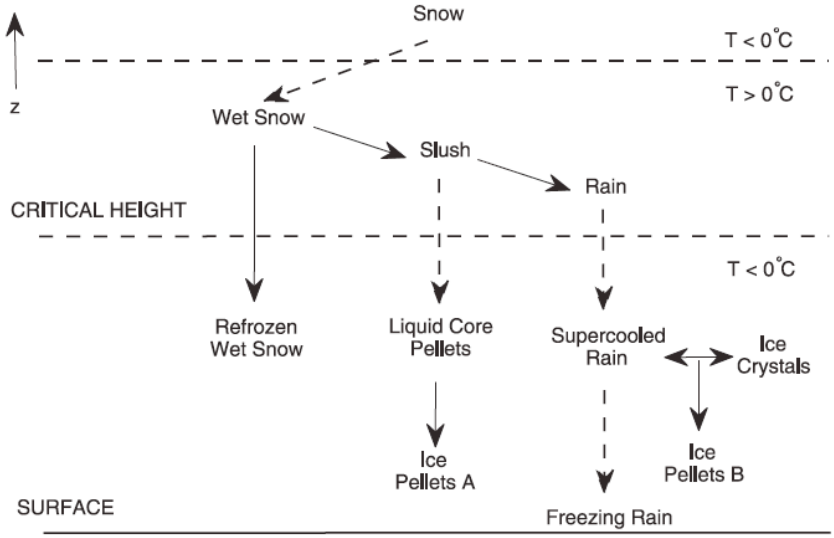

FIG. 1. Schematic diagram of the evolution of precipitation types when falling through the melting layer and the refreezing layer below it. The critical height is indicated as well as the temperature of the atmospheric layers. The solid line is the ground level. The solid arrows between precipitation types category indicate a change of prognostic variables. The dashed arrows indicate that the name of the precipitation changes but they are the same prognostic variables.

Fig. 2.28. From Thériault et al. (2010).

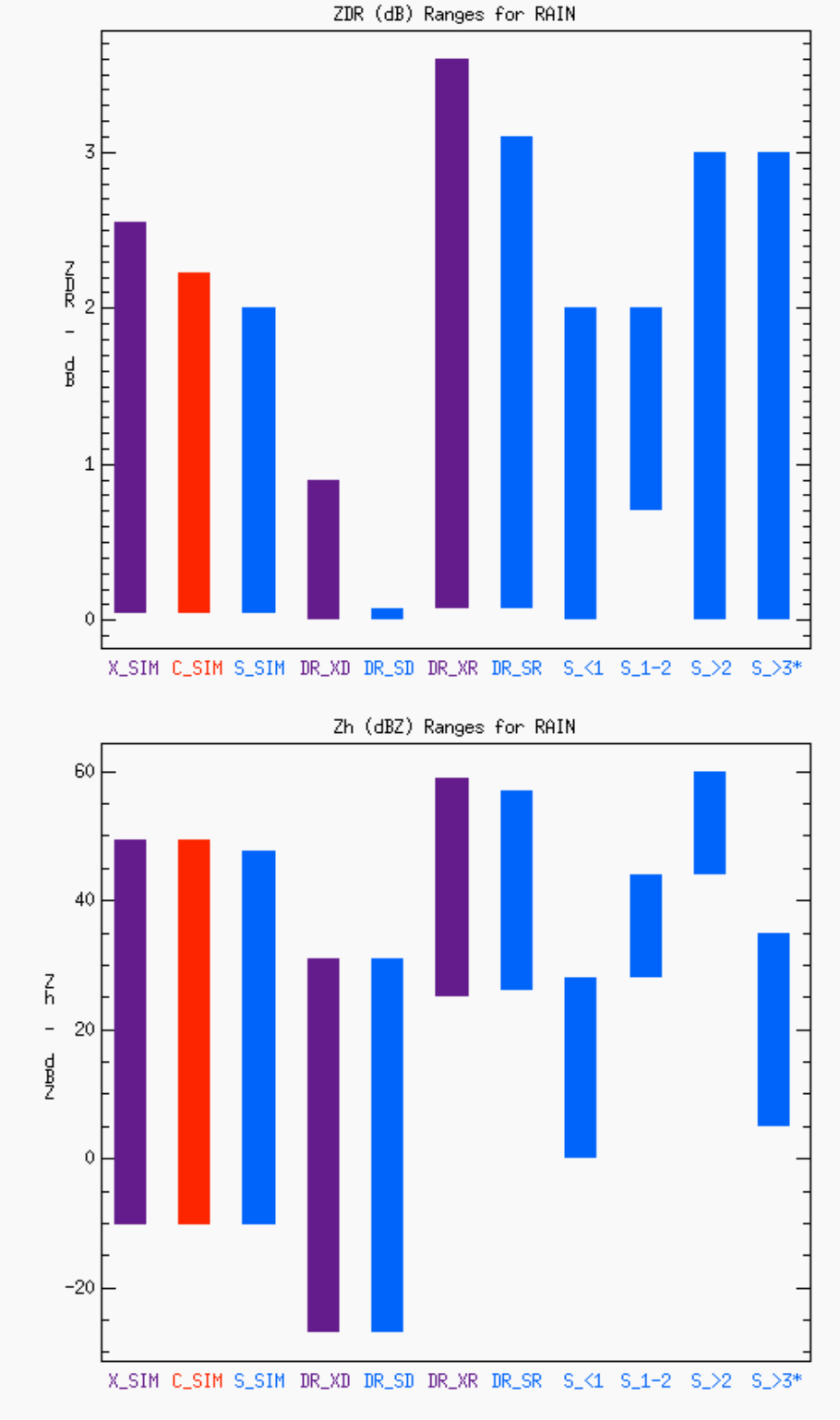

Fig. 2.29. Simulated ranges of Z_{DR} and Z_H for sleet at X-, C-, and S-band wavelengths (X_SIM: purple, C_SIM: red, S_SIM: blue) compared to results from Dolan and Rutledge (2009) for drizzle and convective-regime rain at X-band (purple) and S-band (blue) and from Straka et al (2000) for rain with $D_0 < 1$ mm, 1 mm $< D_0 < 2$ mm, $D_0 > 2$ mm, and $D_0 > 3$ mm with large drops at low number concentrations at S-band (blue).

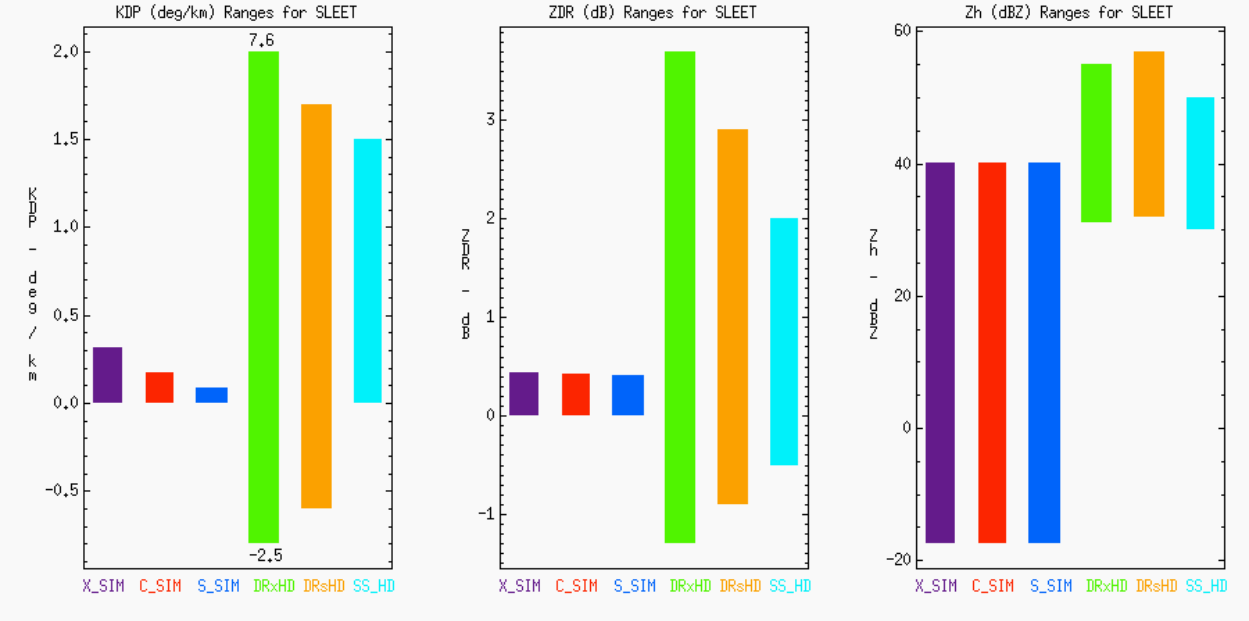

Fig. 2.30. Simulated ranges of K_{DP}, Z_{DR}, and Z_H for sleet at X-, C-, and S-band wavelengths (X_SIM: purple, C_SIM: red, S_SIM: blue) compared to results for high-density graupel from Dolan and Rutledge (2009) at X-band (green) and S-band (orange) and from Straka et al. (2000) at S-band (cyan).

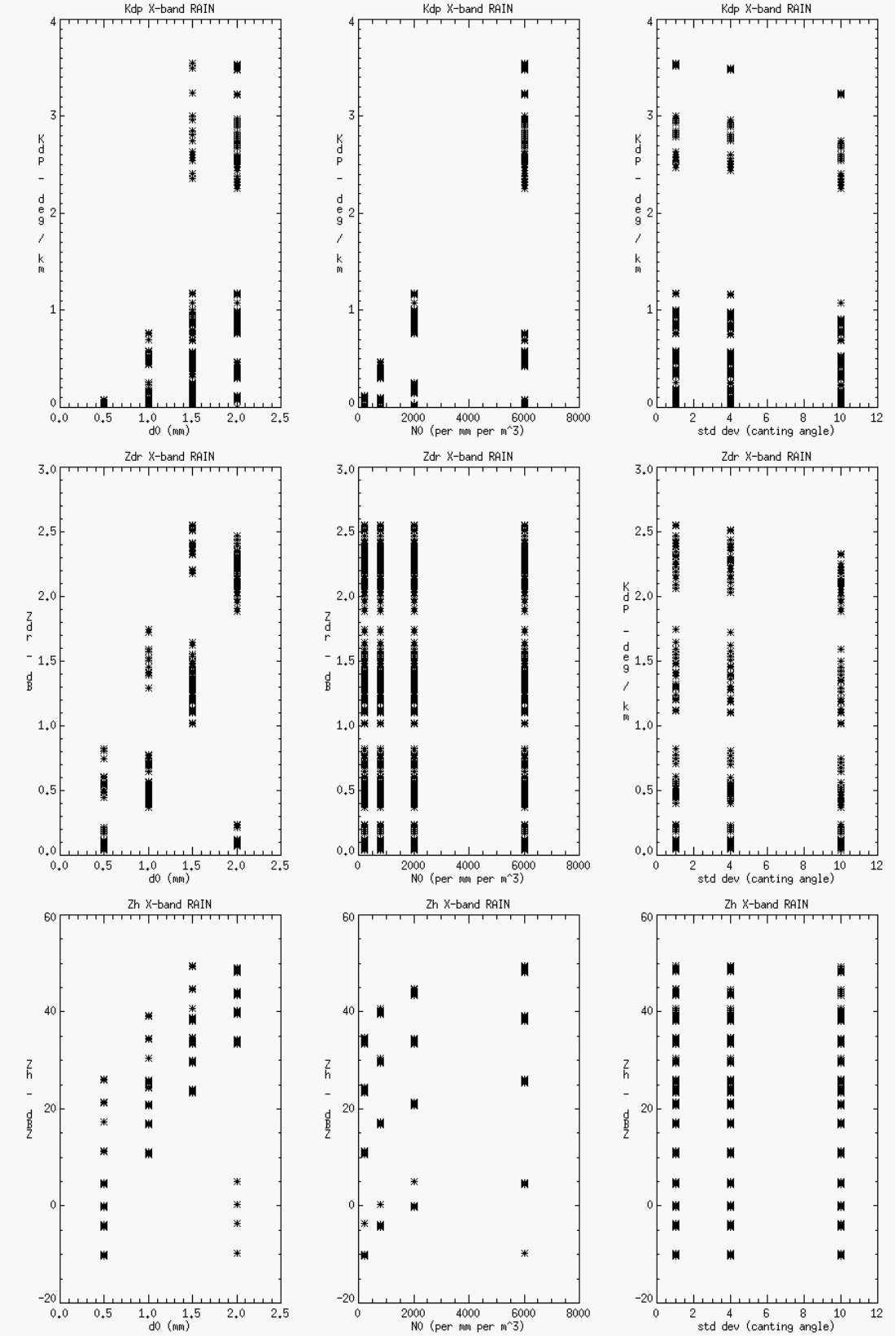

Fig. 2.31. Sensitivity scatter plots of simulated K_{DP}, Z_{DR}, and Z_H for rain to various microphysical and radar parameterizations from Table 2.1 at X-band wavelength.

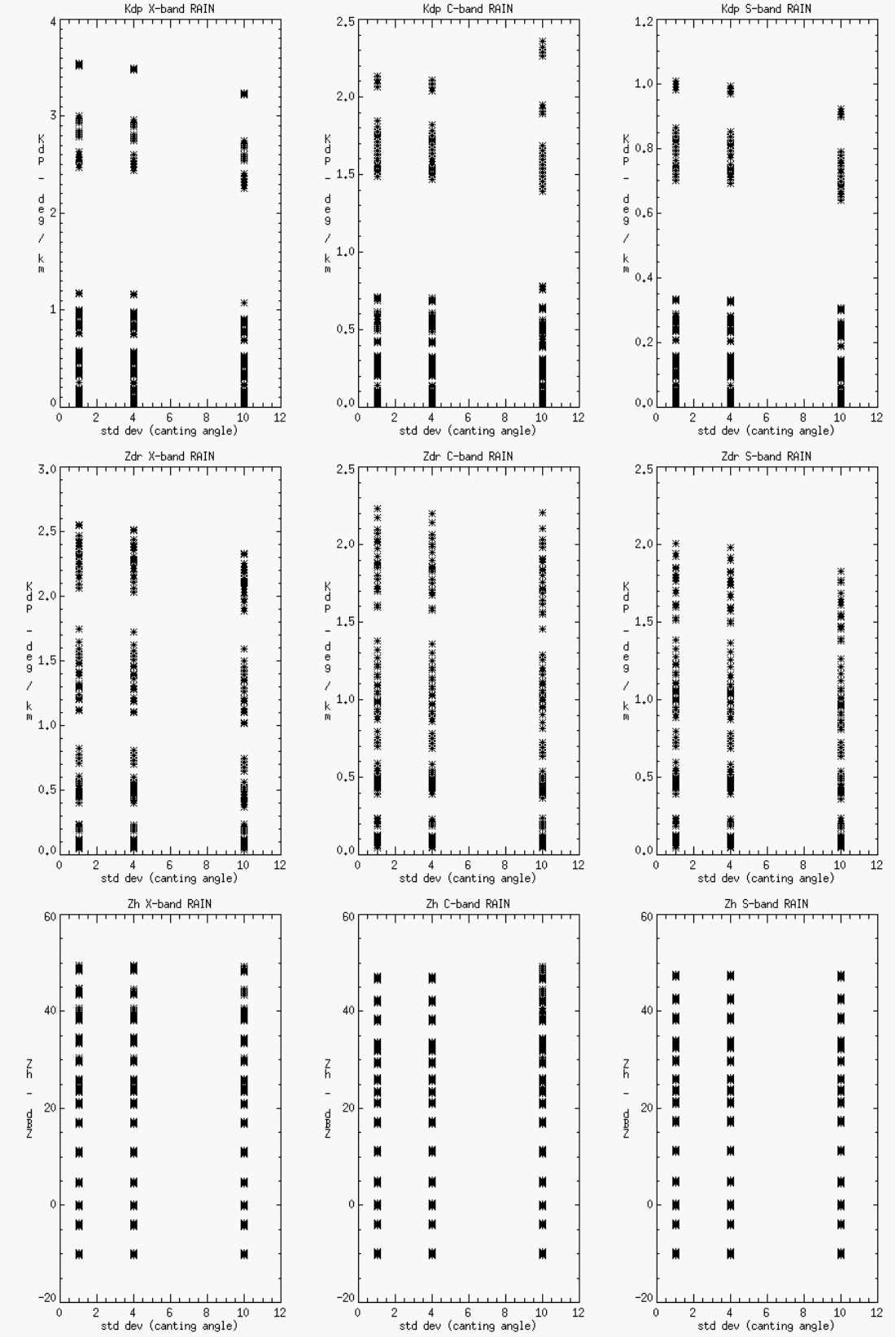

Fig. 2.32. Sensitivity scatter plots of simulated K_{DP}, Z_{DR}, and Z_H for rain to standard deviation of canting angle for X-, C-, and S-band wavelengths.

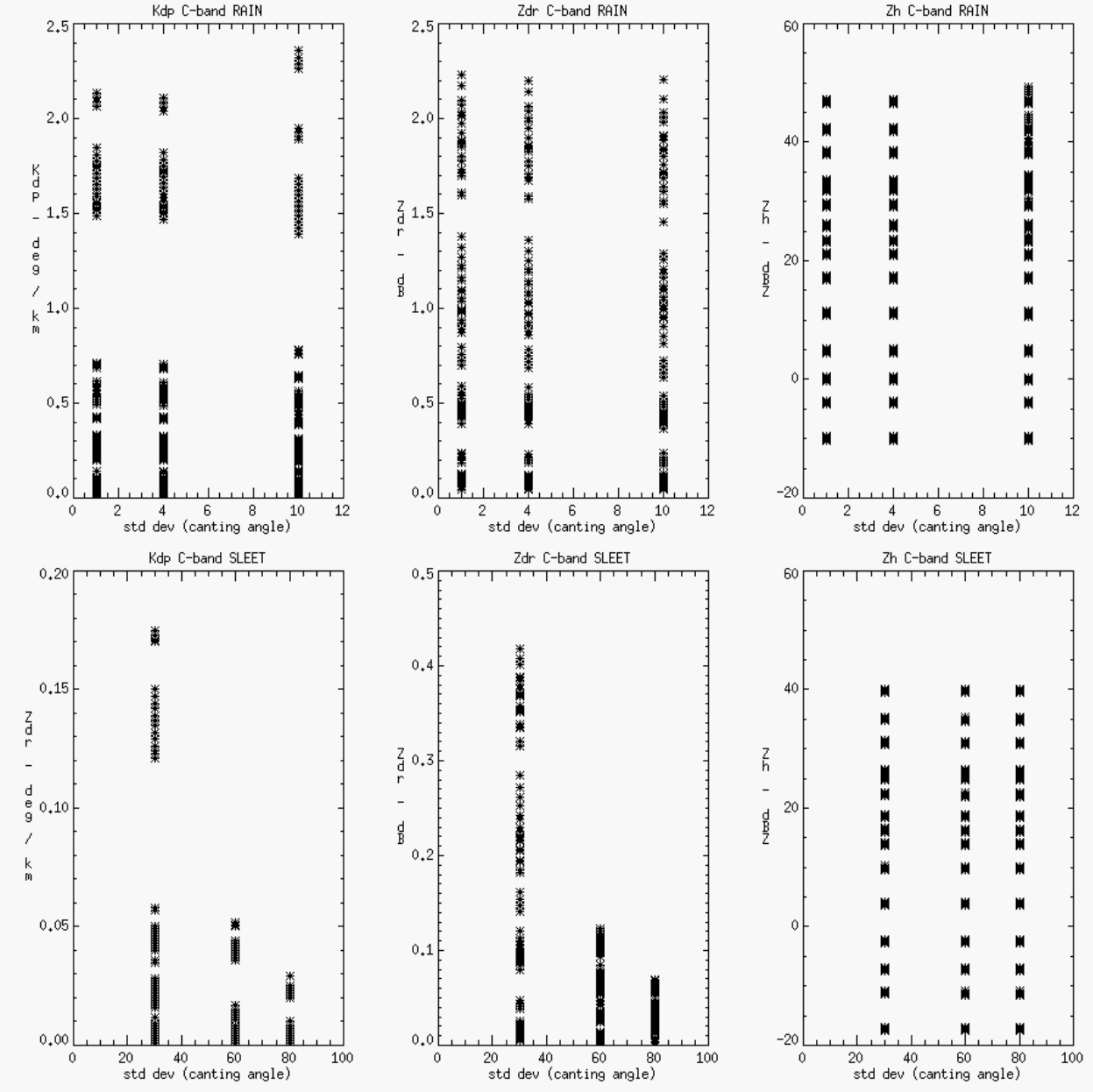

Fig. 2.33. Sensitivity scatter plots of simulated K_{DP}, Z_{DR}, and Z_H for sleet and rain to standard deviation of canting angle at C-band wavelength.

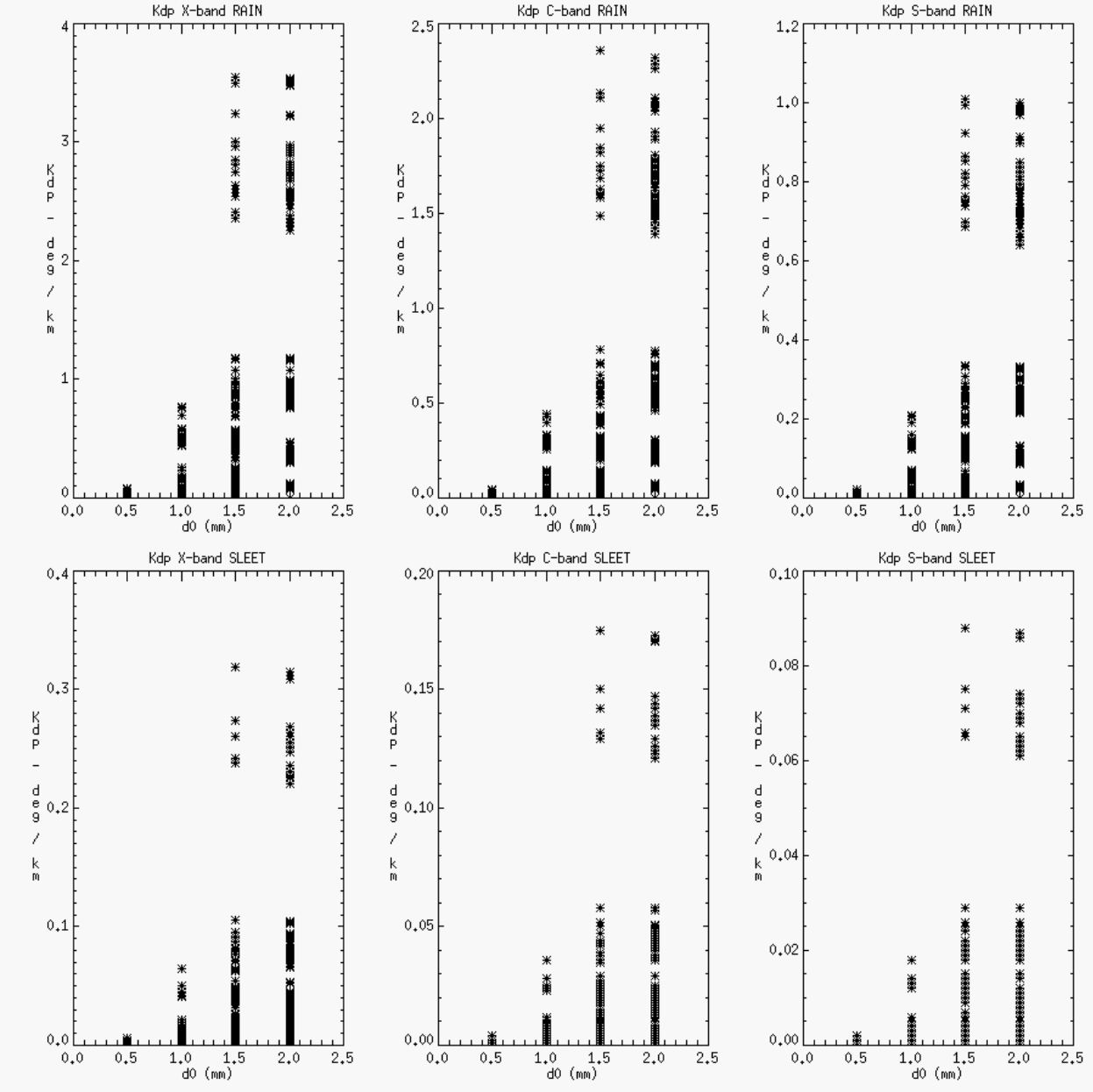

Fig. 2.34. Sensitivity scatter plots of simulated K_{DP} for rain and sleet to D_0 at X-, C-, and S-band wavelengths.

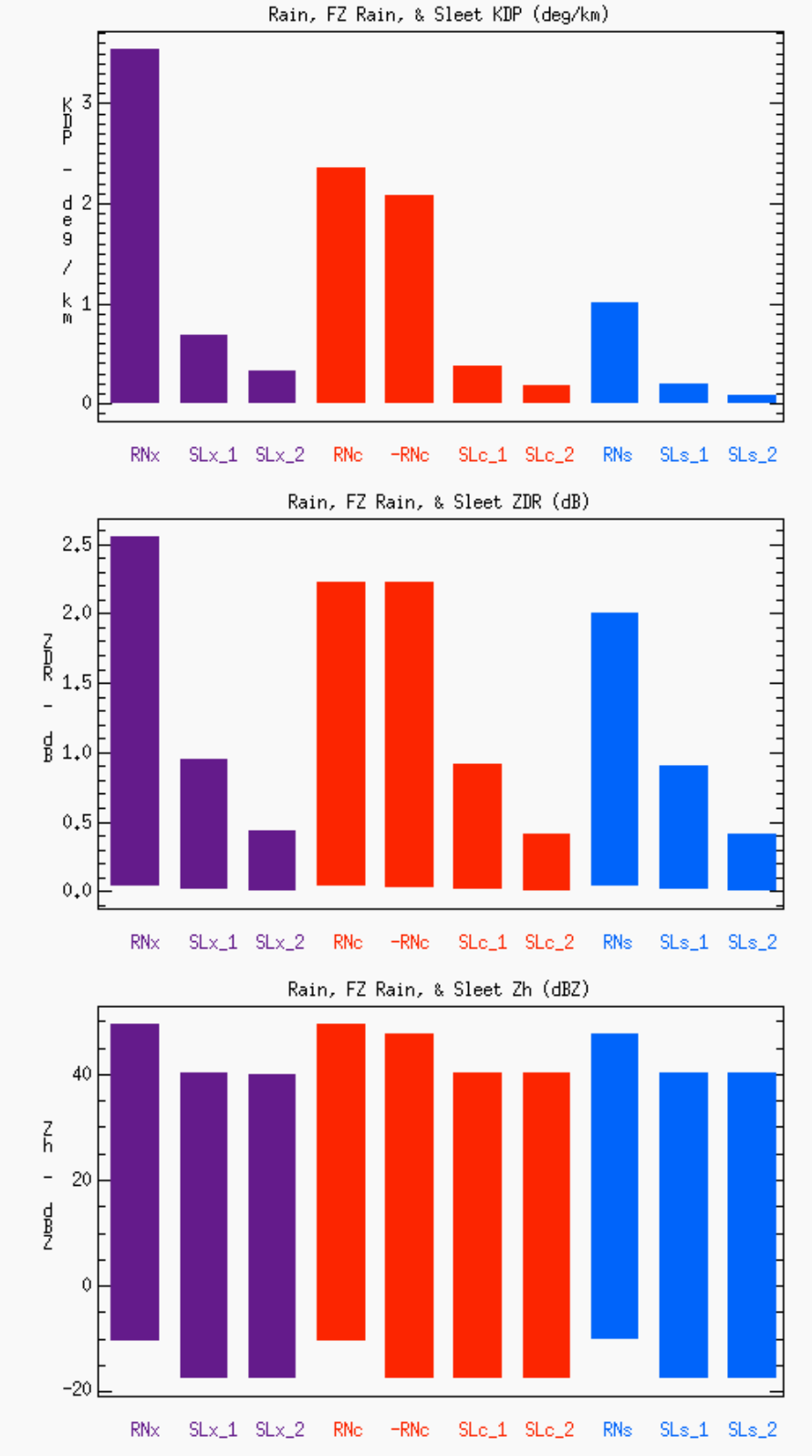

Fig. 2.35. Simulated ranges of K_{DP}, Z_{DR}, and Z_H for rain (RN), freezing rain (-RN) at C-band only, sleet with fall behavior of rain (SL_1) and sleet with realistic, tumbling fall behavior of graupel (SL_2) at X- (purple), C- (red), and S-band (blue) wavelengths.

CHAPTER THREE

Development of Melting Layer Detection and Hydrometeor Identification Algorithms

3.1 Radar specifications and winter storm case studies

This winter hydrometeor classification algorithm (HCA) was tested with three different polarimetric radar systems at three different operating frequencies using radar observations from three different winter storms. Table 3.1 shows the various radar specifications, with KOUN listed simply as a reference. Volume Coverage Patterns (VCPs) for each radar used in this study are illustrated in Fig. 3.1. Table 3.2 contains a summary of each precipitation event. The CASA (Collaborative Adaptive Sensing of the Atmosphere) IP1 (Integrated Project One) network in southwestern Oklahoma includes four X-band dual-polarized radars with overlapping domains (McLaughlin et al. 2009, Junyent et al. 2010). According to the Oklahoma radar map in Fig. 3.2, the CASA network falls within the larger range of OU-PRIME (University of Oklahoma Polarimetric Radar for Innovations in Meteorology and Engineering, OKU), a C-band radar in Norman, OK. Both systems took measurements during a freezing rain and sleet event on 28 January 2010 as well as a transition event between rain to blizzard conditions on 24 December 2009. CSU-CHILL (Colorado State University, originally developed by the Universities of Chicago and Illinois) is a S- and X-band dual-wavelength, dual-polarized radar in Greeley, CO. This radar captured simultaneous dual-wavelength observations of a snowstorm along the Front Range of the Rocky Mountains on 3 February 2012. CSU-CHILL and OU-PRIME performed routine vertical cross-section scans (RHI – Range Height Indicator) at predefined azimuths. Since this type of scan is helpful to discern the vertical distribution of polarimetric variables, RHIs were also reconstructed from CASA PPI scans. OU-PRIME and CSU-CHILL at X-band do

not have dense enough upper-level volume coverage patterns with which meaningful, additional RHIs can be made. Hydrometeor classification algorithms at various wavelengths for the same meteorological phenomena are developed and evaluated with these rich datasets.

3.2 Radar data processing and quality assurance

Quality control and post-processing efforts to produce comparable Z_H, Z_{DR}, K_{DP}, and ρ_{HV} between each radar system are briefly discussed. The specific differential phase (K_{DP}) was calculated for each radar system using the Wang and Chandrasekar (2009) method contained in the DROPS module. K_{DP} is only calculated where $\rho_{HV} > 0.75$ (CASA) or 0.80 (CHILL and OU-PRIME) to exclude non-meteorological echo and regions of the melting layer where polarimetric radar variables fluctuate too rapidly for reliable determination of K_{DP}. DROPS was also used to calculate the signal to noise ratio (*SNR*).

Each of the three CASA radars operating during the 2009 and 2010 winter storms required an individual Z_{DR} bias correction. The corrections in Table 3.3 were determined by analyzing many Z_{DR} histograms from the dry aggregated snowflake region above the melting layer, within which Z_{DR} should be approximately zero (Ryzhkov et al. 2005b, Brandes and Ikeda 2004). This manual correction method approaches the ideal 0.1 dB accuracy standard, except during situations with differential attenuation at increasing range beyond the melting level or a wet/iced over radome. Ideally, zenith pointing radars are used to determine the Z_{DR} bias, but CASA's maximum elevation angle is less than 30°. Z_{DR} should be nearly zero in drizzle for scanning radars at any elevation angle, but Giangrande and Ryzhkov (2004) show that Z_{DR} during light rain can exceed 0.5 dB because drizzle only constitutes a small fraction of the total precipitation volume.

Although CASA's gate spacing (100 m) provides fairly high radial resolution, the beam width is relatively large (1.8 deg). Non-uniform beam filling degrades the polarimetric variables beyond ~25 km in range of these radars (Ryzhkov 2007). OU-PRIME also suffered from this issue beyond ~85 km. This was accounted for by restricting the ranges within which the melting layer detection algorithm is performed, since it relies on the spatial distribution and vertical extent of polarimetric radar signatures.

One of CASA's strategies is to deploy a network of many small, low-cost radars for a distributive, collaborative, adaptive sensing (DCAS) of the atmosphere. CASA radars operate at a relatively low average transmitting power to achieve this goal, which produces a low signal to noise ratio (*SNR*) at ranges much farther than 20 km. ρ_{HV} is systematically lower for shorter wavelengths, klystron systems, and low *SNR* (below 20 dB at S-band according to Ryzhkov and Zrnic 1998b). CASA radars use magnetrons, but the shorter wavelength and lower signal strength cause ρ_{HV} to significantly decrease with range. This field was therefore corrected for noise using the bias-corrected Z_{DR} (in linear units as ζ_{DR} in (10)) and *SNR*. This equation required a correction on the second term since this text was last printed, according to (9).

(9) $\rho_{HV\text{-}NOISE} = \rho_{HV\text{-}QC} \left[1 + (1 / SNR)\right]^{-1/2} * \left[1 + (\zeta_{DR} / SNR)\right]^{-1/2}$

(Bringi and Chandrasekar 2001: Eq. 6.122 with correction)

(10) $\zeta_{DR} = 10.0 \exp (0.1 Z_{DR})$ (Bringi and Chandrasekar 2001: *Notations*)

Fig. 3.3 shows an example of the KSAO (Chickasha, OK) radar's uncorrected ρ_{HV}, corrected ρ_{HV}, radar reflectivity factor, and signal to noise ratio at 4.8° elevation angle during the 24 December 2009 blizzard. This image also illustrates CASA's targeted sector scanning strategy at every elevation angle except 1°. The CASA ρ_{HV} field was improved by these efforts, but was still well below 0.9 within meteorological echo where $Z_H > 15$ dBz beyond 25 km range

from the radar. This prompted use of *SNR* and range thresholds in the melting layer detection and hydrometeor classification algorithms to help discriminate where ρ_{HV} decreases from unity because of phase change as opposed to signal attenuation and/or nonuniform beam filling. Signal to noise ratio is actually quite high in the melting layer so *SNR* thresholds of 30 dB for CASA, 10 dB for OU-PRIME, and 25 dB for CHILL were used to classify wet snow. A 5 dB *SNR* and 5 dBz Z_H non-meteorological echo threshold was also employed for all algorithms.

3.3 Rayleigh scattering assumptions and attenuation

The radar equation for calculating reflectivity assumes all targets are oblate spheroids composed of liquid water, which is obviously not valid during winter storms. The variable density of ice between frozen (and perhaps rimed) hydrometeors is a major source of uncertainty for interpreting radar data. We specified physically realistic ice particle densities in the scattering simulations, but there is no way to know how representative these values are for every storm in every region (Zhang et al. 2011). Another related unknown is the dielectric factor, which is included in the radar backscattering cross section used to calculate every dual-polarized radar variable. We specified the dielectric factor in the T-matrix and Mueller-matrix models according to the actual hydrometeor composition (ice, water, or an air/ice/water mixture), but a single value is assumed when the radar is scanning in real-time. The scattering simulations and radar observations agree quite well despite these uncertainties.

The maximum diameter of spherical, liquid hydrometeors that still satisfy Rayleigh scattering conditions decreases with decreasing wavelength: approximately 2.1 mm at X-band, 3.5 mm at C-band, and 7 mm at S-band (Gunn and East 1954). These thresholds should be relaxed for frozen particles due to their lower dielectric factor and bulk density compared to

liquid water. Both of these factors contribute to the radar backscattering cross section used to determine the critical diameter. Dendrites, plates, and aggregates of dendrites with diameters exceeding the Rayleigh scattering threshold certainly exist aloft during winter storms. However, after careful interrogation of over 50 hours of radar data, even the X-band datasets did not appear to exhibit patterns suggestive of significant attenuation or backscattering differential propagation phase (δ) errors that would greatly impact HCA performance.

The radar may interpret an ice particle as completely liquid if a water coating as thin as 10% of the melting ice particle's diameter develops (Aden and Kerker 1951). Furthermore, a thinner water coating is needed to produce this result for shorter wavelength radars. Non-zero δ in regions of melting snowflakes from X- and C-band observations confirm departure from the non-Rayleigh scattering regime. These areas must be interpreted with caution.

For similar reasons, differential attenuation also occurs within and beyond the melting layer for low radar elevation angles during periods of heavy stratiform precipitation. When the radar beam intersects the radar bright band at a shallow angle, it becomes nearly oriented along the major, horizontal axis of large, water-coated aggregates. This substantially decreases Z_H while producing negative Z_{DR} and noisy K_{DP} beyond the melting layer in a radial fashion that is non-meteorological and physically unrealistic. An example of these differential attenuation issues at C-band wavelength during a winter storm where sleet is occurring at the surface is shown in Fig. 3.4. Attenuation correction for large, wet snowflakes is an ongoing topic of research (León et al. 2011), since most algorithms were originally designed for convective, warm-season precipitation. Therefore, no attenuation correction was performed on these data except for the effect of gases on OU-PRIME observations. Finally, ground clutter contamination

in OU-PRIME data was not removed so it produces an erroneous wet snow classification that should be ignored.

3.4 Melting layer detection and hydrometeor classification algorithm development

3.4.1 Overview

The fuzzy-logic hydrometeor identification algorithm described in Dolan and Rutledge (2009) was adapted for winter precipitation types to include cold, stratiform rain, sleet, wet snow (indicative of the melting layer), dry aggregated snowflakes, dendrites, and plates. A variable weighting system was also designed to optimize the algorithm's decision-making process between certain precipitation types. This substantially increased the skill of the algorithm. As is typical for many HCAs, classification is performed on each pixel without knowledge of decisions made for nearby pixels or how the radar variables trend with height and time. To address these deficiencies, the nearest-neighbor approach, use of texture fields (Ryzhkov et al. 2005b), and 2-dimensional membership beta functions (Zrnic et al. 2001) have proven useful in other HCA studies. We did not explore these concepts here though. The reader should refer to Chandrasekar et al. (2011) for a more detailed review of radar-based hydrometeor classification algorithms.

This algorithm produces a score between zero and one for each possible hydrometeor type within each radar bin based on how well the suite of polarimetric radar (PR) observations falls within the membership beta function ranges (ranges of expected values) for a given precipitation category. The score is also affected by how heavily each PR variable is weighted in the decision process. The hydrometeor class with the highest score is considered the "dominant" hydrometeor type. The slope of the membership beta functions (MBF) can be specified for either

strict or relaxed conformity of the observations into a range of expected values. Sometimes it is beneficial to decrease the slope parameters in this way or widen the MBFs to produce an overlap between different hydrometeor categories. This can prevent data gaps where classification would have been rendered impossible. The X-band membership beta functions for each level of the hydrometeor classification algorithm are shown graphically in Figs. 3.5, 3.6, and 3.7. MBFs for C-band (Figs. 3.8, 3.9, and 3.10) and S-band (Figs. 3.11, 3.12, and 3.13) are approximately the same except for smaller magnitude ranges of K_{DP}. Slope parameters are provided in Tables 3.4, 3.5, and 3.6. The weighting system used for each PR variable during each classification step is illustrated in Figs. 3.14, 3.15, and 3.16. It is significant that this single weighting system worked well on all four radar platforms and at all three weather radar wavelengths (X-, C-, and S-band). The algorithm methodology is described first, and then the derivations of these membership beta functions and weighting functions are explained.

3.4.2 Hydrometeor classification algorithm methodology

Park et al. (2009) suggests that HCA performance can be optimized if individual algorithms are developed for each major precipitation regime. It may be unrealistic to design a single algorithm (one set of membership beta functions) to handle convective and stratiform precipitation in both the warm and cold season. Rather, multiple algorithms could be used and combined in a decision tree with some minor input from the user, atmospheric soundings, or numerical weather prediction (Schuur et al. 2012). Our study settled on a two- or four-step hydrometeor classification approach for each 10° azimuth sector within full volume scans or along a single azimuth for vertical cross section radar scans. In the interest of developing an algorithm that can be used operationally, it should be noted that performing multiple iterations of

hydrometeor classification did not significantly increase the time required to complete these steps on a radar volume scan. In fact, it was much more computationally expensive and time consuming to interpolate temperature from a sounding to the radar coordinate system in order to use it as a variable in the algorithm.

The use of multiple HCA steps was motivated by failed attempts to include all five hydrometeor types in the same decision process, even when temperature was the most heavily weighted variable in the algorithm. These errors occurred because the expected polarimetric variable ranges for rain and sleet nearly encompass the ranges for all other hydrometeors according to scattering simulations in Fig. 2.2. Light rain and dry aggregated snow, with moderate Z_H, near zero Z_{DR}, and low K_{DP}, are virtually indistinguishable without prior identification of the melting layer, which separates the two phenomena (Ryzhkov and Zrnic 1998b).

Assuming a winter precipitation regime to begin with, dry aggregated snowflakes, dendrites, plates, and wet snow are classified within the radar volume first. “Melting pixels” are counted if wet snow is classified between acceptable melting layer elevations (1-4 km) and at ranges that exclude clutter contamination nearest to the radar, beam broadening, and beam ascent with propagation (5-40 km only). Following methodology from Giangrande et al. (2008) and Boodoo et al. (2010), statistics are performed on the heights of all accepted melting layer pixels to determine the melting layer (ML) base (20^{th} percentile), median (50^{th} percentile), mean, and top (80^{th} percentile) height. These percentile values were tested by Boodoo et al. (2010) with a three-year climatology comparison between radar, wind profiler, and RUC data. The 80^{th} percentile height (ML top) was highly correlated with the 0°C wet-bulb temperature level. These

procedures could be further modified to detect variable melting layer heights as a function of range along a particular azimuth window.

A PPI radar scan from OU-PRIME through the bright band of a winter storm at 1545 UTC on 28 Jan 2010 in Fig. 3.17 shows the melting layer descending toward the west. The radar-derived statistics as a function of azimuth for this radar volume are compared to the sounding indicated 0°C height in Fig. 3.18. The sounding (Fig. 3.19) was taken at the same location as OU-PRIME and within an hour of the radar data used to compute these statistics. There is excellent agreement between each dataset. However, the radar offers this temperature information at higher spatiotemporal resolution for no additional cost, as opposed to acquiring and using special soundings or model simulations.

If a sufficient number of melting layer pixels (>1 00, Giangrande et al. 2008) were identified in the radar volume, a "warm" HCA is performed to classify either rain, sleet, or more melting snow below the melting layer median height. Recall that wet snow or semi-melted ice particles that survive their descent through the melting layer can promote a transition from freezing rain to sleet near the surface (Thériault et al. 2006). Since scattering simulations and HCA testing confirmed that sleet and rain cannot be distinguished without temperature information, the possibility of sleet is simply classified if $T < 0°C$ according to the most recent sounding.

The third HCA step is a reclassification of dry aggregated snowflakes, dendrites, or plates above the melting layer median height. The membership beta functions and weighting functions are slightly different for this iteration since proper ice crystal classification is now the priority, as opposed to wet snow classification. This second "cold" HCA, the warm HCA, and the wet snow pixels from the first cold HCA are combined in the final, fourth step. Because wet snow can be

spuriously classified aloft where ρ_{HV} is anomalously low, pixels are not considered representative of the melting layer in this final step if they are higher than 0.5 km above the ML top or if *SNR* is below some threshold value based on the particular radar. Alternatively, if a ML was not indentified in the first cold HCA, the second cold HCA can be used as the final algorithm result assuming the entire atmospheric column is below freezing. If a melting layer is not identified in a particular scan, the ML information from the previous time step can also be extended in time, if appropriate. Similarly, ML information from a particular sector can be applied to sectors where a ML could not be identified for non-meteorological reasons.

These HCA steps are shown graphically in Fig. 3.20 for the same PPI scan in Fig. 3.17. Fig. 3.20-a (FH) shows the first cold HCA, which is primarily used to identify the melting layer by the wet snow category (yellow). The warm HCA (FW) between sleet, rain, and wet snow is created in Fig. 3.20-b. Sleet is appropriately classified below 800 m ASL according to the depth of the T < 0°C layer indicated by the sounding in Fig. 3.19. Then the second cold HCA (FC) reclassifies dendrites, plates, and dry aggregated snow to better represent the upper levels of the storm, shown in Fig. 3.20-c. Dendrites are classified in the southwest quadrant of this scan where Z_{DR} and K_{DP} are enhanced, corresponding to heights where the temperature approaches -15°C according to the sounding. In fact, the hydrometeor classification algorithm usually shows dendrites at the optimum -15°C temperature level or colder and extending down into regions that are ~5-10°C warmer, which matches our theoretical understanding of these crystals (PK97). Aggregates are chosen as the dominant hydrometeor type where both Z_{DR} and K_{DP} are near zero. For the final version of the HCA (FN) in Fig. 3.20-d, the warm and second cold HCA results are used below and above the ML median height along with appropriate wet snow pixels from the first cold HCA. It is up to the user or perhaps some external information as to which

hydrometeor classification provides the best diagnosis for the given weather situation. For instance, one must take into account that insufficient melting within the temperature inversion could lead to snow at the surface even when a bright band occurs.

All single and dual-polarimetric hydrometeor classification algorithms to date have relied heavily on a sounding or model output temperature fields (Liu and Chandrasekar 2000, Zrnic et al. 2001, Ryzhkov et al. 2005, Park et al. 2009, Dolan and Rutledge 2009, Elmore et al. 2011, Schuur et al. 2012). However, Zrnic et al. (2001) confirmed that excluding temperature from a warm-season convective HCA exercise only slightly degraded the accuracy and smoothness of the algorithm results. Scattering simulations from Chapter 2 suggest that the dual-polarimetric signatures between different hydrometeor types are sufficiently robust and exclusive enough to classify these phenomena without the use of external temperature, except between pure rain, freezing rain, and sleet.

It is plausible that ice water content (*IWC*), ice mass, or ice fraction could be used to distinguish a vertically or horizontally oriented transition from rain/freezing rain to sleet within the radar domain. However, these derived quantities are not pursued in this study because their calculation depends on many assumptions that render it unreliable, especially during winter storms. For instance, knowledge of the "rain line" to relate Z_{DR} and Z_H during rain must be known prior to the calculation, K_{DP} must be very accurate, and the storm should cover a large area from which to calculate such bulk statistics (Cifelli et al. 2002, Carey and Rutledge 2000). However, winter storms have low echo tops, K_{DP} was less trustworthy near the ground (and ground clutter) where the sleet classification should occur, and the rain-snow relationship was unavailable for these cases. Vivekanandan et al. (1994) showed that ice scatterers are not only nonspherical, but are also of varying bulk density, and these conditions lead to large variability

in the Z_H-*IWC* relationship, up to 2 orders of magnitude. They suggest that the *IWC* calculation method should be refined by first identifying the ice particle habit and density to decide which particular power law relationship is more accurate. This provides motivation for the current study. *IWC* can also be calculated directly from K_{DP} and Z_{DR} if these variables are trustworthy (Ryzhkov et al. 1998).

3.4.3 Development of wet snow membership beta function

Wet snow can be identified by the radar bright band with low ρ_{HV}, high Z_H, and enhanced Z_{DR} according to Fig. 3.21 from Brandes and Ikeda (2004: Fig. 1). The microphysics of melting snowflakes leads to ρ_{HV} and Z_{DR} signatures being displaced slightly below the classic Z_H bright band, near the bottom of the ML (Ryzhkov and Zrnic 1998).

ρ_{HV} is considered the most reliable indicator of the melting layer because of its relation to hydrometeor diversity induced by phase change (Giangrande et al. 2008). This field can approach values as low as 0.50 when the melting/isothermal layer near 0°C is extensive enough to fill the entire radar beam. Otherwise, the melting layer signatures may be diluted by non-uniform beam filling (Ryhkov and Zrnic 1998b, Ryzhkov 2007).

Photographs provided by Fujiyoshi (1986) in Fig. 3.22 help explain the snowflake melting process and its interaction with electromagnetic radiation indicated in Fig. 3.21. Z_H begins to increases by 5-10 dBz just above the 0°C level because snowflakes become wetted in the first stage of melting (Fig. 3.22-a). This increases the particles' effective density and dielectric constant to that of water while their diameters remain very large (Zrnic et al. 1993, Vivekandandan et al. 1993, Ryzhkov and Zrnic 1998a). Meltwater drops migrate to the

concavities between crystals and branches initially (Knight 1979), and then accumulate on the tips of dendritic branches as melting proceeds.

The snowflakes become more jagged and the original crystalline structure becomes hardly discernable by stage 2 (Fig. 3.22-b). The melted diameters are largest in this stage because sticking promotes further aggregation (Barthazy et al. 1988). Zrnic et al. (1993) confirms that the largest particles are found 100-200 m below the Z_H maximum, or with the Z_{DR} maximum. Observations from Fujiyoshi (1986) also showed that rain drops and snowflakes in different stages of melting usually fall together. The presence of oblate raindrops, large snowflakes, and smaller, nearly melted particles in the same radar gate contribute to reduced ρ_{HV} at this level.

In the third stage of melting (Fig. 3.22-c), the snowflakes start to collapse and thin, so that by stage 4 (Fig. 3.22-d) they are smooth, without holes, but still irregularly shaped. These particles are denser, have liquid water content > 50%, and have much smaller melted diameters (< 3 mm) so their fall speed drastically increases. Rapidly decreasing number concentration from size sorting between melted and semi-melted particles dictates that the Z_H enhancement terminates abruptly with decreasing altitude, even more so than it began aloft (Giangrande et al. 2008).

At stage 5 (no photograph) the original snowflake is completely indistinguishable and is more lens-shaped than spherical. This oblateness factor helps explain why other PR variables decrease much more rapidly than Z_{DR} below the bright band, as seen in Fig. 3.21. C-band OUPRIME observations during stratiform winter precipitation in Fig. 3.23 also show this lingering Z_{DR} enhancement just below the melting layer but above the relatively homogeneous values in the rain region.

Dolan et al. (2012) simulated the polarimetric radar variables expected for melting snow with a dual-layer electromagnetic scattering T-matrix and Mueller-matrix model. These ranges were used as a first guess for developing the wet snow membership beta function. Then PR variable ranges were optimized, weighted, and extended to be more mutually exclusive from plates, dendrites, and dry aggregated snow as well as representative of the noise encountered within the ML for various radars. Non-Rayleigh scattering due to large, melting aggregated snowflakes in the melting layer can produce extreme or erroneous values of K_{DP}, so this variable was excluded from the wet snow HCA altogether with a weighting factor of zero. Z_{DR} can also fluctuate wildly in the ML for similar reasons, so its variable range was widened between -2 to 8 dB. This range included negative values to accommodate differential attenuation above the ML, but this would ideally be accounted for by an attenuation correction algorithm. Since Z_H does not always exhibit a strong bright band signature, especially compared to ρ_{HV} and Z_{DR}, Z_H had the lowest weighting in the wet snow decision process and its variable range was widened extensively from 5-45 dBz (Straka et al. 2000).

3.4.4 Adaptation of remaining membership beta functions from scattering simulations

With the exception of wet snow, the membership beta functions were derived directly from the scattering simulation ranges in Chapter 2 and then adjusted to cover all realistic scenarios and make each category more mutually exclusive. For instance, since all dry aggregated snowflakes modeled by the T-matrix and Mueller-matrix were oblate with a single density relationship based on diameter, the minimum Z_H was manually extended to a more practical value of zero (Straka et al. 2000). The Z_{DR} range for aggregates was also widened to

include negative values (likely encountered due to noise and differential attenuation above the ML) and up to +1 dB. While most observations of dry aggregated snowflakes barely exceed 0.25 dB (Herzegh and Jameson 1992), 1 dB is an acceptable value for classification purposes considering the effect of noise, uncertainty, and the varying degree of aggregation (Bader et al. 1987, Illingworth et al. 1987, Straka et al. 2000).

Simulated K_{DP} for aggregates was extremely close to zero, but the upper bound for this membership beta function was raised based on the degree of noise in the K_{DP} calculation due to low correlation coefficient, low *SNR*, and strong gradients in differential phase on the fringes of precipitation echoes, within the melting layer, and around ground clutter (Wang and Chandrasekar 2008, Ryzhkov and Zrnic 1998b). This was a critical step toward increasing the algorithm's performance. K_{DP} values can be very small for longer wavelengths and the degree of uncertainty in its calculation, especially in and around the ML, must be taken into account by the HCA somehow. Previous hydrometeor classification algorithms have employed the use of confidence vectors for this reason (Park et al. 2009). Trial and error efforts to reduce dendrite over-classification of anomalously high K_{DP} regions just above the ML determined that the maximum acceptable aggregate K_{DP} range should be increased to 0.2° km^{-1} for X- and S-band CHILLL, 0.35° km^{-1} for OU-PRIME at C-band, and 0.5° km^{-1} for the CASA X-band radars. HCA performance in and around the melting layer was highly sensitive to these "confidence windows" for each radar platform/wavelength/resoultion. These values are still lower than the K_{DP} expected for dendrites or nearby wet aggregates in the melting layer. K_{DP} can reach 0.5 – 1° km^{-1} within the ML at S-band where backscattering differential phase (δ) remains near zero for particles with diameters less than ~10 mm (Zrnic et al. 1993a, Straka et al. 2000). If this algorithm were applied to another radar system, a 0.2-0.5° km^{-1} K_{DP} error range for the dry

aggregated snowflake category could be introduced based on the radar wavelength and spatial resolution. Otherwise, no additional modifications would be necessary.

The minimum Z_H for dendrites was lowered to zero while the Z_{DR} range associated with dendrites and plates was widened by at least 0.5 dB. Even after this initial relaxation of the MBFs, the dendrite category's lower Z_{DR} bound still needed to be extended down to 1.0 dB to meet the aggregate range. Otherwise, hydrometeors with Z_{DR} between 1.0 and 1.5 dB would have been unclassifiable. The dendrite category was modified as opposed to plates since Z_{DR} should be higher for latter hydrometeor.

3.4.5 ρ_{HV} membership beta functions

Scattering simulations were only performed for a homogenous collection of specific hydrometeor types without accounting for mixtures of particles or various stages of melting, so the modeled ρ_{HV} was always greater than ~0.99 (Balakrishnan and Zrnic 1990b). ρ_{HV} was manually allowed to range between 1.0-0.90 for all hydrometeors except wet snow, which encompassed 0.6-0.95 (Illingsworth and Caylor 1989, Ryzhkov and Zrnic 1998a, Straka et al. 2000). Trial and error revealed that the overlap between these categories was critical for satisfactory results.

Using mutually exclusive ρ_{HV} bounds for wet snow versus other categories about either 0.95 or 0.90 led to two major errors, respectively: 1) over-classification of wet snow at increasing range where ρ_{HV} decreased due to signal quality, and 2) over-classification of dendrites at the fringes of the melting layer where high Z_{DR} and moderately high ρ_{HV} dominated the HCA fuzzy-logic. Widening the MBF for wet snow as well as dry aggregated snowflakes to incorporate uncertainty, noise, and the displacement of PR signatures within the bright band also

helped mitigate this error without compromising the mesoscale variability of the ML signature found in the ρ_{HV} field.

3.4.6 Development of weighting functions

Hydrometeor classification was more successful when a variable weighting system was used for each level of the algorithm: cold HCA # 1 in Fig. 3.14 between wet snow, dry aggregated snowflakes, dendrites, and plates; warm HCA in Fig. 3.15 between wet snow, rain, and sleet; and cold HCA # 2 in Fig. 3.16 between dry aggregated snowflakes, dendrites, and plates. The algorithm was very sensitive to small changes in the distribution of weights, seemingly more so than to the variability in spatial resolution and data quality between each radar system. This was somewhat surprising given the vastly different radar characteristics described in Table 3.1, but encouraging of this algorithm's suitability for many radar platforms.

ρ_{HV} was weighted highest for wet snow detection. However, the more ρ_{HV} was weighted, the thinner the classified ML became since this polarimetric signature is usually strong and narrow in the vertical direction. Higher ρ_{HV} weighting also resulted in over-classification of dendrites at the fringes of the ML because Z_{DR} and Z_H were still high even though ρ_{HV} could have recovered toward unity.

K_{DP} and Z_{DR} have strong importance when differentiating oriented crystals and dry aggregated snowflakes. However, it was found that K_{DP} must be weighted slightly above Z_{DR} during crystal classification to keep the decision process mutual between these two variables. Otherwise, high Z_{DR} will dominate the HCA. For instance, Fig. 3.24 shows the HCA results within a dendritic growth zone where Z_{DR} and K_{DP} were competing. K_{DP} is enhanced from the dendritic growth zone down to the ML (2-4 km) but Z_{DR} is only strongly positive in an elevated region above 2.5 km. Dendrites are most likely growing where the Z_{DR} and K_{DP} signatures

maximize near 4 km (Kennedy and Rutledge 2011). Crystal aggregation occurs as these pristine crystals descend. The reflectivity-weighted Z_{DR} variable is more sensitive to diameter (by D^6) than the mass-weighted K_{DP} variable (by D^3). Therefore, Z_{DR} can become "diluted" by the presence of small, spherical targets or large, tumbling aggregates that overwhelm the particle size distribution with a low Z_{DR} value, even if large oriented crystals are also present. K_{DP} is only sensitive to oblate particles such that effectively spherical targets within the radar bin do not make any contribution to this variable. This explains why K_{DP} remains relatively high even when dendrites are aggregating because some large, oblate, pristine crystals are still present that can produce high values all the way down to the melting level.

These trends suggest that positive Z_{DR} only occurs when oriented crystals are pristine since this variable tends toward zero as aggregation begins, whereas enhanced K_{DP} can be indicative of *any* pristine dendrites remaining in the PSD. Therefore, K_{DP} was weighted highest in the snowflake and snow crystal categories.

Another case where K_{DP} and Z_{DR} compete for the snow type classification is when Z_{DR} > 2 dB (relatively high) but K_{DP} remains near zero (and *SNR* is still high enough to indicate a trustworthy scattering regime). These trends suggest plates could be present, but plates were seldom classified compared to dendrites. In fact, Fig. 3.25 shows the extent to which they were identified at all during these three case studies. This may be because plates occur less often, are simply not occurring in these case studies, or overlapping membership beta functions and radar constraints, such as increased elevation angle, prevent the natural ranges of Z_{DR} from approaching such high values needed to discriminate plates from dendrites.

This algorithm should be run on data during a time when plates were actually reported at the surface before the algorithm's ability to detect plates from dendrites is officially evaluated.

Recently, Williams et al. (2011) and others at the National Severe Storms Laboratory have shown that exceptionally high Z_{DR} in potential plate-crystal regions of winter storms appear in "cocoon" orientations at the tops of precipitating echoes, not in pockets contained within the cloud as for dendritic growth zones (Kennedy and Rutledge 2011). This physically suggests that plate classifications should not be collocated with that of dendrites because these crystal types might grow in different regions of the cloud, likely due to different temperature and saturation conditions.

Another hypothesis is that, before water saturation is reached, small crystals may grow as plates. Then once the humidity increases beyond water saturation and into ice supersaturated conditions, dendritic or sector branches would grow on top of, or superimposed on the edges of, crystals that previously looked like plates. This theory also suggests that plates and dendrites might not coexist in the same area because their growth habit depends on the environment. If the environment is suitable for plates, the radar should be able to identify them. We suggest that a ratio or 2-dimensional membership beta function (Zrnic et al. 2001) could be derived and used to exploit the inverse K_{DP}-Z_{DR} relationship between these two crystal categories in a future version of this hydrometeor classification algorithm.

Z_H has a low weight for all hydrometeor classifications because it is generally innocuous for all ice types without any significant trends with the differential measurements (Trapp et al. 2001). Temperature is the leading variable in the warm HCA but it has a 0.0 weight in both cold HCAs.

Testing proved that temperature was not necessary for the classification of hydrometeors above or within the melting layer because the signatures in ρ_{HV}, Z_{DR} and K_{DP} were sufficiently robust. Furthermore, inclusion of temperature tended to degrade the classification by producing

non-meteorological, horizontally oriented blocks of hydrometeor classification, as illustrated in Fig. 3.26 (from approximately the same time period and geographic region as Figs. 3.20, 3.24, and 3.25). First, the melting layer may have spatiotemporal variability that cannot be captured with a sounding. The radar and sounding indicated 0°C heights from these two sources might not agree either. Second, Fig. 3.26 also shows how the algorithm may use temperature to classify plates above dry aggregated snowflakes, and some dendrites farther above the plates. This is physically unrealistic since most snowflakes are made up of dendritic component crystals and plates have unfavorable geometry for coagulation. Third, dendritic and plate crystal growth are based on temperature *and* saturation. When the algorithm uses temperature as a variable, it produces a strict ice crystal classification that is horizontally oriented and may or may not coincide with dual-polarimetric signatures for oblate crystals. If plates or dendrites exist within the cloud, scattering results and obsevations suggest that they *will* produce enhanced K_{DP} and Z_{DR} signatures. The sounding-indicated -13 to -17°C region roughly corresponds to where oriented crystals should begin to grow, but the K_{DP} and/or Z_{DR} signatures may extend further toward the ML if dendritic crystals fall longer distances before they aggregate. This process is not represented in Fig. 3.26 because it is not allowed when temperature is driving the hydrometeor classification algorithm.

3.5 Summary

The success of the HCA algorithm depends on proper development of the weighting functions and adaptation of the membership beta functions from theory. Care must be taken to adjust these parameters such that the algorithm is not being tuned for a specific variable or situation. Rather, the radar algorithm's decision-making process should follow universal,

physical principles of winter storms. Realistic hydrometeor classifications also require precise dual-polarimetric radar observations. When this is not possible, noise and uncertainty can be taken into account by widening the ranges of expected values in the membership beta functions or relaxing the slope parameters.

K_{DP} has much greater magnitude ranges for shorter wavelengths and each radar system has different spatial resolution, transmitting power, quality of measurements, and calculation methods. Before these issues were dealt with by a tailored dry aggregated snowflake K_{DP} error/confidence window, the longer wavelength systems produced more erroneous hydrometeor classifications in and around the melting layer. This was because meteorological K_{DP} values were less exclusive from noise. Then trial and error revealed that a single weighting scheme worked equally well on all three radar systems at various wavelengths in both Oklahoma and Colorado. It was originally hypothesized that the X-band HCA would naturally be more trustworthy while the S-band algorithm might require fine-tuning for the same quality of results. However, these findings suggests that this algorithm could be run on data from any radar system once an appropriate dry aggregated snow K_{DP} confidence window is determined based on radar wavelength and spatial resolution. Chapter 4 illustrates how the X-band algorithm may be more reliable because of its dependence on K_{DP}, but the same methodology is still robust and applicable for X-, C-, and S-band wavelength systems during most continental winter precipitation regimes. The algorithm produced accurate results with low Z_H weighting and without temperature information, except for sleet classification. Further validation and analyses of winter storm microphysics with the HCA are presented in Chapter 4.

Table 3.1. Specifications of radars used in this study with the dual-polarimetric WSR-88D as a reference.

Name	**CSU-CHILL X**	**CASA**	**OU-PRIME**	**CSU-CHILL S**	**(KOUN) WSR-88D**
Wavelength	3.2 cm X-band	3.2 cm X-band	5.44 cm C-band	11.01 cm S-band	10.0 - 11.1 cm S-band
Frequency	9410 MHz	9410 MHz	5510 MHz	2725 MHz	2700-3000 MHz
Antenna Diameter	8.5 m	1.2 m	8.5 m	8.5 m	8.5 m
Height (ASL)	1432 m	350 m	342 m	1432 m	381 m
Nyquist Velocity	16 m s^{-1}	35 m s^{-1}	16.05 m s^{-1}	26 m s^{-1}	21-35 m s^{-1}
PRF	2000 s^{-1}	Dual 1600-2400 s^{-1}	1180 per s^{-1}	800 - 12000 s^{-1}	300-1300 s^{-1}
Pulse Width	650 ns	660 ns	800 (400 - 2000) ns	200-1600 ns	1600 - 4500 ns
Max Range	75 km	40 km	120 km	150 km	250 km
Peak Power	12 kW per channel	10 kW per channel	1000 kW	800 kW	750 kW
Transmitter	Magnetron	Magnetron	Magnetron	Klystron	Klystron
Beam Width	0.33°	1.8°	0.45°	1.1°	0.95°
Gain	56 dBi	36.5 dBi	50 dBi	43 dBi	44.5 dBi
Gate Spacing	75 m	100 m	125 m	150 m	250 m
Scanning Strategy	PPI, 4 RHIs, base	PPI	PPI, 2 RHIs, zenith	PPI, 4 RHIs, base	PPI
Update Time	5-10 min	3 min	7 min	10 min	5 min
Latitude	40.44625°	(Network center) 34.82764°	35.180299°	40.44625°	35.2361°
Longitude	-104.63708°	(Network center) -98.1006945°	-97.4355°	-104.63708°	-97.4633°

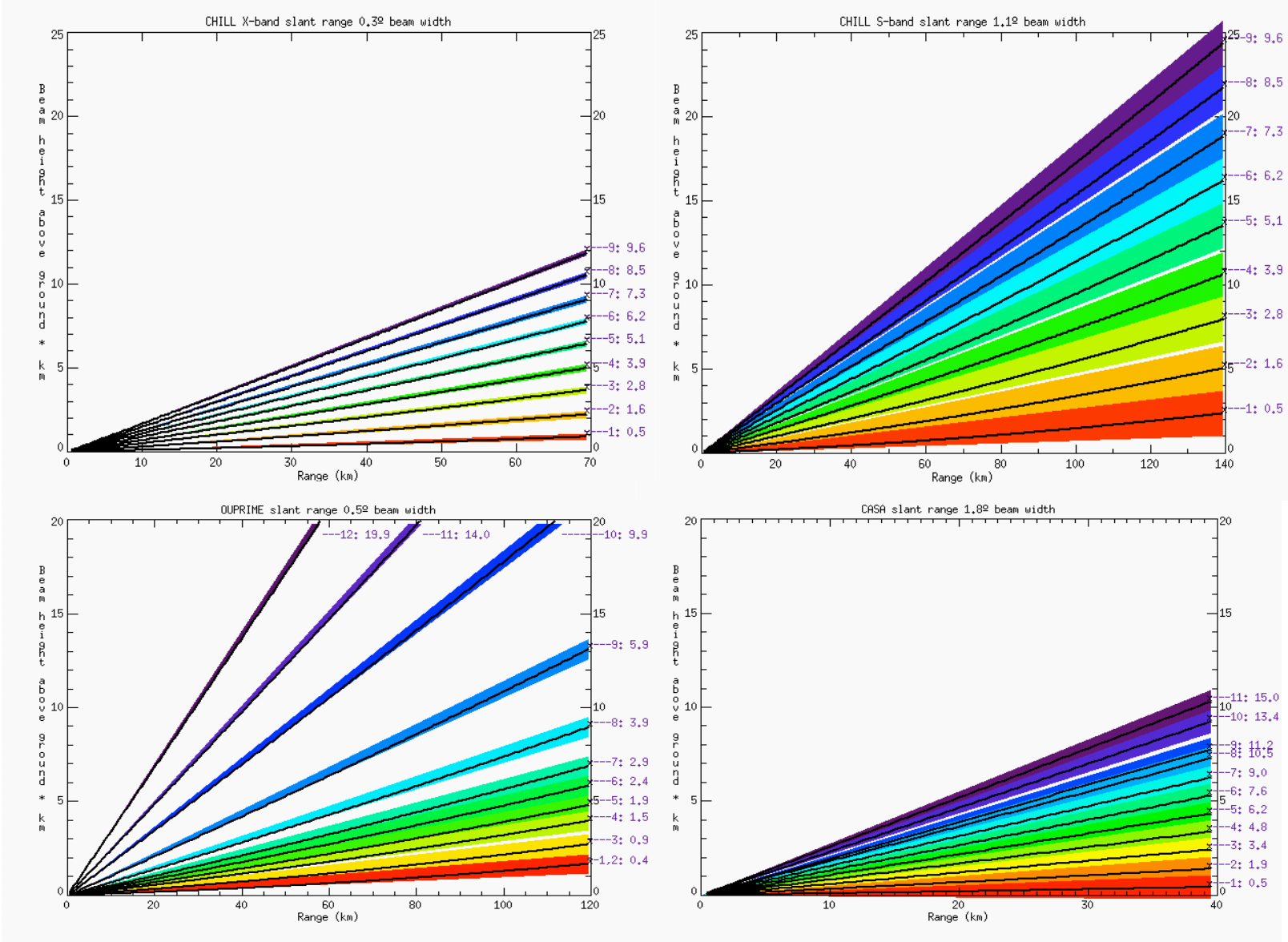

Fig. 3.1. Volume Coverage Patterns for X- and S-band CSU-CHILL, C-band OU-PRIME, and X-band CASA IP1 radars. Each ray's sweep number and elevation angle (°) are labeled according to the system's scanning strategy.

Table 3.2. Winter storms used to test hydrometeor classification algorithm (HCA).

Date	Location & Radars Used	Duration of precipitation studied	Time $T_{SFC} < 0°C$ at radars	Forcing Mechanisms for Precipitation	Precipitation Type Evolution
24 Dec 2009	Oklahoma OU-PRIME/CASA	0900 – 2359 UTC	1300 – 1400 UTC	Mid-latitude cyclone passage southeast of radars, low-level isentropic lift and advection of warm moist air from Gulf of Mexico toward Oklahoma, westward passage of transition zone precipitation band past radars as surface temperatures dropped below freezing, temperature inversion remained strong to the east of the transition zone, then the entire atmospheric column cooled over time, leading to blizzard conditions throughout the entire radar domain	Convective rain then westward passage of a precipitation band marking transition between rain/freezing rain/sleet to blizzard conditions
28 Jan 2010	Oklahoma OU-PRIME/CASA	1130 – 2359 UTC	1230 – 1245 UTC	Mid-latitude cyclone with stationary front south of radars, low-level isentropic lift and advection of warm moist air from Gulf of Mexico toward Oklahoma, weakening of temperature inversion and strengthening/deepening of surface cold layer over time	Stratiform rain leading to freezing rain and finally sleet
3 Feb 2012	Colorado CSU-CHILL X & S	0300 – 0700 UTC	Entire time period below 0°C	Upslope, easterly flow into Front Range Mountains, mid-latitude cyclone west of radar	Stratiform snow

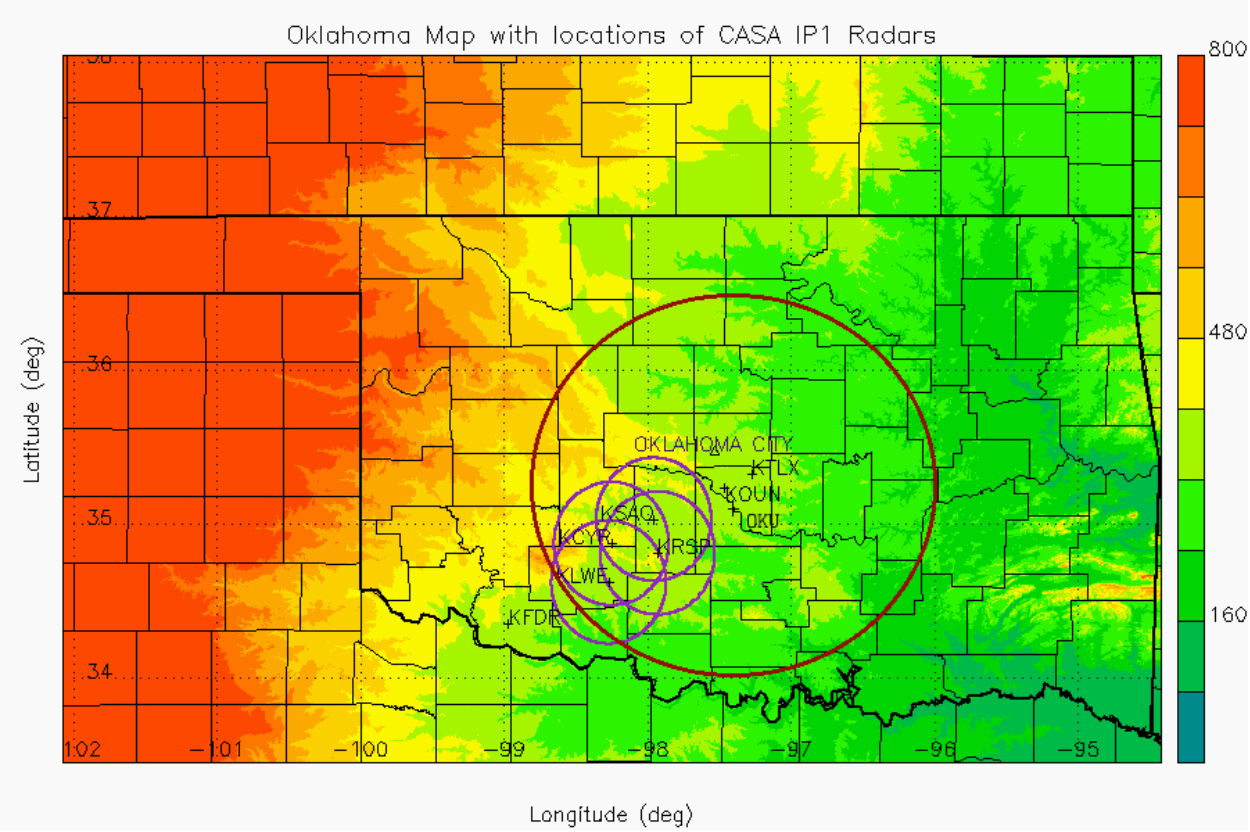

Fig. 3.2. Oklahoma topographical map (meters ASL) with purple 40-km range rings around four CASA X-band radars (KSAO, KRSP, KLWE, and KCYR described in Table 3.3) and maroon 120-km range ring around OU-PRIME C-band radar (OKU). Although not used in this study, KOUN is a nearby dual-polarimetric S-band radar while KTLX and KFDR are the closest National Weather Service S-band WSR-88D radars (adapted from Dolan and Rutledge 2010).

Table 3.3. Z_{DR} bias for each CASA radar operational during two Oklahoma winter storms

Name	**KSAO**	**KCYR**	**KRSP**
Location	Chickasaw, OK	Cyril, OK	Rush Springs, OK
Altitude (ASL)	375 m	460 m	442 m
Latitude	35.031390	34.87398	34.8128
Longitude	-97.956111	-98.25212	-97.93056
2009 Z_{DR} Bias (dB)	0.6	-0.3	-2.3
2010 Z_{DR} Bias (dB)	1.3	-1.6 before 1404 UTC -0.35 after 1404 UTC	-0.8

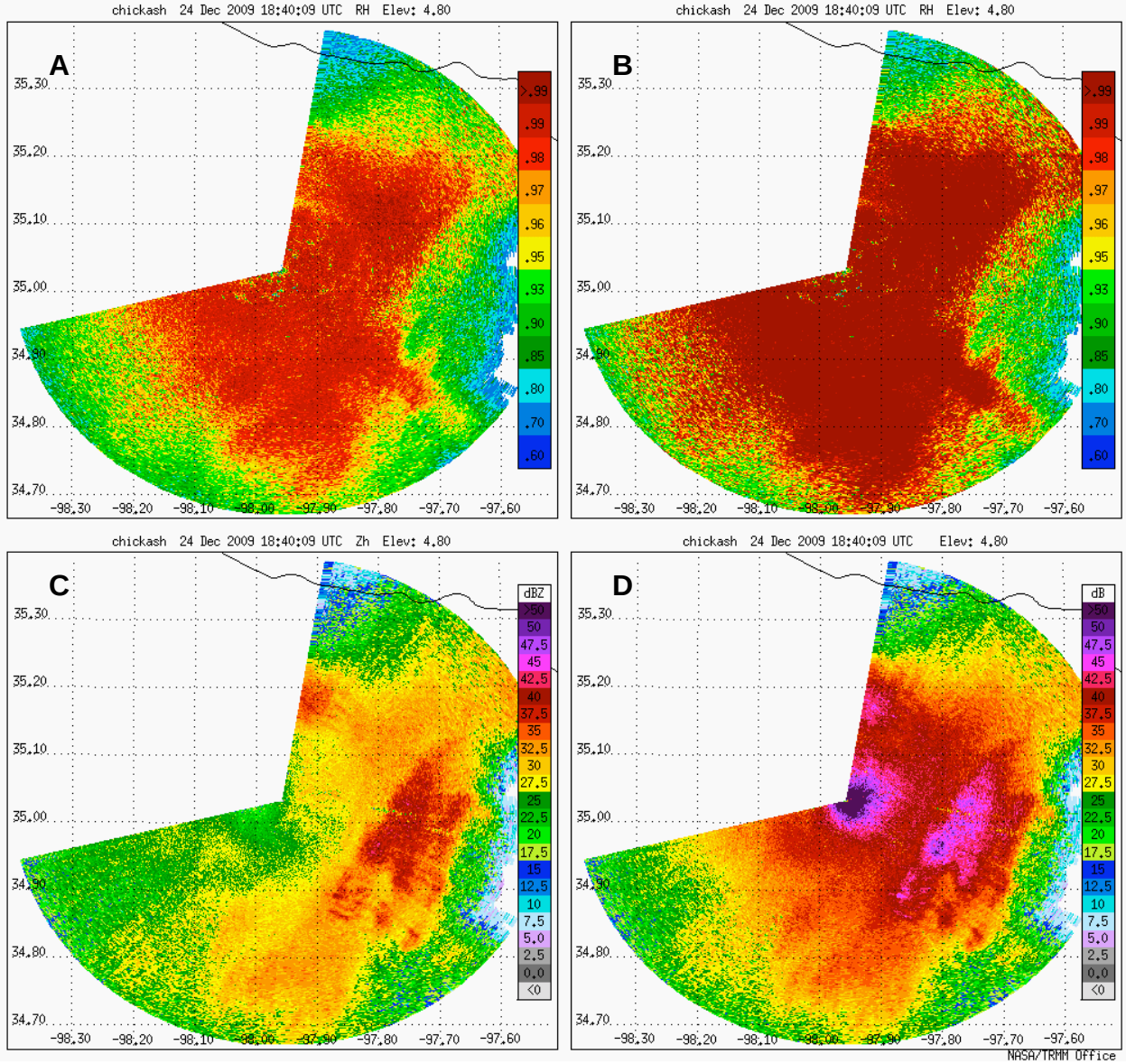

Fig. 3.3. Example of the original CASA ρ_{HV} field (a) and ρ_{HV} after being corrected for noise (b) for a given radar reflectivity factor Z_H (c) and signal to noise ratio (d).

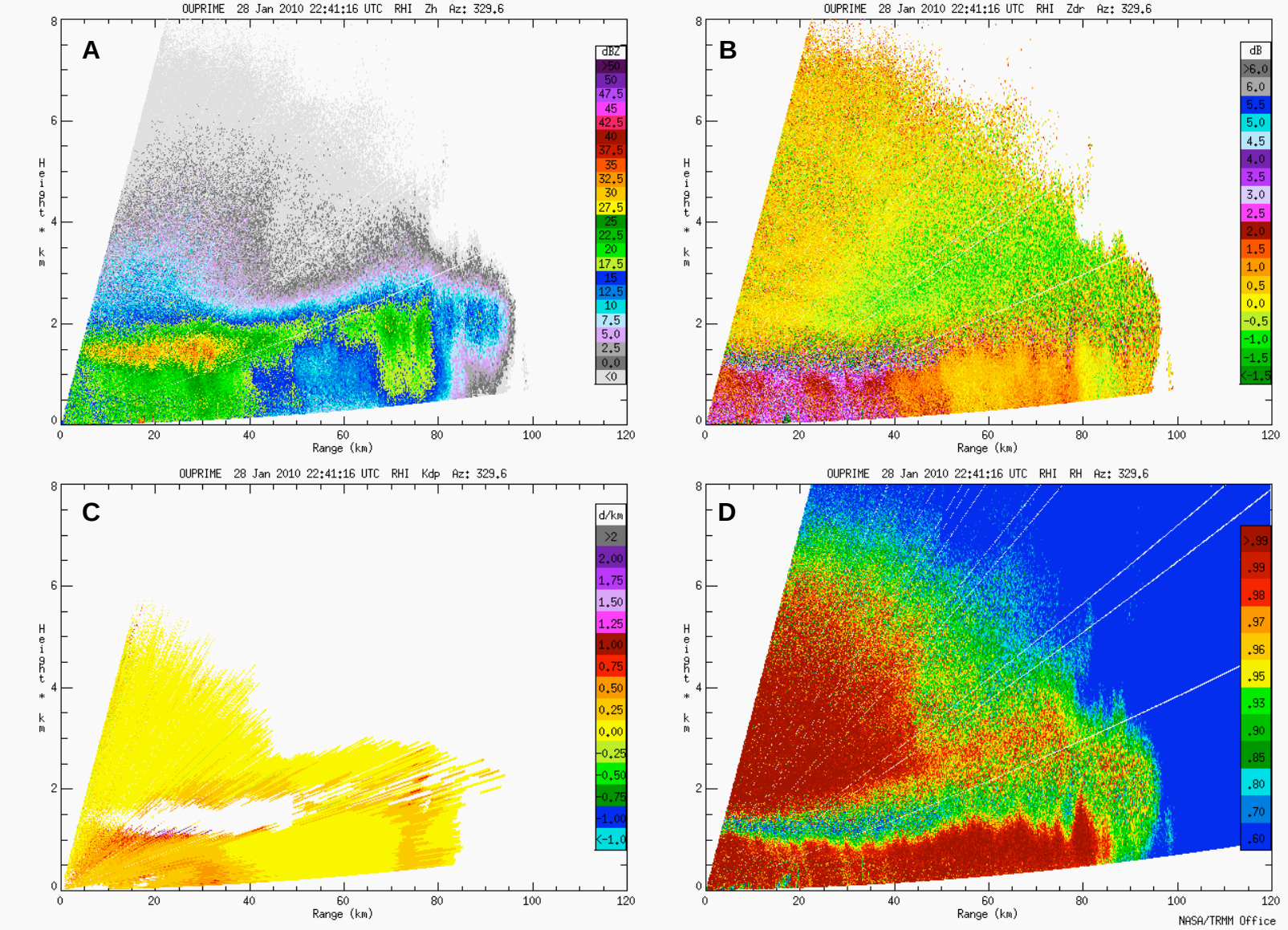

Fig. 3.4. OU-PRIME vertical cross section scan of (a) radar reflectivity: Z_H, (b) differential reflectivity: Z_{DR}, (c) specific differential phase: K_{DP}, and (d) correlation coefficient: ρ_{HV} showing differential attenuation through the melting layer of a winter storm.

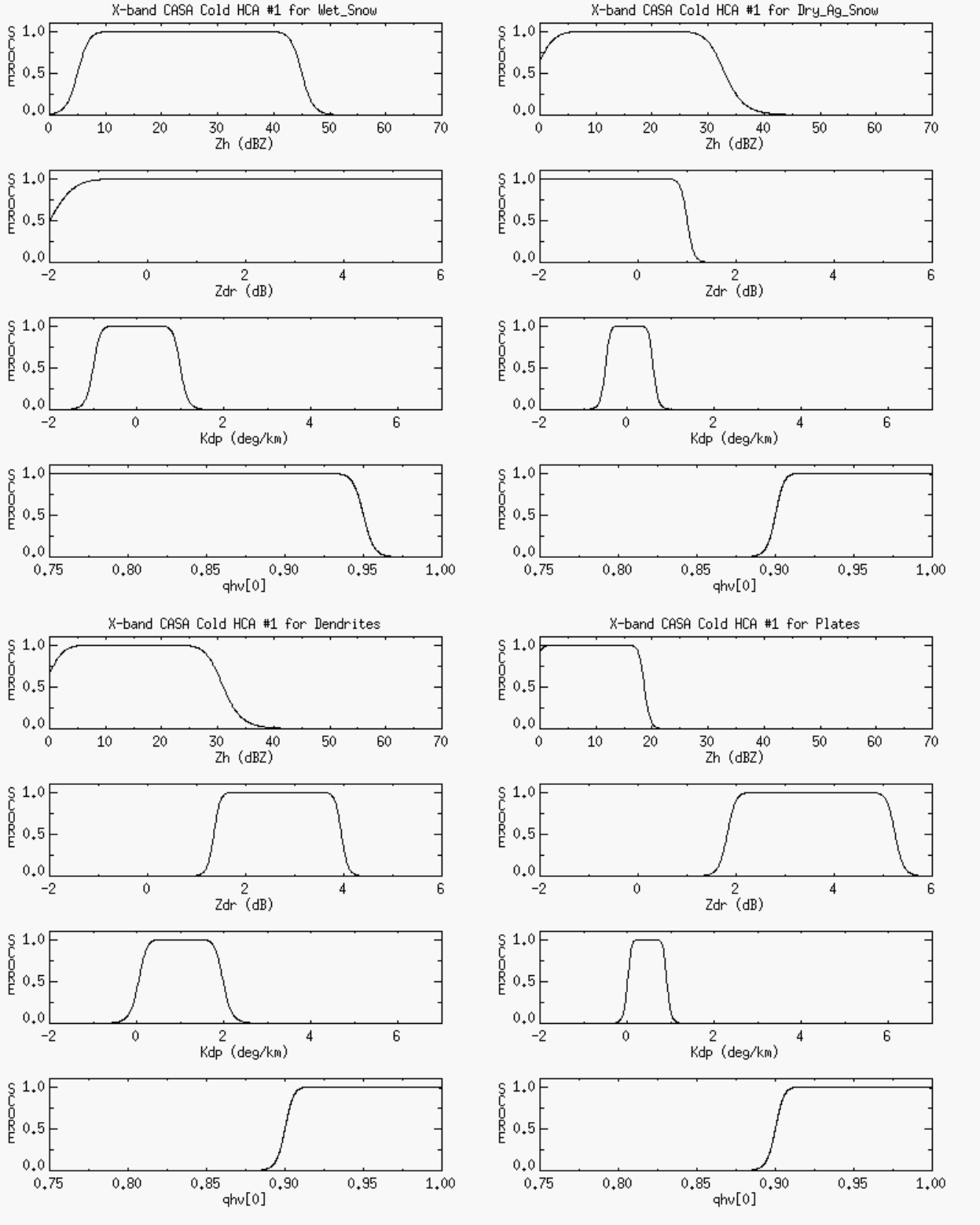

Fig. 3.5. X-band membership beta functions of radar reflectivity (Z_H), differential reflectivity (Z_{DR}), specific differential phase (K_{DP}), and correlation coefficient at lag zero (ρ_{HV}) for hydrometeors allowed above and within the melting layer: wet snow, dry aggregated snowflakes, dendrites, and plates (cold HCA #1).

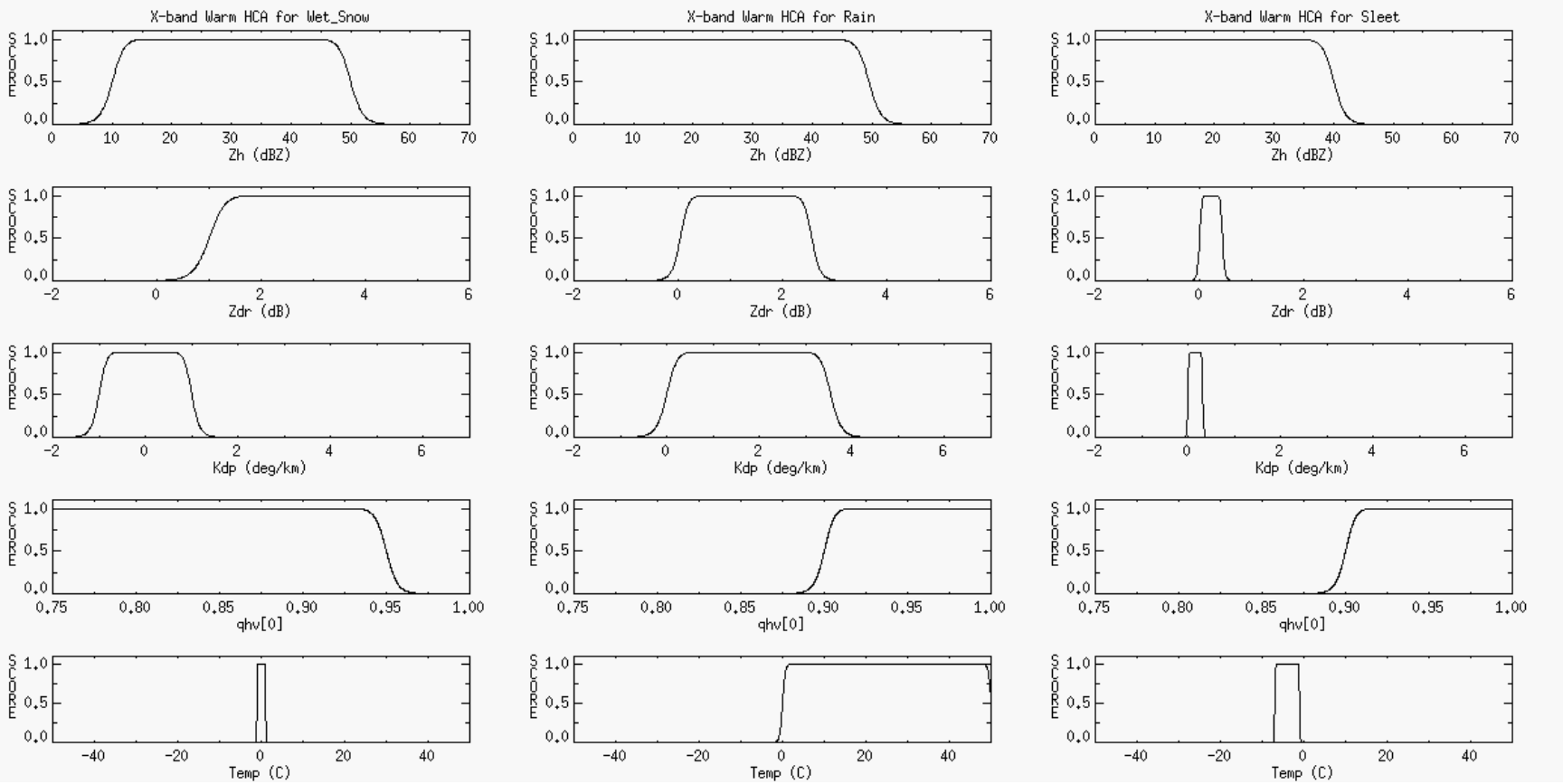

Fig. 3.6. X-band membership beta functions of radar reflectivity (Z_H), differential reflectivity (Z_{DR}), specific differential phase (K_{DP}), correlation coefficient at lag zero (ρ_{HV}), and temperature (Temp) for hydrometeors allowed below the melting layer: wet snow, rain, and sleet (warm HCA)

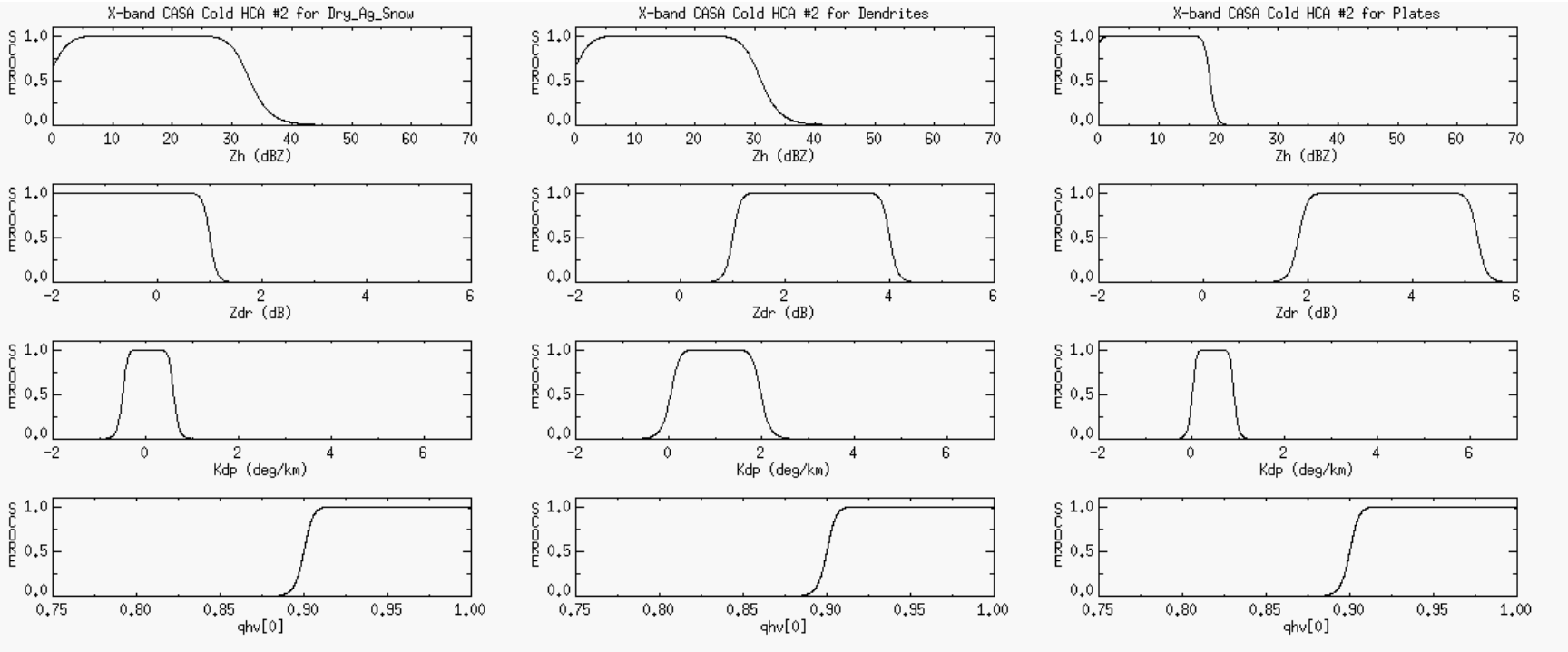

Fig. 3.7. X-band membership beta functions of radar reflectivity (Z_H), differential reflectivity (Z_{DR}), specific differential phase (K_{DP}), and correlation coefficient at lag zero (ρ_{HV}) for hydrometeors allowed above the melting layer: plates, dendrites, and dry aggregated snowflakes (cold HCA #2)

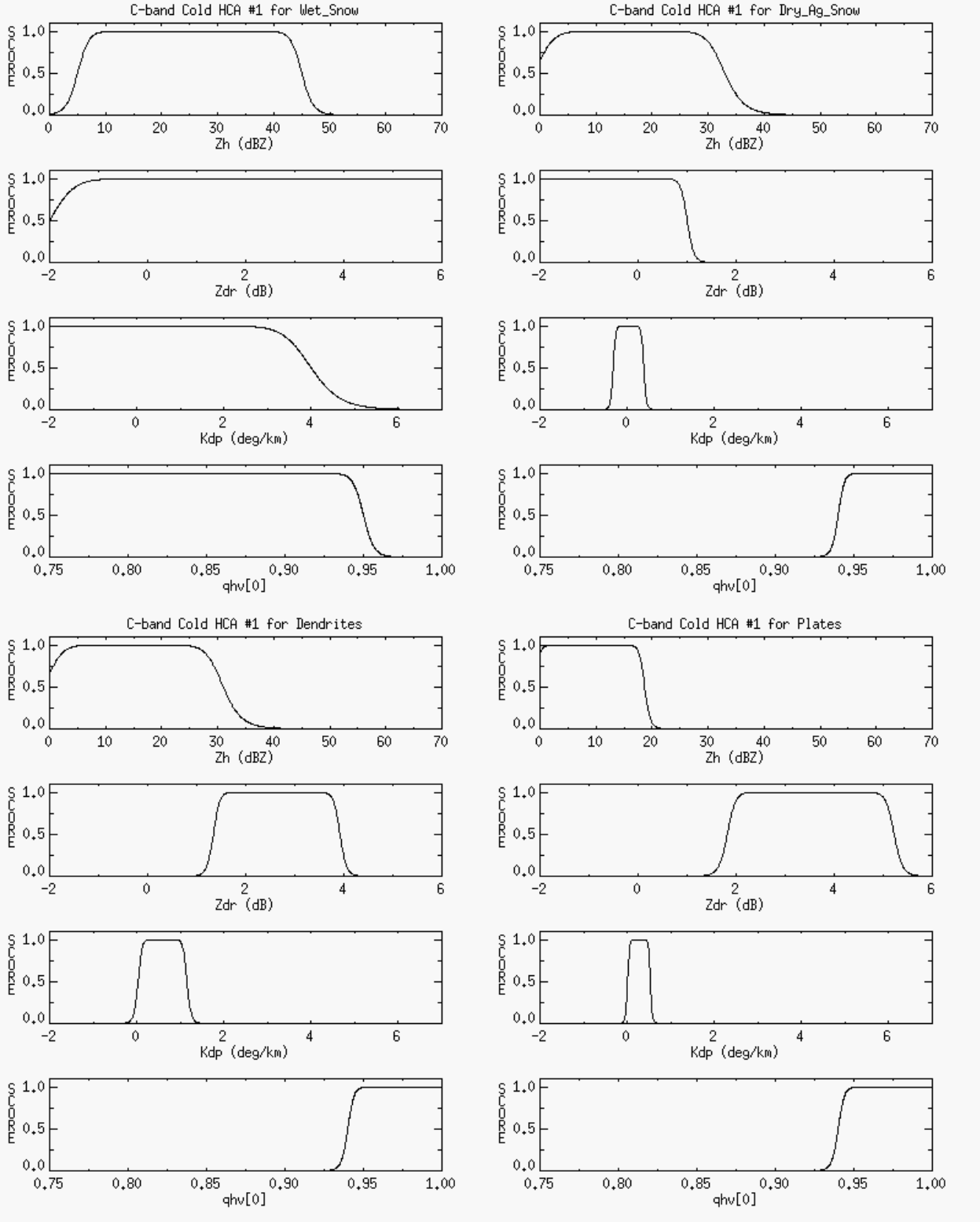

Fig. 3.8. C-band membership beta functions of radar reflectivity (Z_H), differential reflectivity (Z_{DR}), specific differential phase (K_{DP}), and correlation coefficient at lag zero (ρ_{HV}) for hydrometeors allowed above and within the melting layer: wet snow, dry aggregated snowflakes, dendrites, and plates (cold HCA #1).

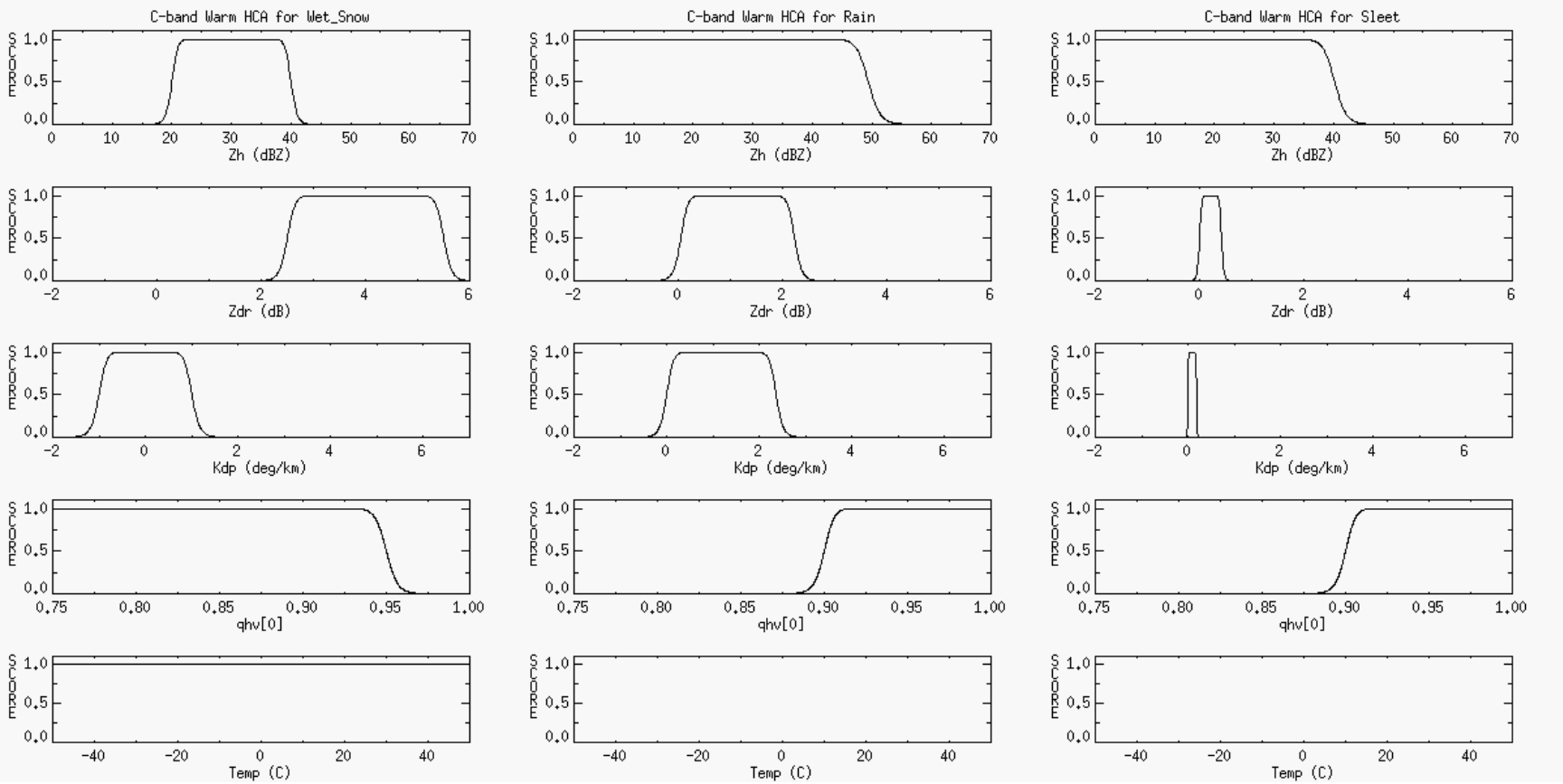

Fig. 3.9. C-band membership beta functions of radar reflectivity (Z_H), differential reflectivity (Z_{DR}), specific differential phase (K_{DP}), correlation coefficient at lag zero (ρ_{HV}), and temperature (Temp) for hydrometeors allowed below the melting layer: wet snow, rain, and sleet (warm HCA)

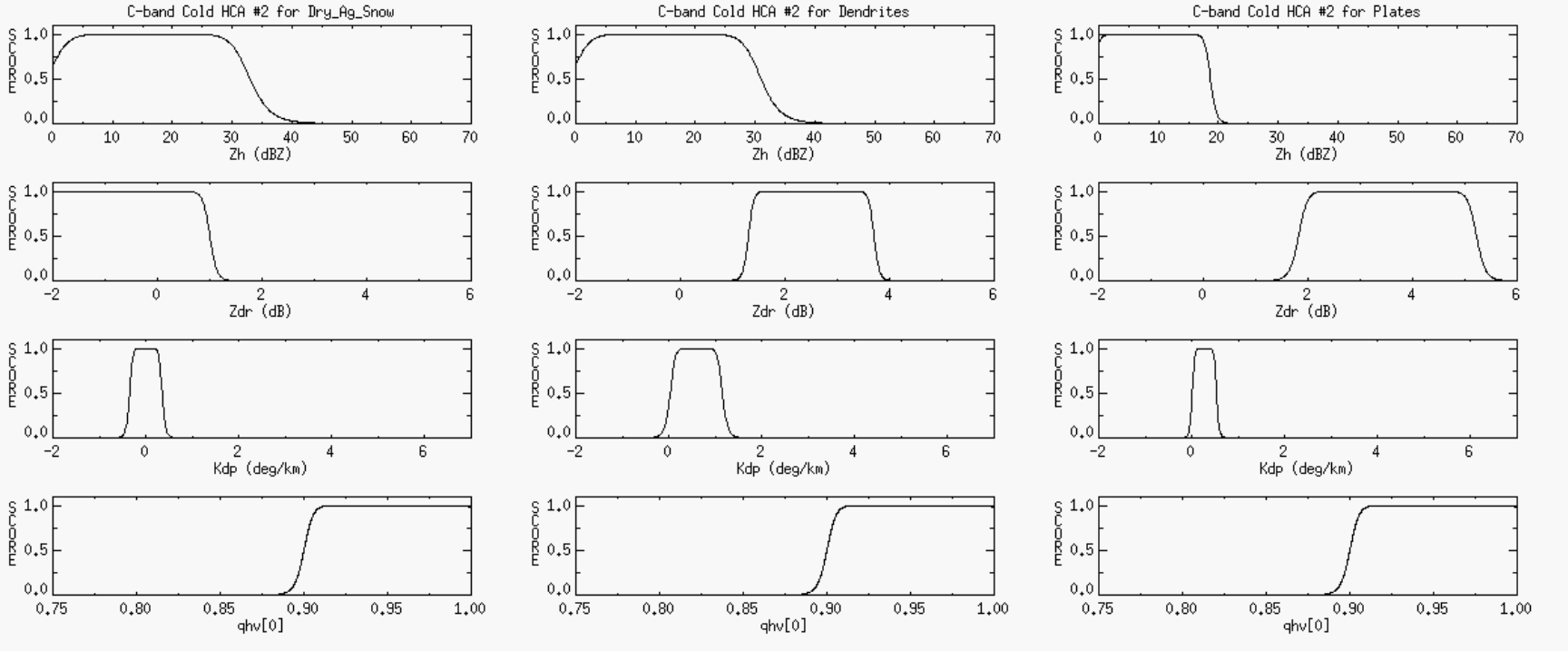

Fig. 3.10. C-band membership beta functions of radar reflectivity (Z_H), differential reflectivity (Z_{DR}), specific differential phase (K_{DP}), and correlation coefficient at lag zero (ρ_{HV}) for hydrometeors allowed above the melting layer: plates, dendrites, and dry aggregated snowflakes (cold HCA #2)

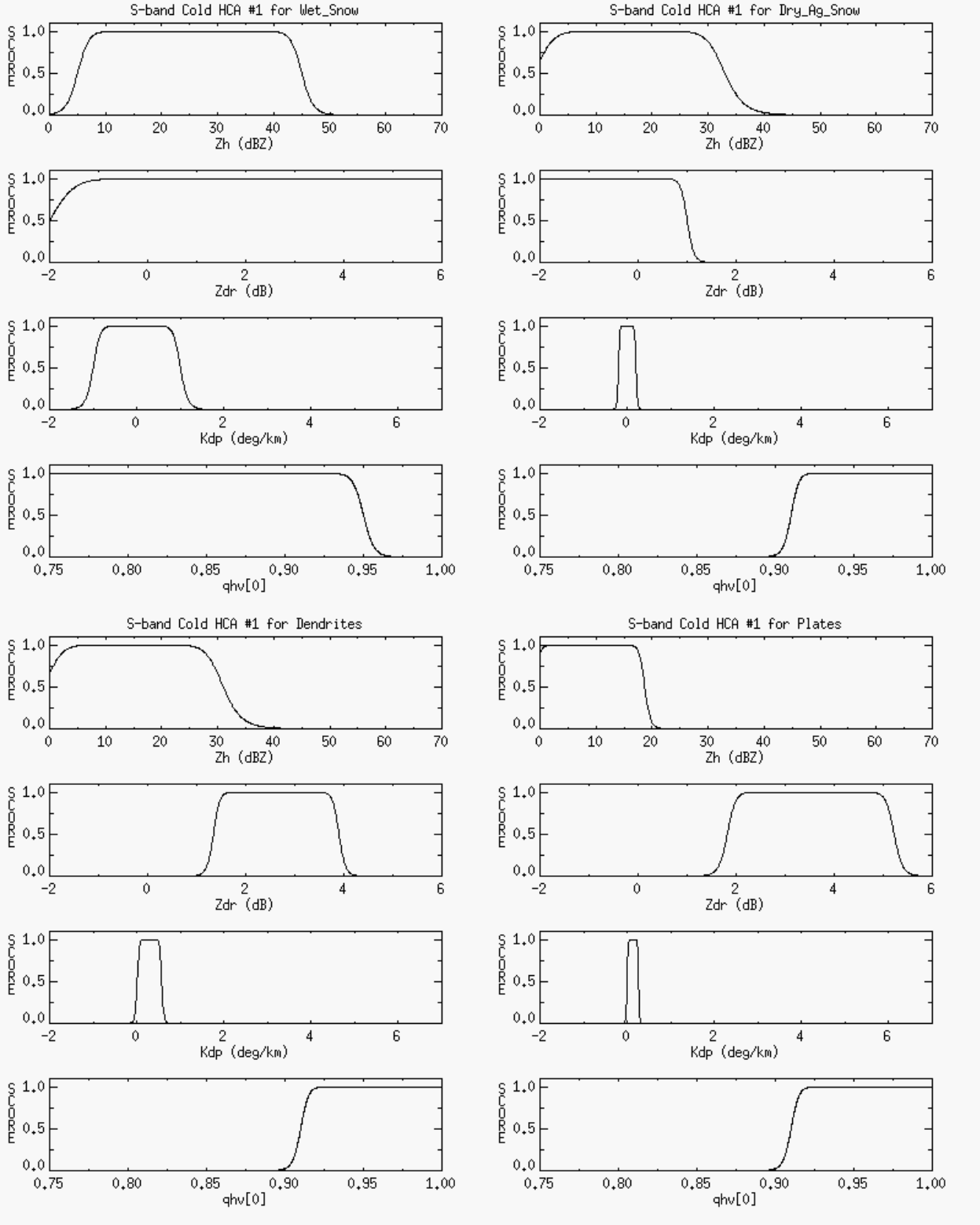

Fig. 3.11. S-band membership beta functions of radar reflectivity (Z_H), differential reflectivity (Z_{DR}), specific differential phase (K_{DP}), and correlation coefficient at lag zero (ρ_{HV}) for hydrometeors allowed above and within the melting layer: wet snow, dry aggregated snowflakes, dendrites, and plates (cold HCA #1).

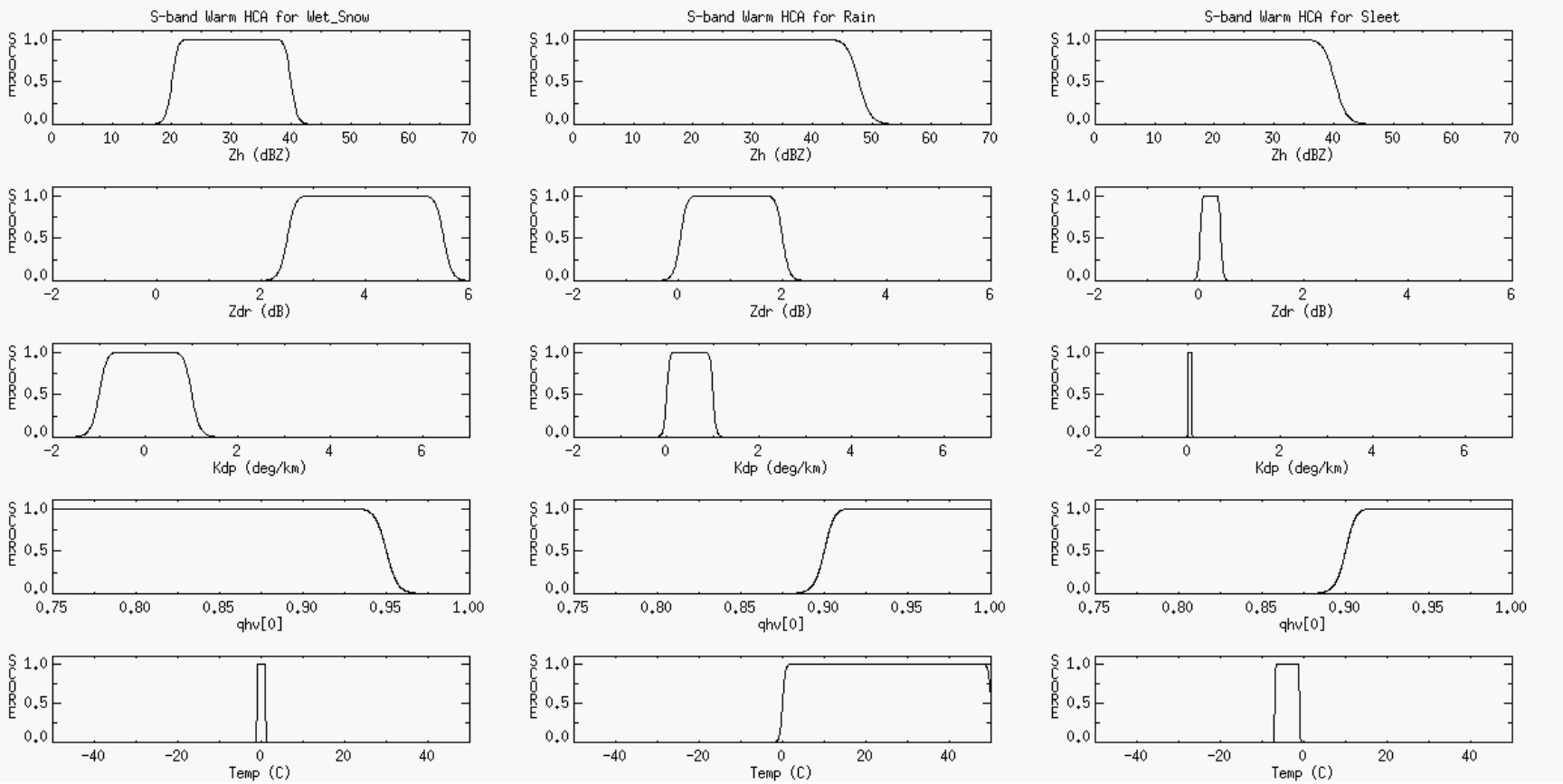

Fig. 3.12. S-band membership beta functions of radar reflectivity (Z_H), differential reflectivity (Z_{DR}), specific differential phase (K_{DP}), correlation coefficient at lag zero (ρ_{HV}), and temperature (Temp) for hydrometeors allowed below the melting layer: wet snow, rain, and sleet (warm HCA)

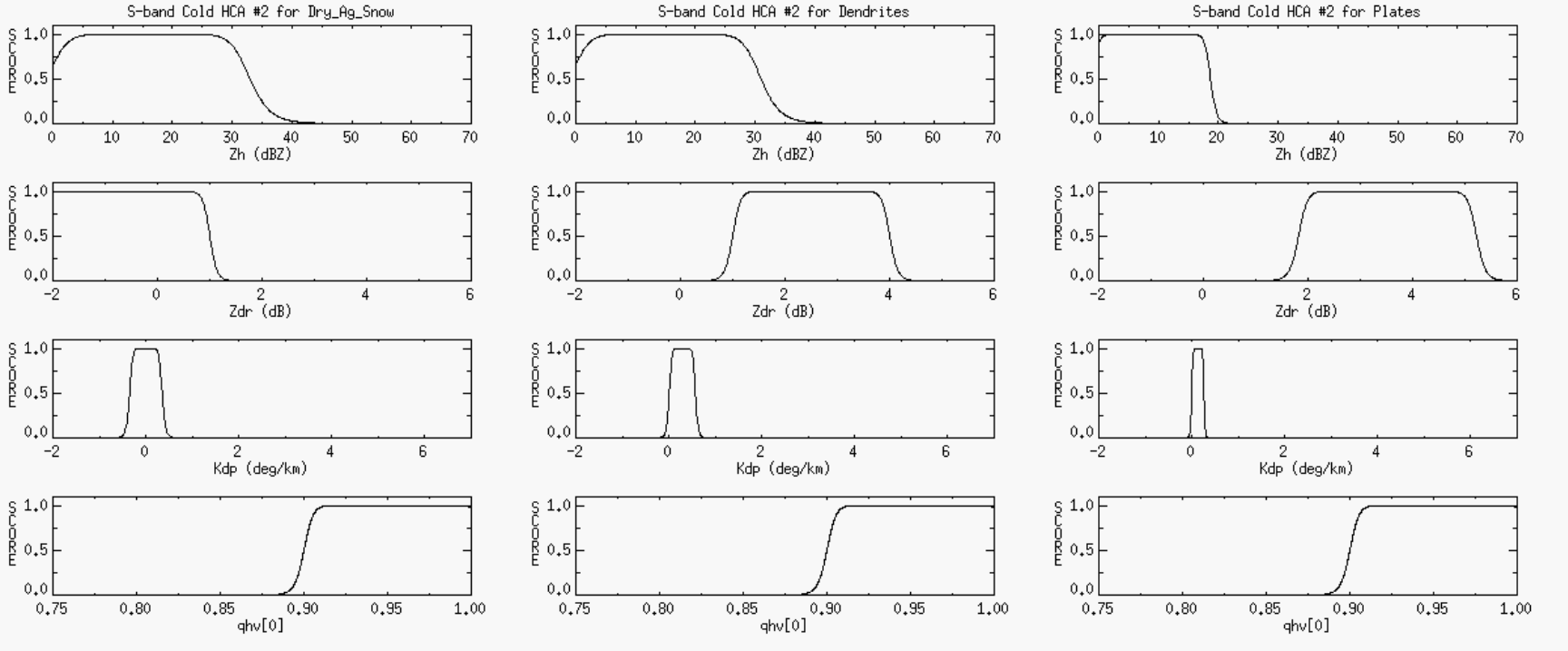

Fig. 3.13. S-band membership beta functions of radar reflectivity (Z_H), differential reflectivity (Z_{DR}), specific differential phase (K_{DP}), and correlation coefficient at lag zero (ρ_{HV}) for hydrometeors allowed above the melting layer: plates, dendrites, and dry aggregated snowflakes (cold HCA #2)

Table 3.4. Slope parameters for X-, C-, and S-band Cold HCA #1 membership beta functions between plates (PL), dendrites (DN), dry aggregated snowflakes (AG), and wet snow (WS).

Variable	PL	DN	AG	WS
Z_H	10	5	5	10
Z_{DR}	10	10	15	10
K_{DP}	5	5	5	5
ρ_{HV}	10	10	10	30

Table 3.5. Slope parameters for X-, C-, and S-band Warm HCA membership beta functions between wet snow (WS), sleet (SL), and rain (RN).

Variable	WS	SL	RN
Z_H	15	15	10
Z_{DR}	5	8	10
K_{DP}	8	8	6
ρ_{HV}	10	10	30
Temp	20	40	15

Table 3.6. Slope parameters for X-, C-, and S-band Cold HCA #2 membership beta functions between plates (PL), dendrites (DN), and dry aggregated snowflakes (AG).

Variable	PL	DN	AG
Z_H	10	5	5
Z_{DR}	10	10	15
K_{DP}	5	10	5
ρ_{HV}	10	10	10

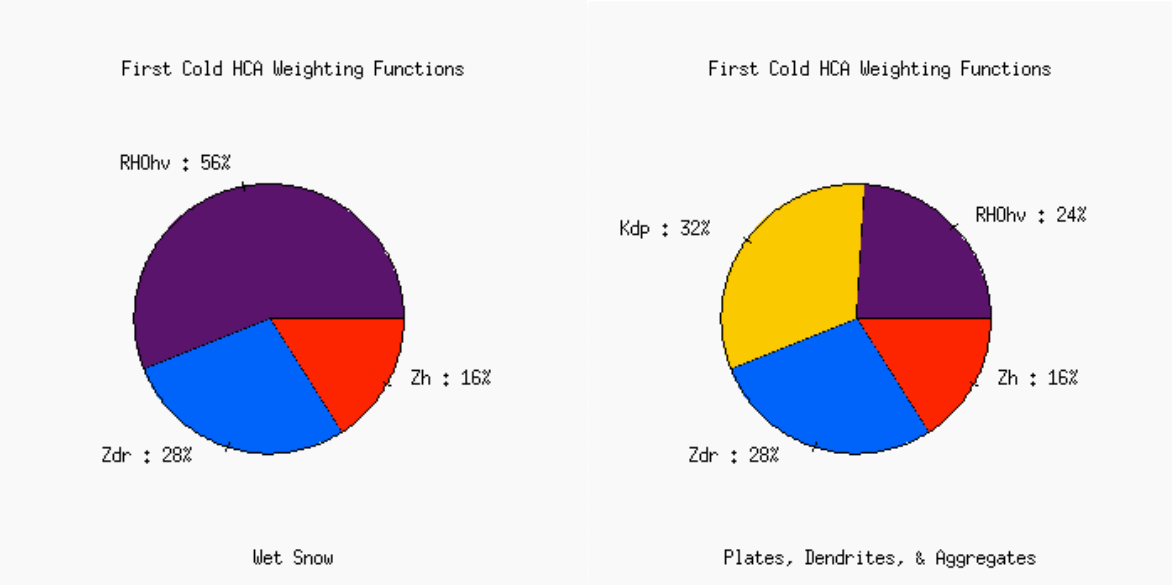

Fig. 3.14. Weighting functions for the X-, C-, and S-band first cold HCA between wet snow, dendritic crystals, plate crystals, and dry aggregated snowflakes. Percentage values show the relative weighting each variable receives in the hydrometeor classification algorithm score. Separate weighting distributions and variables were used to classify certain hydrometeors.

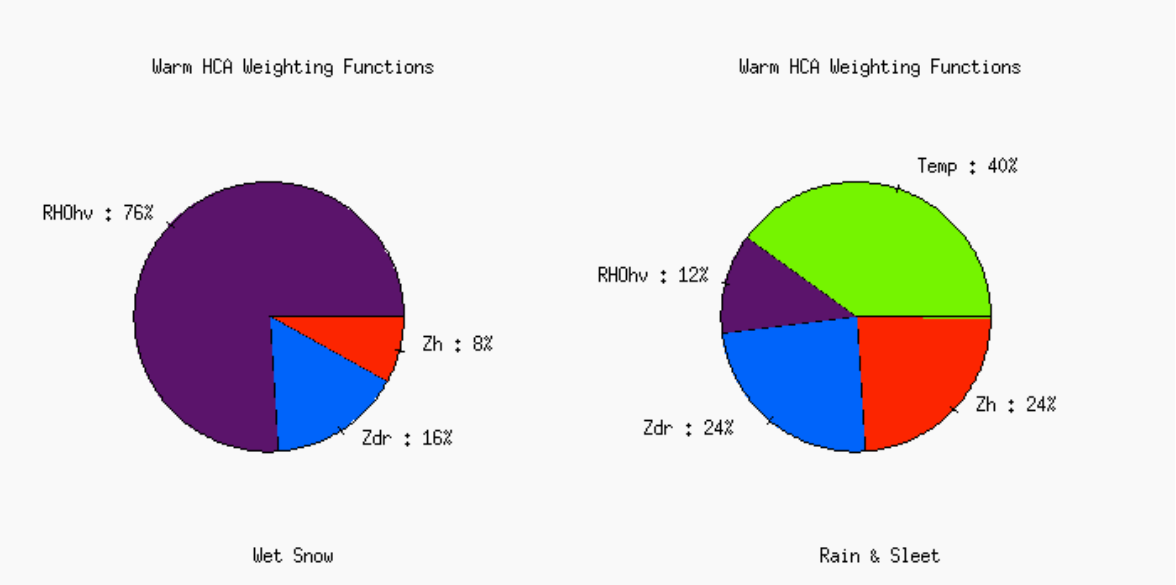

Fig. 3.15. Weighting functions for the X-, C-, and S-band Warm HCA between wet snow, rain, and sleet. Percentage values show the relative weighting each variable receives in the hydrometeor classification algorithm score. Separate weighting distributions and variables were used to classify certain hydrometeors.

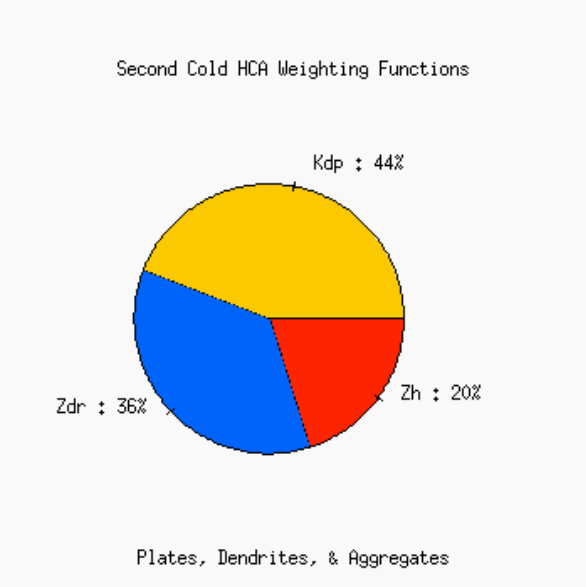

Fig. 3.16. Weighting functions for the X-, C-, and S-band second cold HCA between dendritic crystals, plate crystals, and dry aggregated snowflakes. Percentage values show the relative weighting each variable receives in the hydrometeor classification algorithm score.

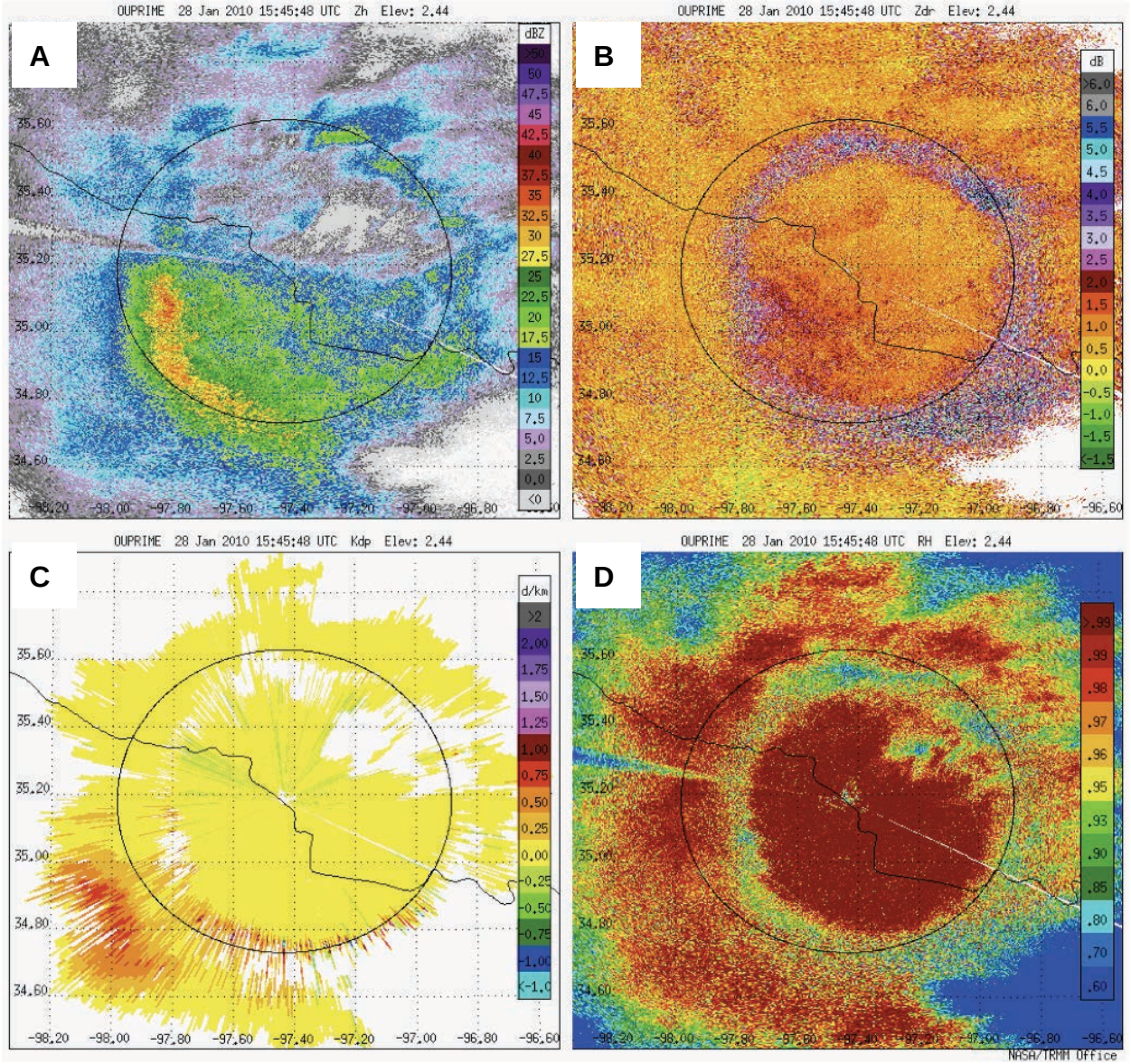

Fig. 3.17. (a) Z_H, (b) Z_{DR}, (c) K_{DP}, and (d) ρ_{HV} through the melting layer of stratiform winter precipitation along the 2.44° elevation angle.

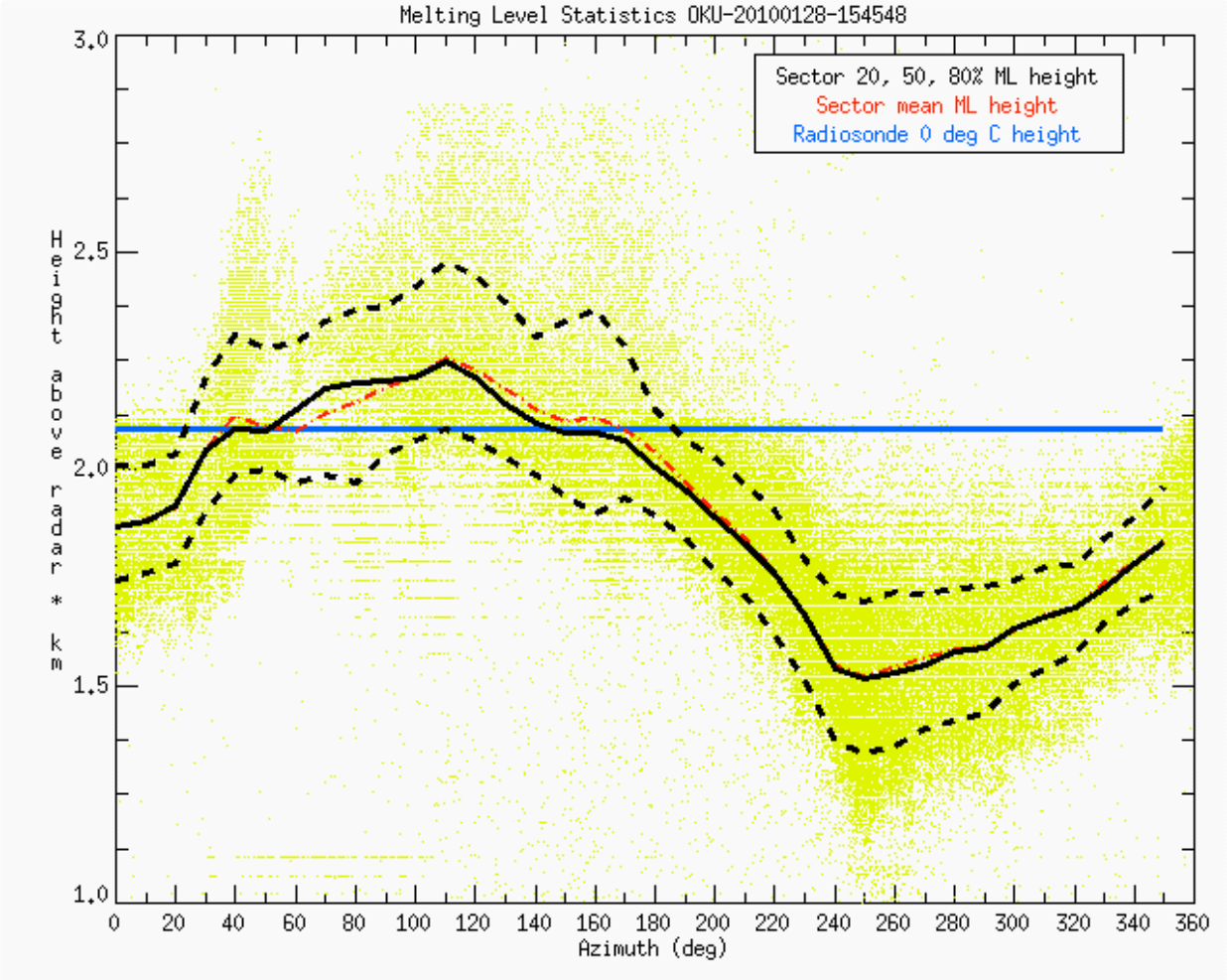

Fig. 3.18. Melting layer detection algorithm statistics for each 10° azimuth window based on the PPI scan in Fig. 3.16. All "melting pixels" are indicated in yellow with the 20th, 50th, and 80th percentile heights in black. The solid black line is the median melting layer height. The dashed red line is the mean melting layer height. The 0°C level according to the KOUN 15 UTC sounding (Fig. 3.18) from approximately the same location is shown in blue.

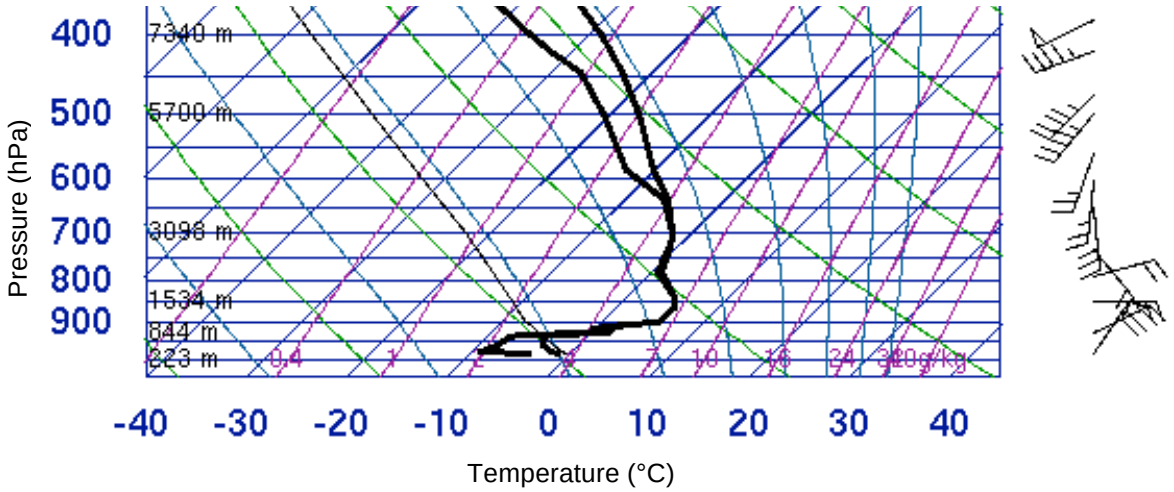

Fig. 3.19. 28 January 2010 15 UTC sounding at KOUN in Norman, OK (Univ. of Wyoming).

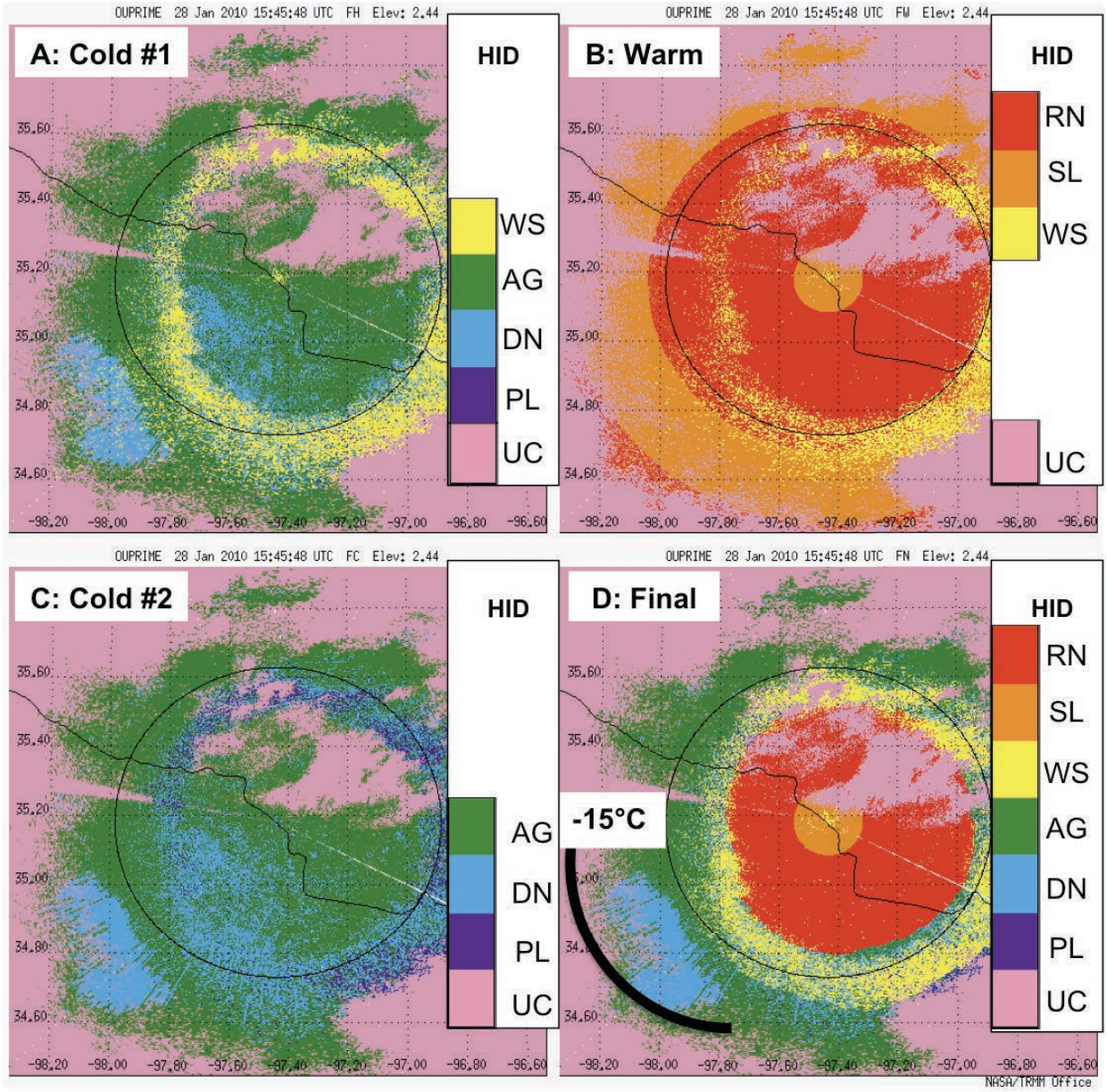

Fig. 3.20. (a) First cold HCA, (b) warm HCA, (c) second cold HCA, and (d) final combined HCA between plates (PL-purple), dendrites (DN-blue), dry aggregated snowflakes (AG-green), wet snow (WS-yellow), sleet (SL-orange), and rain (RN-red) for the same PPI sweep in Fig. 3.16 (HID = hydrometeor ID, UC = unclassified/clear air/non-meteorological echo). -15°C isotherm shown from 15 UTC sounding in Fig. 3.19.

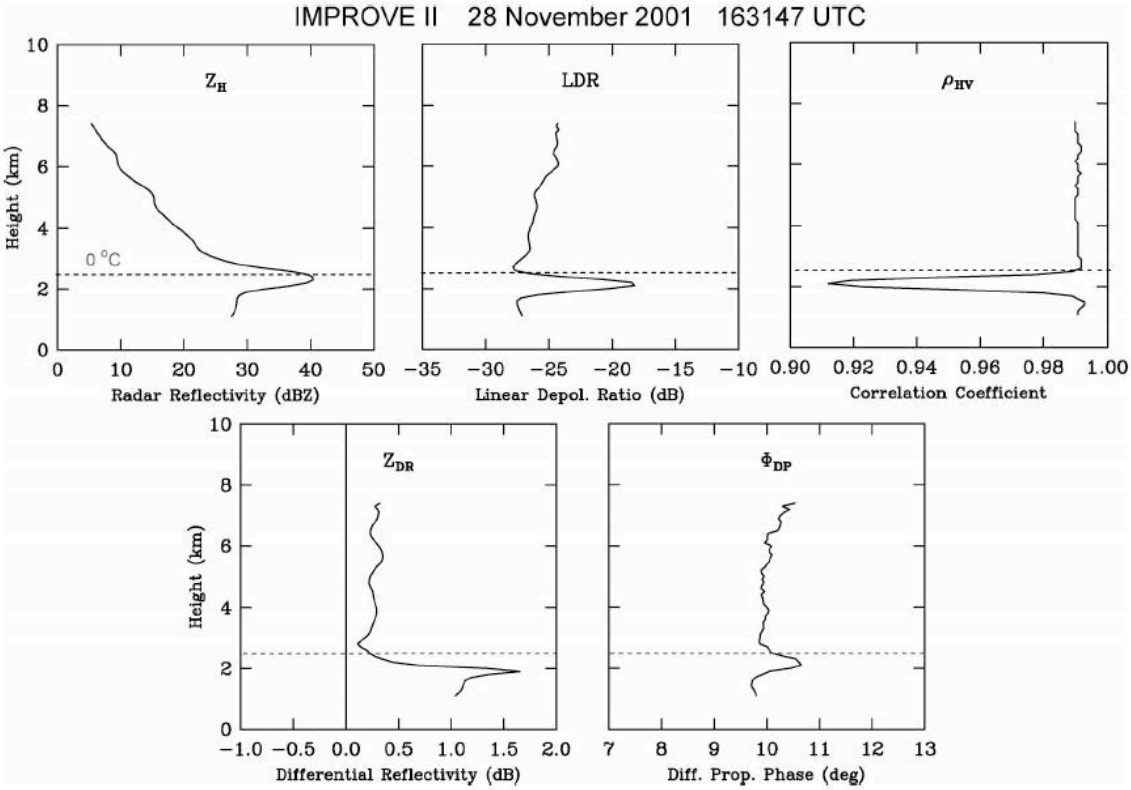

FIG. 1. Profiles of polarimetric measurements (Z_H, LDR, ρ_{HV}, Z_{DR}, and Φ_{DP}). The estimated 0°C level (2.47 km) is shown by a horizontal line. Heights are above mean sea level.

Fig. 3.21. from Brandes and Ikeda (2004).

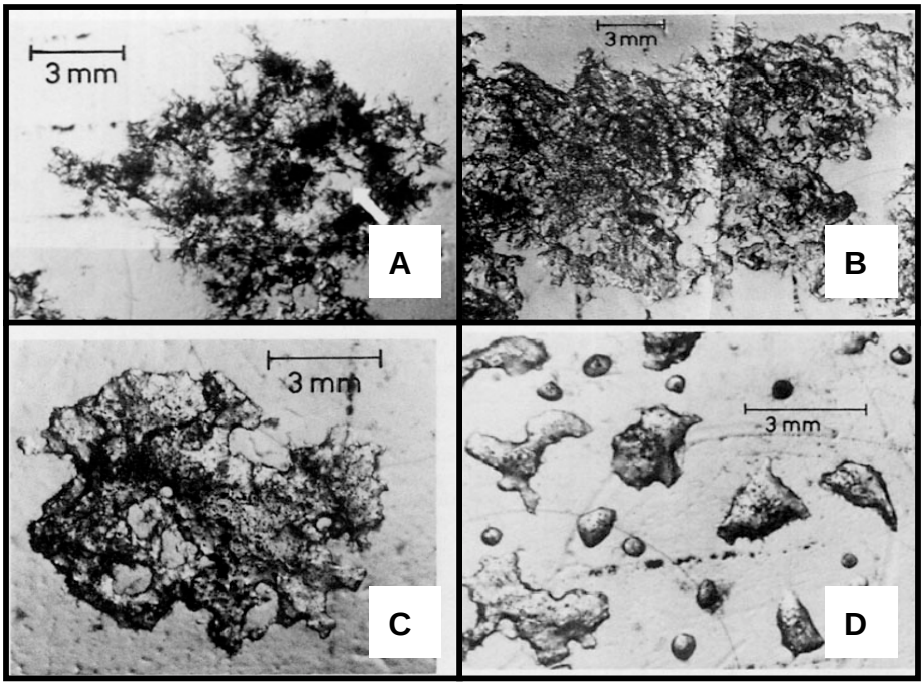

Fig. 3.22. Photographs of snowflakes during stages one (a), two (b), three (c), and four (d) of melting from Fujiyoshi (1986).

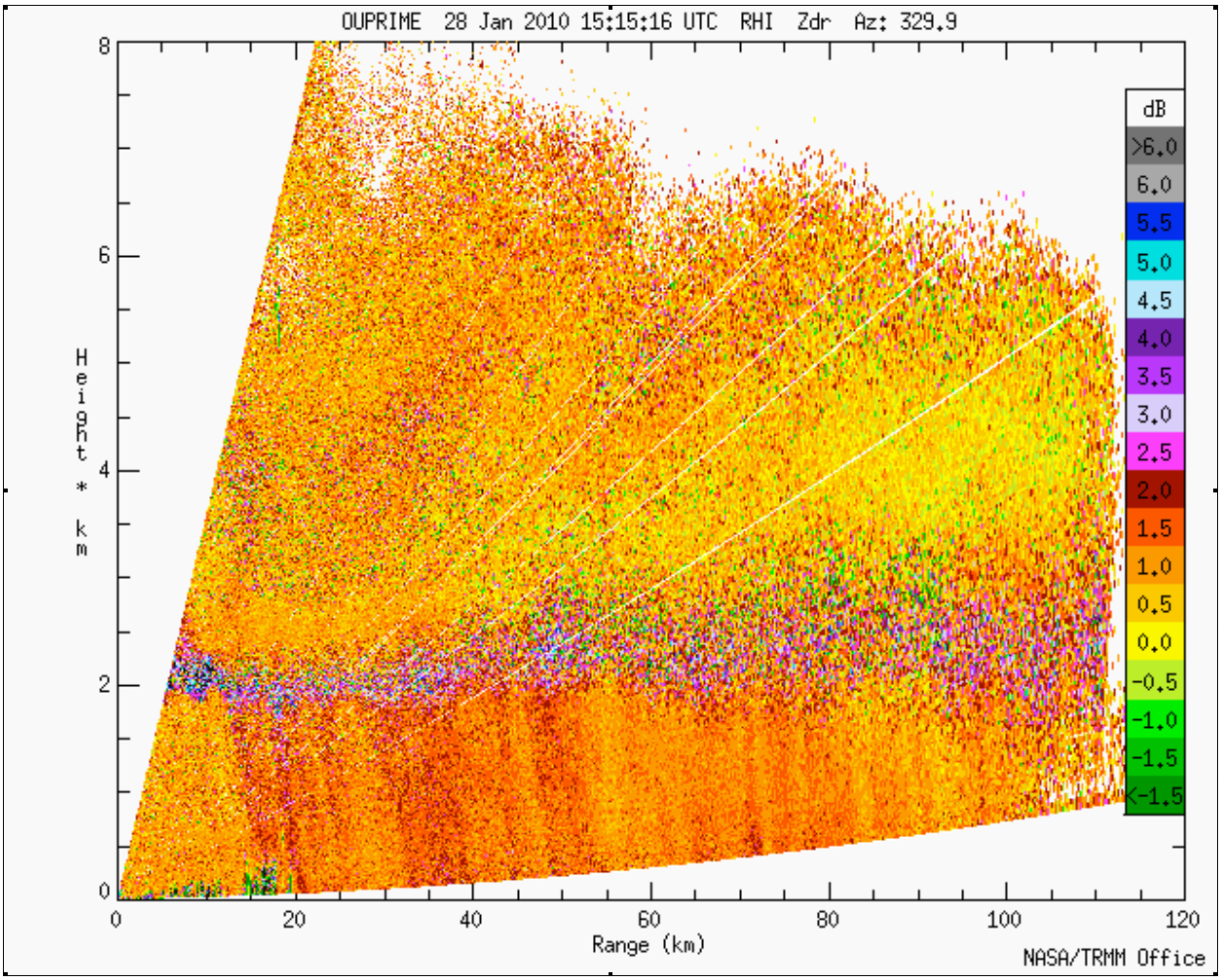

Fig. 3.23. Vertical cross section scan of differential reflectivity Z_{DR} during stratiform precipitation.

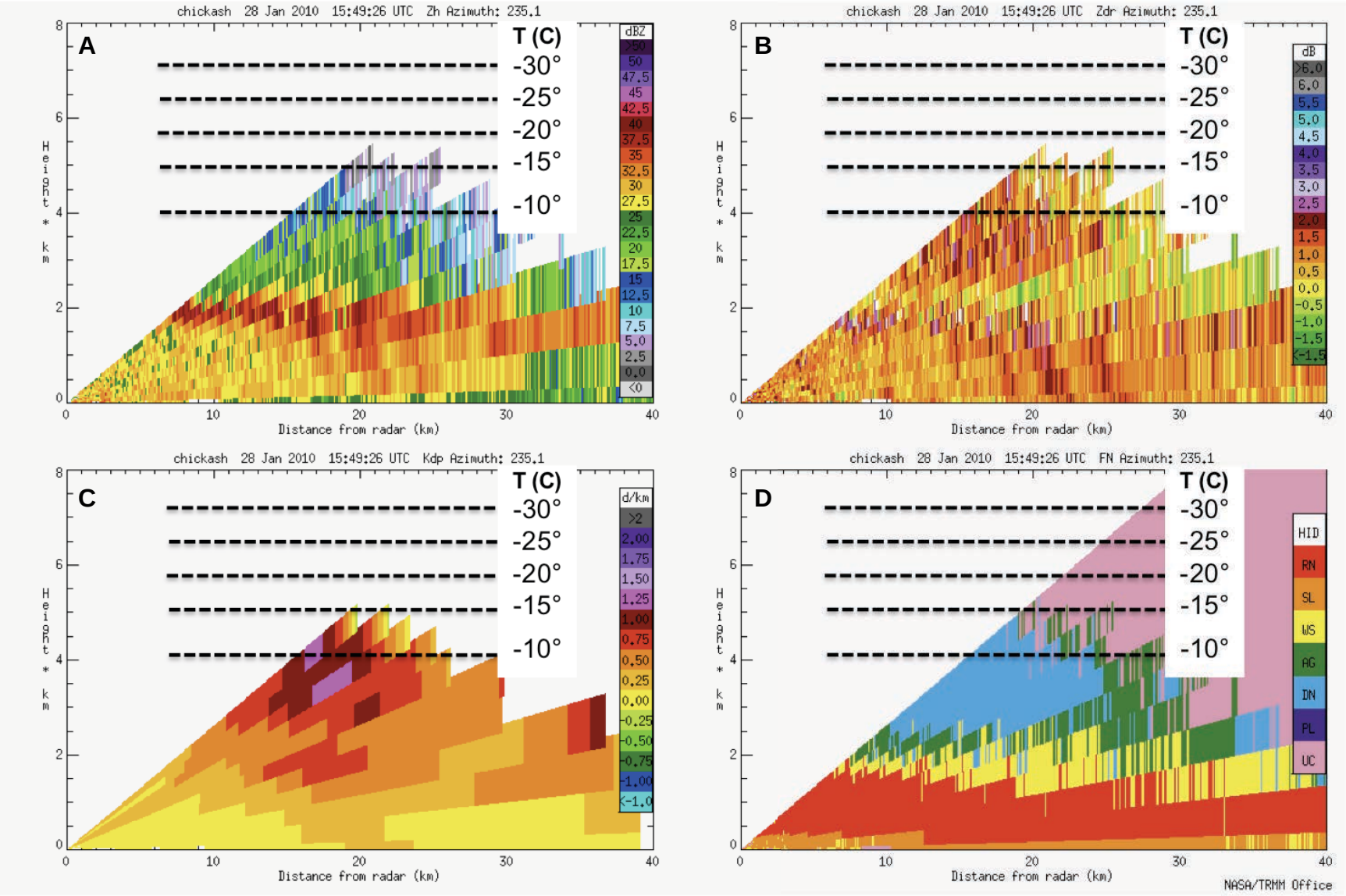

Fig. 3.24. CASA KSAO vertical cross section scan of Z_H (a), Z_{DR} (b), K_{DP} (c), and hydrometeor classification (d) between plates, dendrites, dry aggregated snowflakes, wet snow, sleet, and rain with 15 UTC KOUN sounding isotherms from Fig. 3.19.

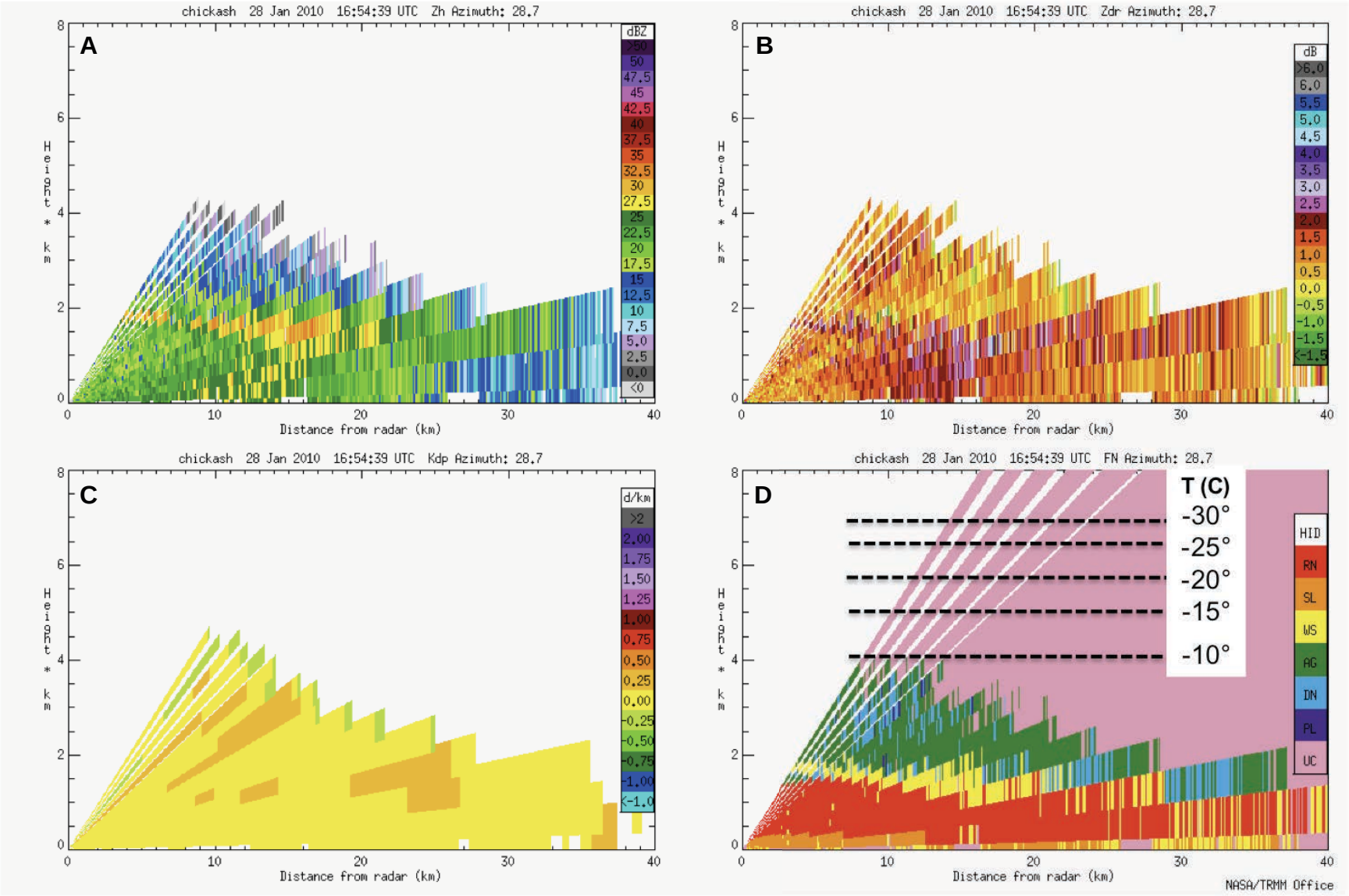

Fig. 3.25. CASA KSAO vertical cross section scan of Z_H (a), Z_{DR} (b), K_{DP} (c), and hydrometeor classification (d) between plates, dendrites, dry aggregated snowflakes, wet snow, sleet, and rain with 15 UTC KOUN sounding isotherms from Fig. 3.19.

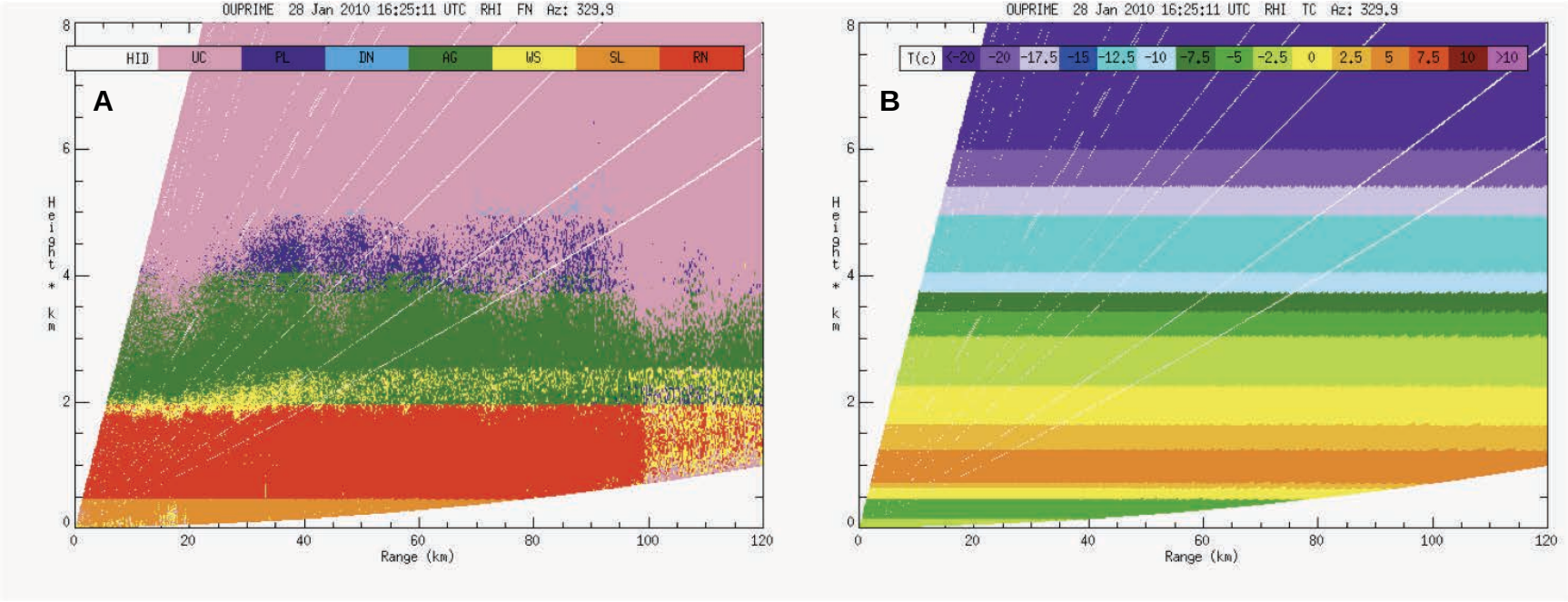

Fig. 3.26. OU-PRIME vertical cross section scan of hydrometeor classification (a) between plates, dendrites, dry aggregated snowflakes, wet snow, sleet, rain, and unclassified echo using temperature (b) as a variable after interpolation from the 15 UTC KOUN sounding in Fig. 3.19.

CHAPTER FOUR

Microphysical Processes in Winter Storms Identified with the Melting Layer Detection and Hydrometeor Classification Algorithms

4.1 Overview

The hydrometeor classification algorithm developed herein is intended to reveal four microphysical processes in winter storms. These include the dendritic growth zone, the transition zone as evidenced by the vertical bright band, the melting layer and its transformation into an isothermal layer, as well as the refreezing zone where raindrops/semi-melted ice particles become ice pellets just above the surface. We define the 0°C level to exist at the melting layer (bright band) top (Boodoo et al. 2010). While these phenomena are validated by temperature information from upper-air soundings, this analysis demonstrates that these processes can be identified solely by the polarimetric radar variables. Doppler velocity indicated fall speed spectra from vertically pointing radars are also explored to further understand the nature of winter storms.

4.2 Dendritic growth zone

Long lasting signatures of enhanced K_{DP} and Z_{DR} near the -15°C level were isolated to determine the maximum K_{DP} and Z_{DR} values associated with dendrites during each winter storm case. These variables tended to maximize at and below this temperature level, as illustrated by the upper-level 16.9° PPI scan of the hydrometeor classification and interpolated 12 UTC temperature field during stratiform winter precipitation in Fig. 4.1. The melting level in this case is marked by wet snow while rain and possibly sleet exist below where the sounding T < 0°C.

We are confident in the upper K_{DP} and Z_{DR} bounds derived from scattering simulations because these values agree extremely well with observations from each radar platform. Maximum observed Z_{DR} ranged from 2-2.5 dB for C-band OU-PRIME as well as X- and S-band CSU-CHILL. Then the CASA radars showed Z_{DR} ~ 4 dB within dendritic growth zones, which is probably not trustworthy because the Z_{DR} bias for these radars was determined manually and might not be ideal for upper-portions of the storm. Therefore, these observed Z_{DR} values for dendrites are lower than the maximum values expected from scattering simulations (3.9 dB). However, these crystals were viewed by the radar at high elevation angles, which can account for up to ~1.25 dB Z_{DR} decrease when the elevation angle reaches 30°. The Z_{DR} elevation angle effect discussed in Section 2.3.2, whereby oblate crystals produce a lesser Z_{DR} return when the radar beam is no longer oriented along the horizontal axis of the hydrometeor, may account for this discrepancy.

Maximum K_{DP} values modeled for dendrites at X-, C-, and S-band were 1.97, 1.14, and 0.57° km^{-1} respectively, which agreed well with previous studies as stated in Section 2.3.2. For a comparison between X- and S-band, coincident CSU-CHILL dual-wavelength vertical cross section (RHI) scans of K_{DP} and the hydrometeor classification through dendritic growth zones are shown in Figs. 4.2 and 4.3 from two different time periods on 3 February 2012. The top panels in each figure show S-band data with corresponding X-band data in the lower panels. K_{DP} values are approximately three times greater in magnitude at the shorter wavelength, which produces more robust and clear dendritic classification over aggregates. It is notable that K_{DP} at S-band in Fig. 4.2-a was barely above zero, which could have been attributed to noise, while K_{DP} in Fig. 4.2-c at X-band wavelength was clearly indicative of dendritic crystals. In the absence of a strong S-band K_{DP} signature, the S-band HCA in Fig. 4.2-b (incorrectly) identifies plates near

echo top height where *SNR* is low and therefore Z_{DR} is erroneously high. This demonstrates the greater discriminatory power of K_{DP} at shorter wavelengths for ice crystal classification.

Maximum K_{DP} from CSU-CHILL at X- and S-band during this case were 2.0 and 0.7° km^{-1}, respectively. K_{DP} reached 2.3° km^{-1} during the 2009 winter storm for the CASA X-band KCYR radar, which is shown by the vertical cross section scan in Fig. 4.4. The highest value recorded from either the 2009 or 2010 storm by the C-band OU-PRIME radar was 1.3 ° km^{-1}, illustrated by RHIs though a dendritic growth zone in Fig. 4.5 and 4.6. These observed specific differential phase values are only slightly higher than those suggested by our scattering simulations (by 0.1-0.3° km^{-1} between S- to X-band respectively). This is likely because we could only model oblate particles as large as 1 cm but dendrites commonly exceed this value in nature (PK97).

Another additional discrepancy indicated by observations but not accounted for in the scattering model was a slight reduction in ρ_{HV} within the dendritic growth zone (Ryzhkov et al. 2011). This signature was not robust or persistent, but is noticeable in Fig. 3.17 and 4.5. Prolific ice crystal growth by vapor deposition could produce some extremely large, low bulk density crystals in the presence of other smaller dendrites. Larger crystals might also have more erratic fall behavior. Varying density and canting between hydrometeors as well as a broadened size distribution could explain the reduced ρ_{HV} pattern. This hypothesis should be confirmed with a more sophisticated electromagnetic scattering model that can represent larger particle diameters.

Figs. 4.1-4.6 also demonstrate that K_{DP} and sometimes Z_{DR} tend to decrease above the dendritic growth zone toward echo top height. This usually leads to classification of dry aggregated snow in the upper-most regions of the cloud. We do not believe this phenomenon is an artifact caused by high radar viewing angle, which would have caused a systematic decrease

in these variables from lower to higher rays, not along the same ray as demonstrated in these figures. While classification of aggregates above dendrites is physically unrealistic, these polarimetric signatures could be indicative of small, less numerous, pristine ice crystals. Lower ice water content could also explain the reduction in $K_{DP.}$ Smaller sized, less numerous, and perhaps less oblate crystals would produce lower Z_{DR} according to the sensitivity studies discussed in Section 2.3.2.

Rauber and Tokay (1991) suggest that under sufficient water saturation conditions, crystals may be too small near cloud top to incorporate excess vapor, which often results in the formation of supercooled liquid drops. As illustrated in Fig. 4.7 (from PK97: Fig. 2-39 and 2-41), these drops can freeze into spatial crystals or double dendrite crystals, which may continue to grow by vapor deposition as they descend. If the temperature is close to -15°C, dendritic branches will form. Without in-situ observations of super cooled liquid drops or a characterization of the temperature or humidity within the upper region of the cloud (where hydrometeors are too small to be detected by weather radars), we cannot make any claims about the possible link between aviation icing hazards and dendrites classified by this algorithm. However, a field study could be designed to test the HCA's use in discerning this relationship.

High-resolution RHI images, such as Figs. 4.5 and 4.6, often revealed that dendritic growth zones exist above enhanced bright band melting signatures and enhanced Z_{DR} "curtains" of heavier rain below these melting regions. This could correspond to aggregation of dendritic crystals aloft that, when wetted due to melting within the bright band, produce larger, oblate raindrops near the surface. An additional "heavy" rain category could be added to the algorithm to represent this Z_{DR} variability. Many studies have postulated that surface precipitation types and rates are modulated or intensified by the habit and type of crystals falling through the

melting layer (Fujiyoshi and Wakahama 1985, Rauber et al. 2001, Thériault et al. 2010, Kennedy and Rutledge 2011).

4.3 Vertical bright band transition zone

Stewart et al. (1992) describe the transition zone between rain, freezing rain, sleet, and snow as well as their separation by a vertical bright band (VBB). Their schematic drawing of this common environment is shown in Fig. 4.8. The hydrometeor classification algorithm developed here does a good job discriminating where the melting layer descends toward the ground as a VBB as opposed to areas of strong precipitation. The discriminating factor between these two scenarios is ρ_{HV}, which remains high for rain but is characteristically low where hydrometeors are melting. Z_H, Z_{DR}, and K_{DP} are strongly positive in both cases (Ryzhkov and Zrnic 1998a).

A vertical bright band structure is revealed in a CASA RHI with all four dual-polarimetric radar variables in Fig. 4.9 and the corresponding hydrometeor classification in Fig. 4.10. This “second cold” HCA result only classifies plates, dendrites, dry aggregated snowflakes, or wet snow. Since the algorithm identifies the melting layer height as a function of azimuth, not range (although it could be modified to do so in the future), it cannot decide to classify rain enclosed by the vertical bright band as well as dry aggregated snow beyond 15 km. The algorithm and surface weather reports confirm that snowflakes did fall to the ground in this region though. The algorithm accurately depicted the vertical bright band intersecting the ground, but erroneously classified dendrites close to the radar below the melting layer.

4.4 Melting and isothermal layer

The melting layer detection algorithm isolates individual radar bins where melting is most likely occurring and calculates the melting layer top, median, and base heights (Giangrande

et al. 2008). The melting layer top and base heights can also be used to approximate the depth of this phase change zone. During the 28 January 2010 ice storm in Oklahoma, a strong temperature inversion near 850 hPa existed above a low-level cold layer. While the surface temperature remained near -1.5°C throughout the entirety of the storm (~12 UTC to 00 UTC), these cold and warm layers changed relative depths and intensities (coldness and warmness, respectively) to support a transition from freezing rain to sleet by about 21 UTC according to ASOS reports. The upper-air soundings from 15 UTC on 28 Jan through 00 UTC on 29 Jan are shown in Fig. 4.11.

The minimum temperature within the surface cold layer lowered from -4.5°C to -8.3°C between 15 UTC and 18 UTC and then increased slightly to -7.0°C by 21 UTC and -4.5°C at 00 UTC. Meanwhile, the maximum inversion temperature decreased with time from 5.6°C at 15 UTC and 18 UTC to 3.8°C at 21 UTC and finally 3.6°C by 00 UTC. The cold layer extended from the surface to 455 m, 655 m, 685, and finally 655 m AGL according to these soundings. As the cold region deepened, the elevated layer where T > 0°C thinned from approximately 1800 to 1000 m.

It is well understood that the radar bright band is typically narrower than the layer where temperatures are above freezing since signs of melting usually do not begin until a couple hundred meters below the 0°C level (Austin and Bemis 1950). The bright band depth indicated by the melting layer detection algorithm during this time only ranged between 200-400 m, but actually deepened slightly over time. This was visibly noticeable in the high-resolution OU-PRIME RHIs, which were used to track the minimum correlation coefficient, the melting layer top, median, and base heights, as well as the melting layer depth shown in Fig. 4.12. Only data within 5-40 km of the radar and where *SNR* > 5 dB were included in this analysis to exclude

errors induced by beam broadening and ground clutter. 5-7 min update frequency between RHI scans introduced some variability or noisiness in these time series data.

ρ_{HV} remained above ~0.88 within the radar bright band while freezing rain was reported at the surface, but became markedly lower just before the surface precipitation transition to sleet around 21 UTC. Fig. 4.13 shows one of the OU-PRIME vertical cross section scans used to create the plot in Fig. 4.12, which is very representative of the ρ_{HV} field from 2100 – 2359 UTC during sleet. Lower ρ_{HV} beyond the typical melting layer values suggests a modification of the phase change process such that hydrometeor diversity enhanced even more than usual. This RHI also shows excursions of low ρ_{HV} extending toward the surface from the base of the melting layer. Furthermore, there are several pixels of low ρ_{HV} below these excursions near the ground.

This long-lived, robust radar signature suggests that particles were not completely melting within the temperature inversion, such that semi-melted particles survived and descended toward the surface. This is further supported by the fact that the temperature inversion was weakening, possibly due to latent cooling associated with melting, while the surface cold layer was deepening and becoming colder. These wet snowflakes and/or partially melted drops would have readily frozen into ice pellets within the low-level cold layer because of their imbedded ice nucleus (Thériault et al. 2006). Once ice pellets form, they can help initiate contact freezing with supercooled raindrops. The quasi-liquid layer provided by ruptured liquid core pellets and semi-melted particle surfaces may also help fuse nearby ice pellets together.

Contoured Frequency by Altitude Diagrams, or CFADS, of Doppler velocity were constructed to examine the vertical structure of the melting layer during this transition from another perspective (Yuter and Houze 1995). OU-PRIME performed vertically pointing scans during this event. The radial velocity in this case measures the difference between air motion

(negligible in synoptically forced ascent regions) and hydrometeor fall speeds. Data below 0.5 km AGL are not shown due to ground clutter contamination.

The Doppler spectra of stratiform precipitation began to shift after remaining relatively constant from 12 – 20 UTC. Fig. 4.14 shows four CFADS of Doppler velocity during the 22 UTC hour. Meaningful trends in these data that might have indicated riming or some low-level precipitation change were not apparent between 21-22 UTC. 22 UTC CFAD observations and the hydrometeor classification from this time period confirm that pristine crystals typically only fall at 0-1 m s^{-1} (negative in these plots), increasing slightly toward 2 m s^{-1} during aggregation (Spek et al. 2008). Terminal velocity may exceed 2 m s^{-1} where riming occurs (Zawadzki et al. 2001), which was not observed in this study. Fall speeds drastically increase up to 8-10 m s^{-1} within the melting layer where centimeter-sized, irregular snowflakes collapse into denser, millimeter-sized drops with less aerodynamic drag force. The region over which this fall speed increase occurs, between the red horizontal lines in Fig. 4.14, serves as a proxy for the melting layer depth, so the progression in this figure indicates that the melting layer did in fact deepen from less than 1 km to over 1.5 km as it descended toward the ground.

Unlike the sounding analysis, which may not be representative of an entire region or time period, these unique radar observations suggest an isothermal layer was forming. This is an important microphysical process for determining surface precipitation type (Stewart et al. 1992, Heymsfield et al. 2004). Melting requires latent heat from the surrounding environment, which cools the temperature inversion over time toward 0°C. A deepening, or spreading out, of the elevated warm layer, which can be identified from this kinematic and microphysical radar analysis but not from the soundings, usually accompanies this cooling process.

By the same token, evaporation below cloud base typically cools and moistens the atmosphere, which can modulate the surface cold layer to promote sleet over freezing rain. Both of these microphysical processes were likely instrumental in the surface precipitation type transition and melting layer evolution observed during this case study. These microphysical and kinematic melting layer metrics could be incorporated into a more advanced hydrometeor identification algorithm since they seem directly and indirectly indicative of the transition between liquid to frozen precipitation types at the surface (Chandrasekar et al. 2011)

4.5 Refreezing zone

It has been demonstrated that the smallest supercooled drops or semi-melted particles below the melting layer where T < 0°C may freeze into ice pellets before larger particles do so because they contain less liquid water (Thériault et al. 2006). This is contrary to the volume dependence on freezing for much smaller cloud particles, which suggests larger cloud drops freeze more readily than smaller cloud drops since the former have a higher probability of containing a freezing nucleus with a smaller energy barrier to overcome (PK97). This size-sorting process may be critical in explaining the low-level trends observed in Z_H, Z_{DR}, and ρ_{HV} during times that freezing rain occurred at the surface as opposed to sleet during the 2010 ice storm. Fig. 4.15 shows a vertical cross section of these three variables plus K_{DP} through stratiform precipitation at 1625 UTC while Fig. 4.16 illustrates the same at 2220 UTC. There is no vertical variation between these variables in the earlier time period when freezing rain occurred, but a horizontally oriented enhancement of Z_H and Z_{DR} with a decrease in ρ_{HV} is noticeable around 680 m AGL at the later time period when sleet was reported at the surface. This height corresponds exactly with the height of the surface cold layer indicated by the 21

UTC sounding in Fig. 4.11-c. In fact, the signature becomes well established for the first time around 2130 UTC shortly after sleet is first indicated by a central OK ASOS station. The polarimetric refreezing pattern gradually intensifies and deepens vertically along with the surface cold layer evolution described previously. The Z_H signature is slightly elevated above the ρ_{HV} and Z_{DR} trends. K_{DP} also exhibits a slightly positive trend during this time, but not in every radar scan. More fine-scale K_{DP} smoothing and calculation is likely necessary to discern the true K_{DP} trend in the refreezing zone, but was not attempted for this work.

To demonstrate the prolific nature of this multi-variate signature in time and space during the precipitation type transition period, OU-PRIME RHIs are used to calculate the mean Z_{DR}, mean Z_H, and minimum ρ_{HV} along a single azimuth within 5-40 km ranges from the radar. These azimuthal averages are presented in Fig. 4.17 during periods of time when this refreezing signature was and was not present. These two time periods contain the RHIs shown in Fig. 4.15 and 4.16. Each colored line in Fig. 4.17 represents data from a separate radar scan, with later time periods in warmer colors. Between 16-17 UTC, there is no vertical variation of Z_H or Z_{DR} below the melting layer, which is centered ~1.8 km. Minimum ρ_{HV} within these scans increases toward the surface, characteristic of stratiform rain and freezing rain. These variables have a significant trend toward the surface in every scan between 22-23 UTC. It is notable that these trends are evident in the time- and range-averaged fields. Z_{DR} begins to increase around 700 m AGL (height of the surface cold layer) while ρ_{HV} decreases and Z_H exhibits an increase then decrease about an inflection point. Z_H is slightly higher during the sleet time period than for freezing rain, but this is simply because the stratiform precipitation captured in the 22-23 UTC RHIs was slightly more intense.

Ryzhkov et al. (2011) documented these same refreezing zone patterns during other mixed-phase wither storms with S- and C-band polarimetric radars, but the physical origin of these trends has not yet been explained. It seems obvious that these robust dual-polarimetric radar signatures are associated with the refreezing process since decreased ρ_{HV} indicates diversity among the particle size distribution, enhanced Z_{DR} indicates a change in density and/or oblateness, and Z_H is also sensitive to particle size and number concentration. We argue that the preferential freezing of smaller drops before larger ones could essentially mask the polarimetric contributions of these small, nearly spherical particles because of their decreased dielectric effect and density of ice compared to water. Ice pellets also tumble as they fall, as opposed to liquid drops, so their fall behavior should further decrease their contribution to Z_{DR} and K_{DP} according to the discussion in Section 2.3.6. The remaining liquid drops would be very large and oblate, which may help overcome the usual Z_{DR} dilution effect of small spherical drops. Then the drop size distribution would be effectively characterized only by the large liquid hydrometeors that have not yet frozen. This process would presumably produce an enhancement of Z_H and Z_{DR} with a decrease in ρ_{HV}, which matches these observations. Kumjian and Ryzhkov (2008) used a similar size-sorting argument to explain the Z_{DR} arc associated with tornadic supercells.

The differential variables may continue trending toward the surface because the drop size distribution is continually changing as the largest drops finally freeze. Conversely, Z_H exhibits a much more muted signature and actually recovers below an inflection point. This is most likely due to the competing dielectric effect, Z_H's insensitivity to hydrometeor shape, and a possible decrease in number concentration as supercooled liquid drops freeze into ice pellets. Z_{DR} and ρ_{HV} are conversely insensitive to total number concentration, so their trends usually extend all the way toward the surface. The size-sorting refreezing process and coagulation of frozen drops to

ice pellets could also increase D_M, the mass-weighted mean volume diameter (Thériault 2010). This IP-b growth mechanism supports a systematic increase in Z_{DR} and Z_H.

These theories seem plausible given the nature of dual-polarimetric variables for frozen hydrometeors explored in Chapters 2 and 3 of this thesis. A microphysical bin model simulation and extensive winter storm field observations of drop size distributions within the lowest 2 km of the atmosphere should be carried out to test the true origin of this distinctive refreezing pattern. More sophisticated electromagnetic scattering simulations could also be conducted.

The CASA radars also detected a refreezing pattern in the 2009 case study very close to the radar site ahead of an approaching vertical bright band. The surface precipitation type was reported to transition from rain to freezing rain, sleet, and finally snow by ASOS as the vertical bright band progressed through the domain. A CASA KSAO vertical cross section of Z_H, Z_{DR}, K_{DP}, and ρ_{HV} through this combination transition-refreezing zone is illustrated in Fig. 4.18. There is no trend in K_{DP} according to this plot, but this is likely because a more fine-scale K_{DP} smoothing and calculation technique is required. Robust, horizontally oriented signatures of Z_H, Z_{DR}, and ρ_{HV} are present near the surface within the first 8 km of the radar. These trends follow the outline of the surface cold layer according to our understanding of the vertical bright band and nearby sounding temperature data. The refreezing signature was only identifiable very close to the CASA radars. This is likely because sufficient vertical and horizontal resolution is needed to capture the drop size distribution fluctuations within each radar bin.

Polarimetric detection of the refreezing *process* is remarkable considering that pure rain, freezing rain, and sleet cannot be distinguished by the radar according to theory and practice. The indication of sleet by enhanced Z_{DR} and Z_H is ironic because this signature may actually be produced by the liquid hydrometeors in the PSD. Furthermore, scattering simulations suggest

that pure sleet without hydrometeors in various stages of freezing is actually associated with *lower* values of Z_H, Z_{DR}, and K_{DP}.

It is also significant that this signature can be identified by the radar *without temperature information* so long as the radar's spatial resolution is sufficient. This provides motivation to use gap-filling X-band radar networks for hydrometeor identification (McLaughlin et al. 2009) because the radar's angular resolution, or beam width, is determined by the radar's antenna size and wavelength. Shorter wavelength radars can achieve narrower beam widths for the same size radar dish as longer wavelength systems or can have the same beam width as longer wavelength systems with a much smaller, cheaper, and transportable antenna dish. Please see Table 3.1 for examples of this relationship for the radars used in this study.

The CASA X-band hydrometeor classification algorithm can actually detect this refreezing phenomenon, although it incorrectly identifies it as dendrites below the melting layer as shown in Fig. 4.19 for the corresponding dual-polarimetric radar variables in Fig. 4.18. This classification likely occurred because K_{DP} happened to be high ($> 0.25\ ^\circ\ km^{-1}$) in this region, which is not always the case depending on the calculation methodology for this variable. High Z_{DR}, moderate Z_H, and ρ_{HV} values still above what is expected within the melting layer will most likely prevent classification of the refreezing signature apart from dendrites or rain within this fuzzy-logic framework. Use of texture fields and/or two-dimensional membership beta functions within a more advanced algorithm could likely isolate the relatively low magnitude variations of these three variables. Texture fields should also improve the accuracy of the melting layer detection algorithm. Surface temperature (easily attainable in most locations) may still be the only variable that can indicate a transition between freezing rain and rain.

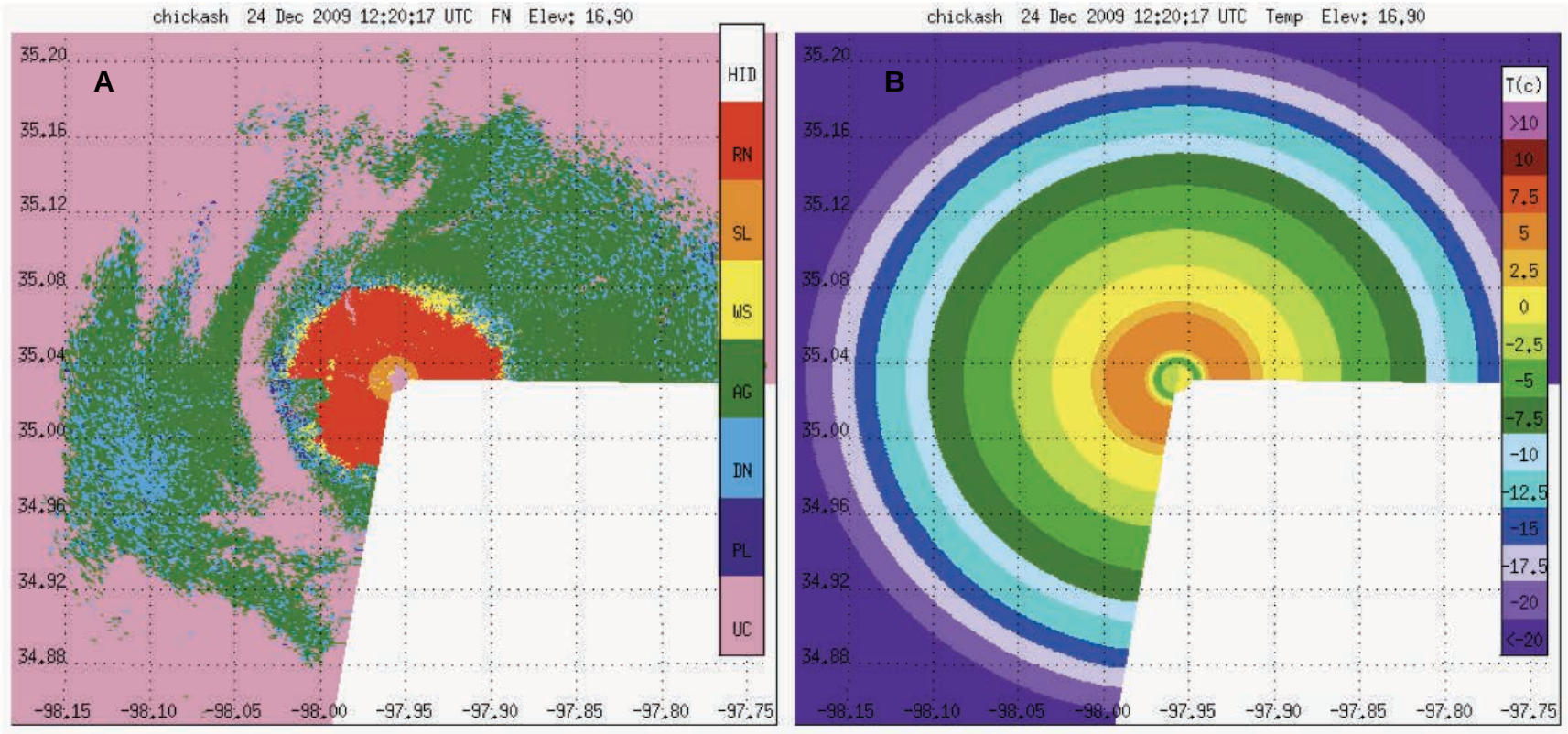

Fig. 4.1. PPI scans through stratiform winter precipitation at 16.9° elevation angle from the CASA KSAO radar of the a) hydrometeor classification between plates, dendrites, dry aggregated snowflakes, wet snow, sleet, rain, and unclassified non-meteorological or clear-air echoes; and b) interpolated temperature field from the 12 UTC nearby KOUN sounding.

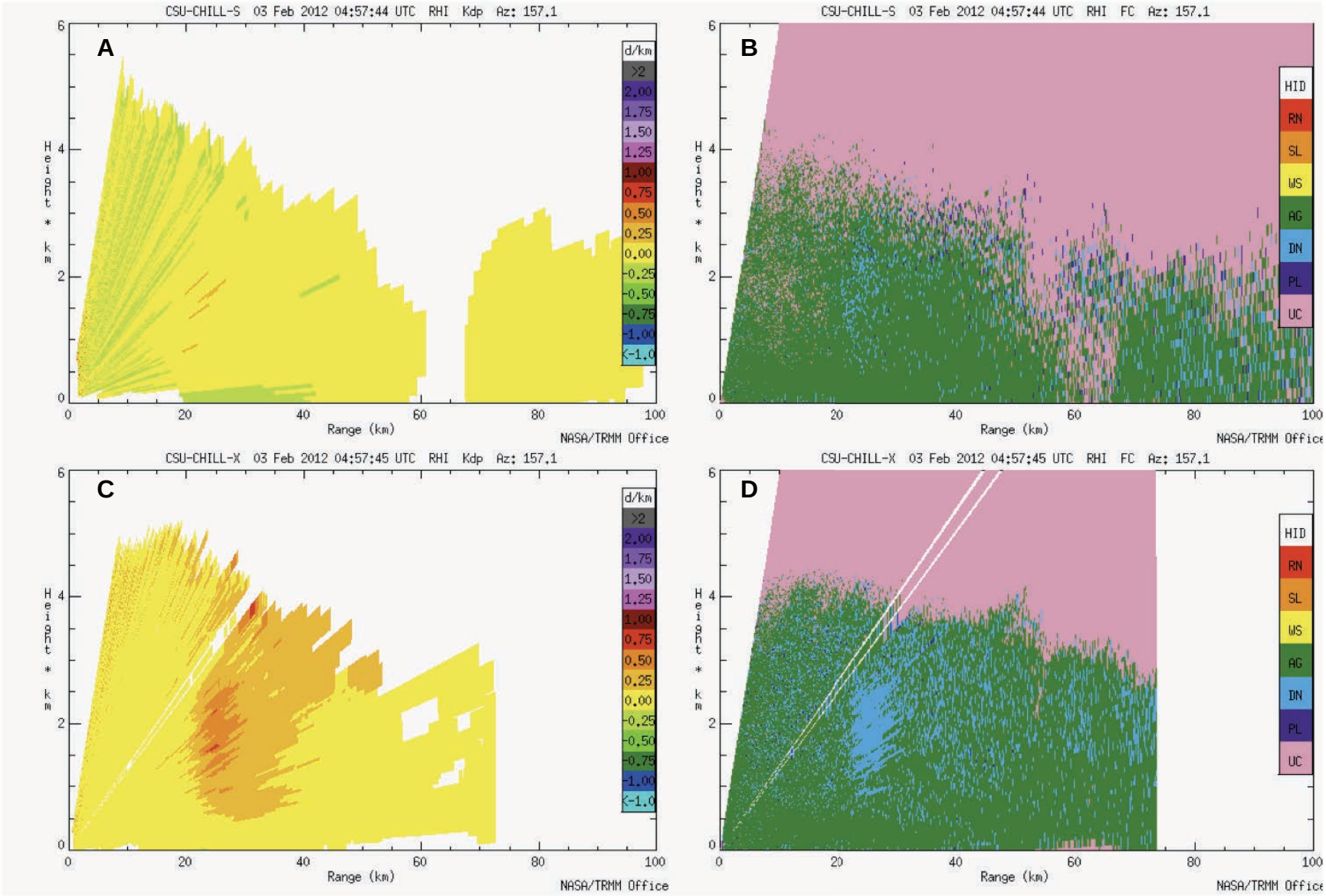

Fig. 4.2. Dual-wavelength S- (upper panels) and X-band (lower panels) CSU-CHILL vertical cross section scans of K_{DP} in a) and c) through a dendritic growth zone indicated by the hydrometeor classification algorithm in b) and d) at 0457 UTC on 3 February 2012.

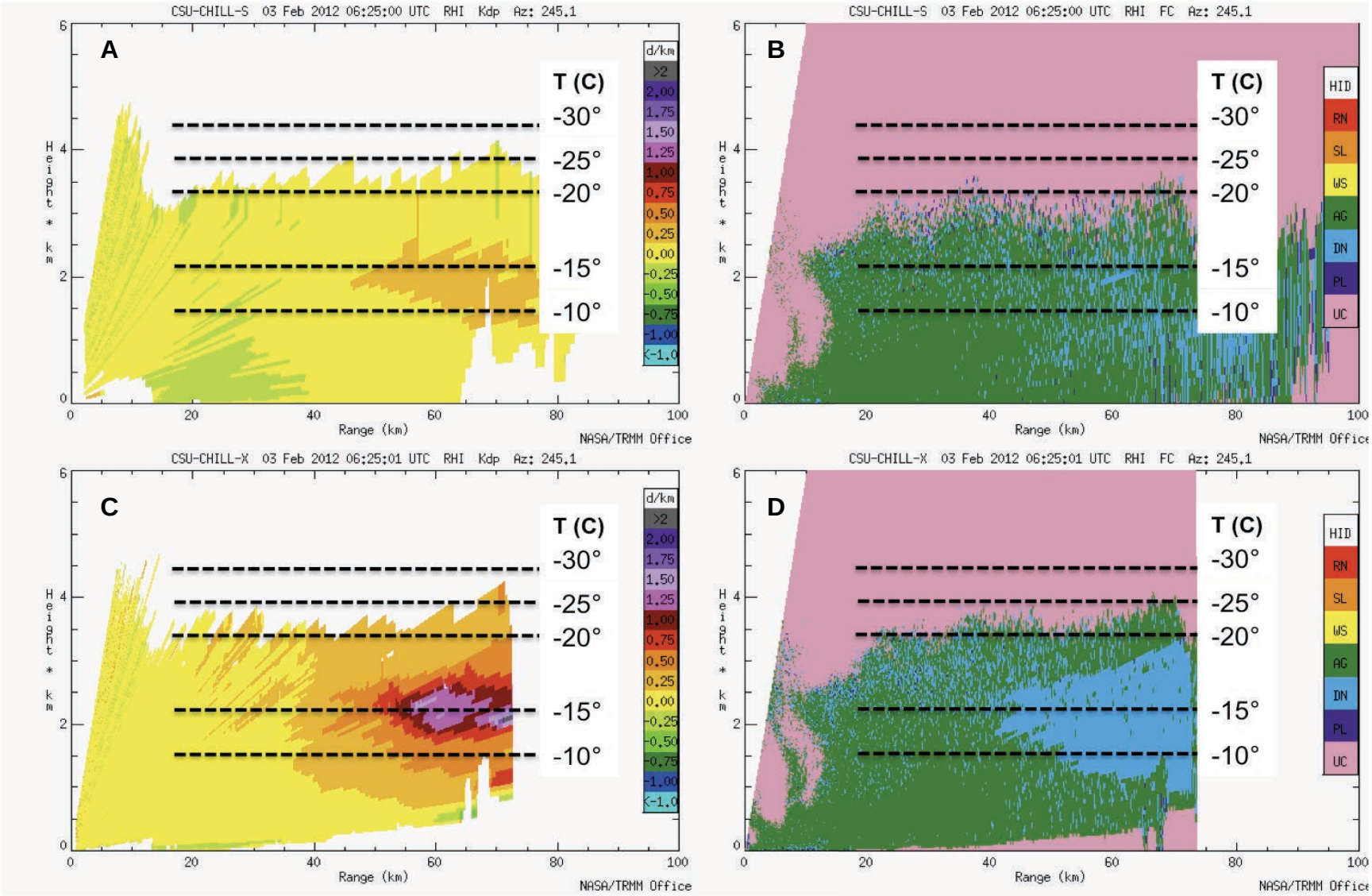

Fig. 4.3. Dual-wavelength S- (upper panels) and X-band (lower panels) CSU-CHILL vertical cross section scans of K_{DP} in a) and c) through a dendritic growth zone indicated by the hydrometeor classification algorithm in b) and d) at 0625 UTC on 3 February 2012 with 00 UTC KDNR (Denver, CO) sounding isotherms.

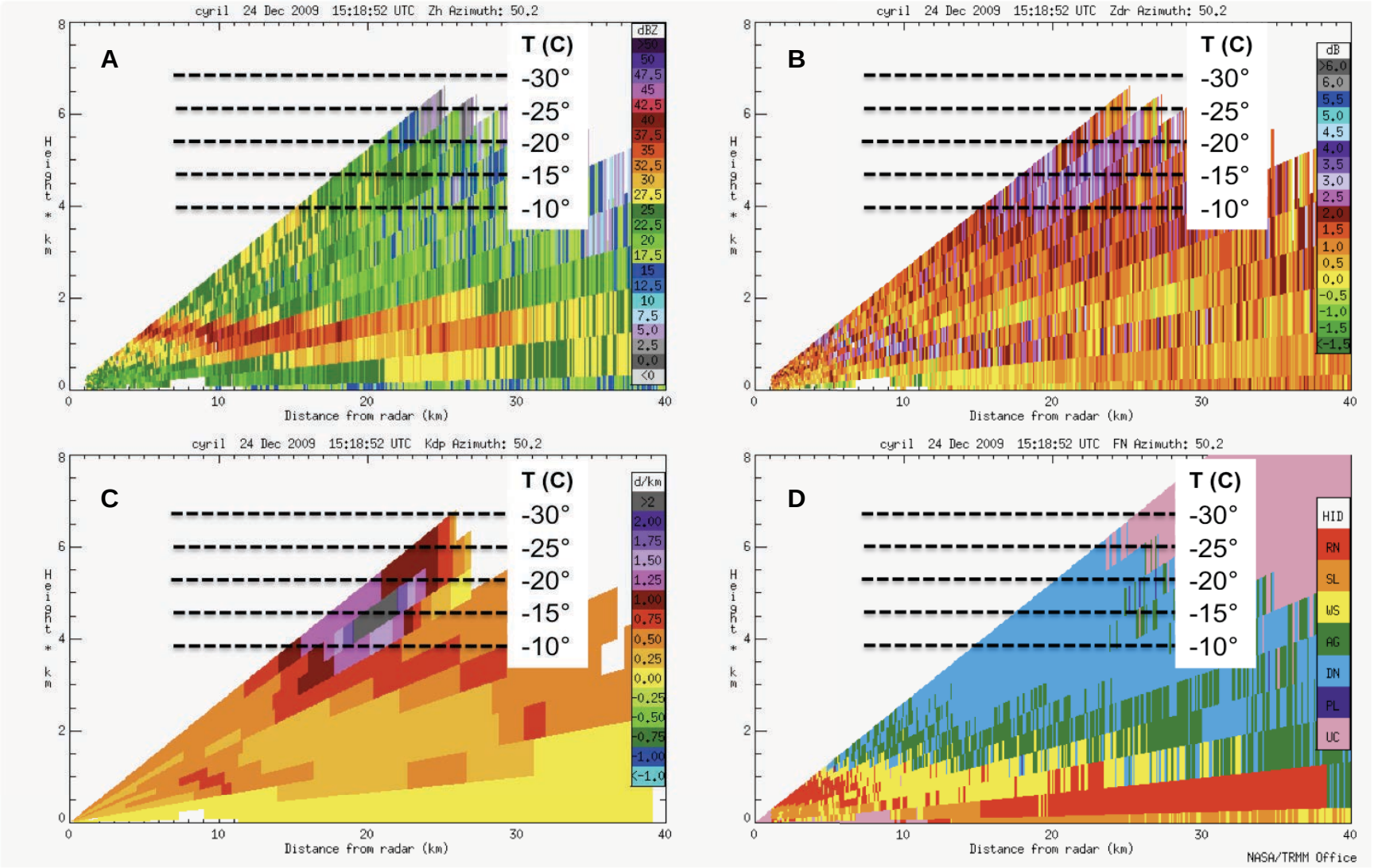

Fig. 4.4. CASA KCYR vertical cross section scan of Z_H (a), Z_{DR} (b), K_{DP} (c), and hydrometeor classification (d) between plates, dendrites, dry aggregated snowflakes, wet snow, rain, sleet, and unclassified echo through a dendritic growth zone on 24 Dec 2009 with 12 UTC KOUN sounding isotherms.

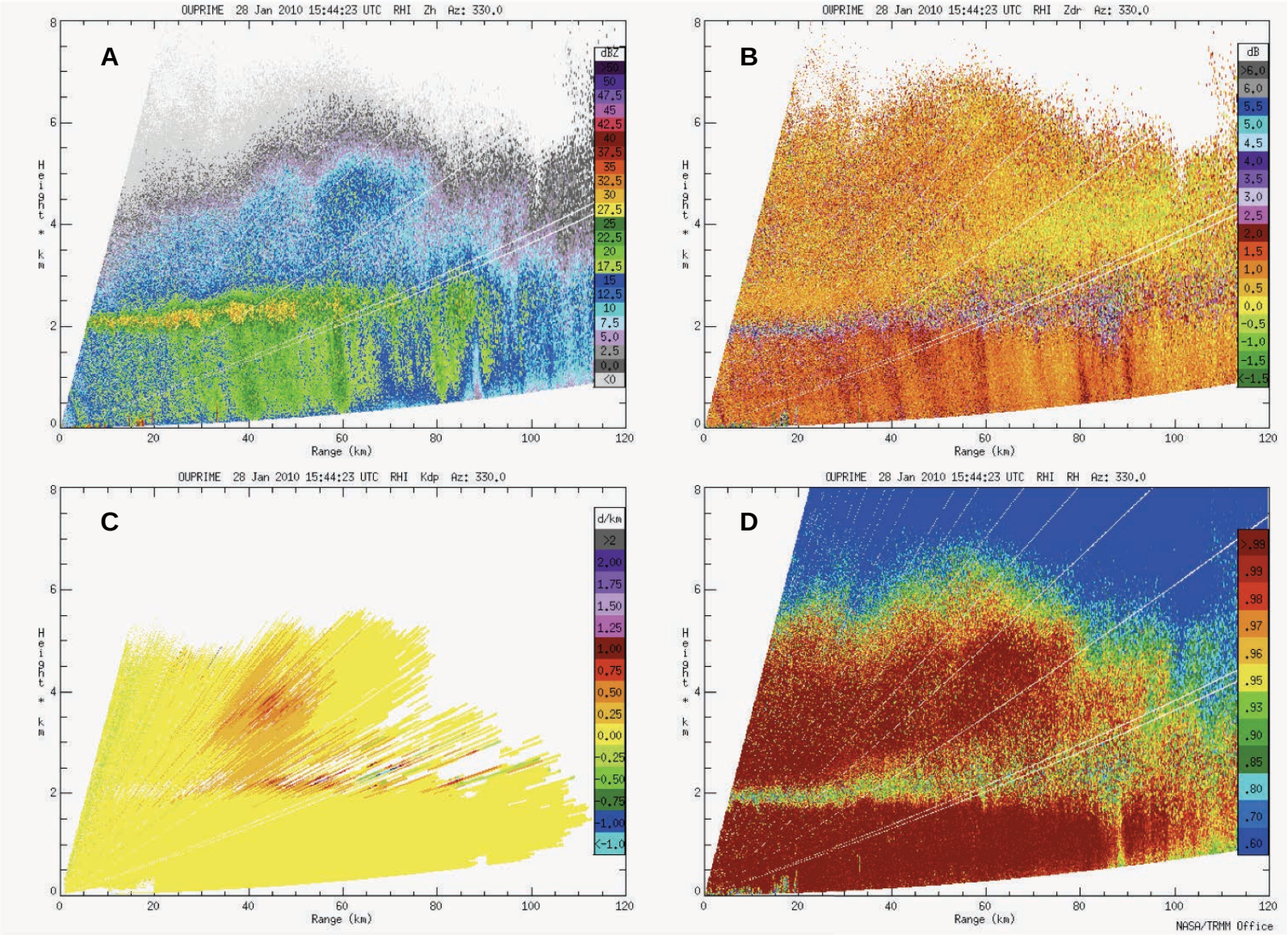

Fig. 4.5. OU-PRIME vertical cross section scan of Z_H (a), Z_{DR} (b), K_{DP} (c), and ρ_{HV} (d) through a dendritic growth zone on 28 January 2010.

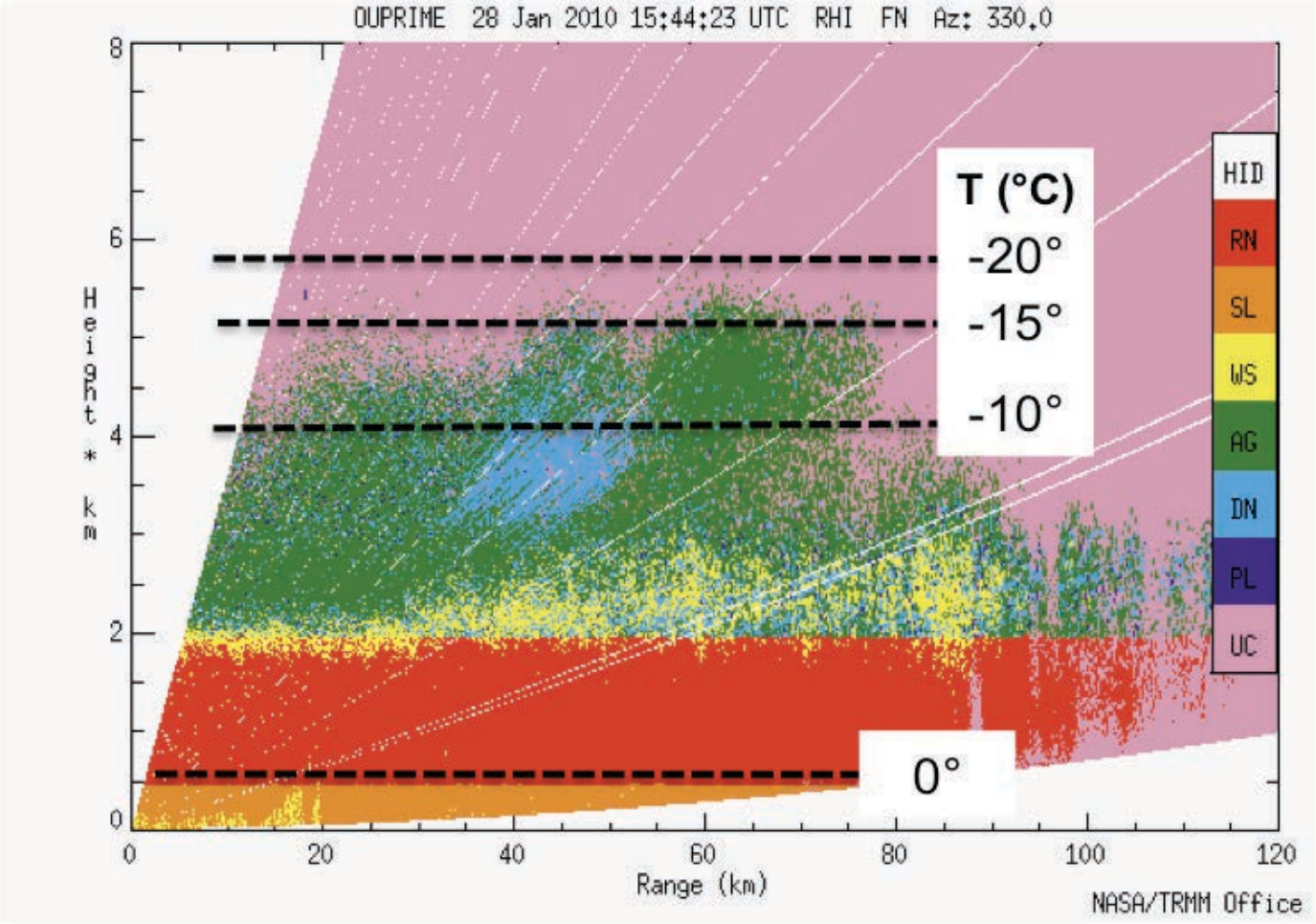

Fig. 4.6. OU-PRIME vertical cross section scan of hydrometeor classification between plates, dendrites, dry aggregated snowflakes, wet snow, rain, sleet, and unclassified echo through the dendritic growth zone from Fig. 4.5 with 15 UTC KOUN sounding isotherms from Fig. 4.11a.

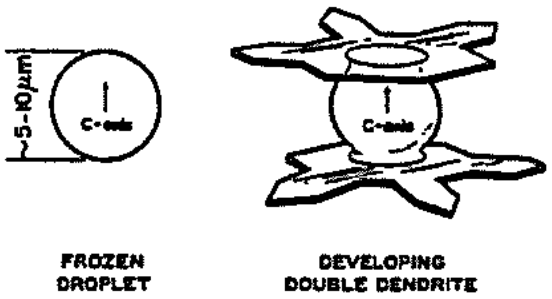

A

Fig. 2-39: Schematic drawing indicating the formation of a double star from a single-crystalline frozen drop. Note that competition for vapor causes irregular growth of opposing branches of the two crystals. (From Jiusto and Weickmann, 1973; by courtesy of Am. Meteor. Soc., and the authors.)

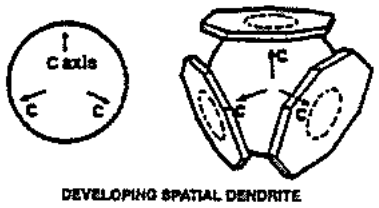

B

Fig. 2-41: Schematic drawing indicating formation of a spatial crystal from a polycrystalline frozen drop. (From Jiusto and Weickmann, 1973; by courtesy of Am. Meteor. Soc., and the authors.)

Fig 4.7. a) and b) from Pruppacher and Klett (1997).

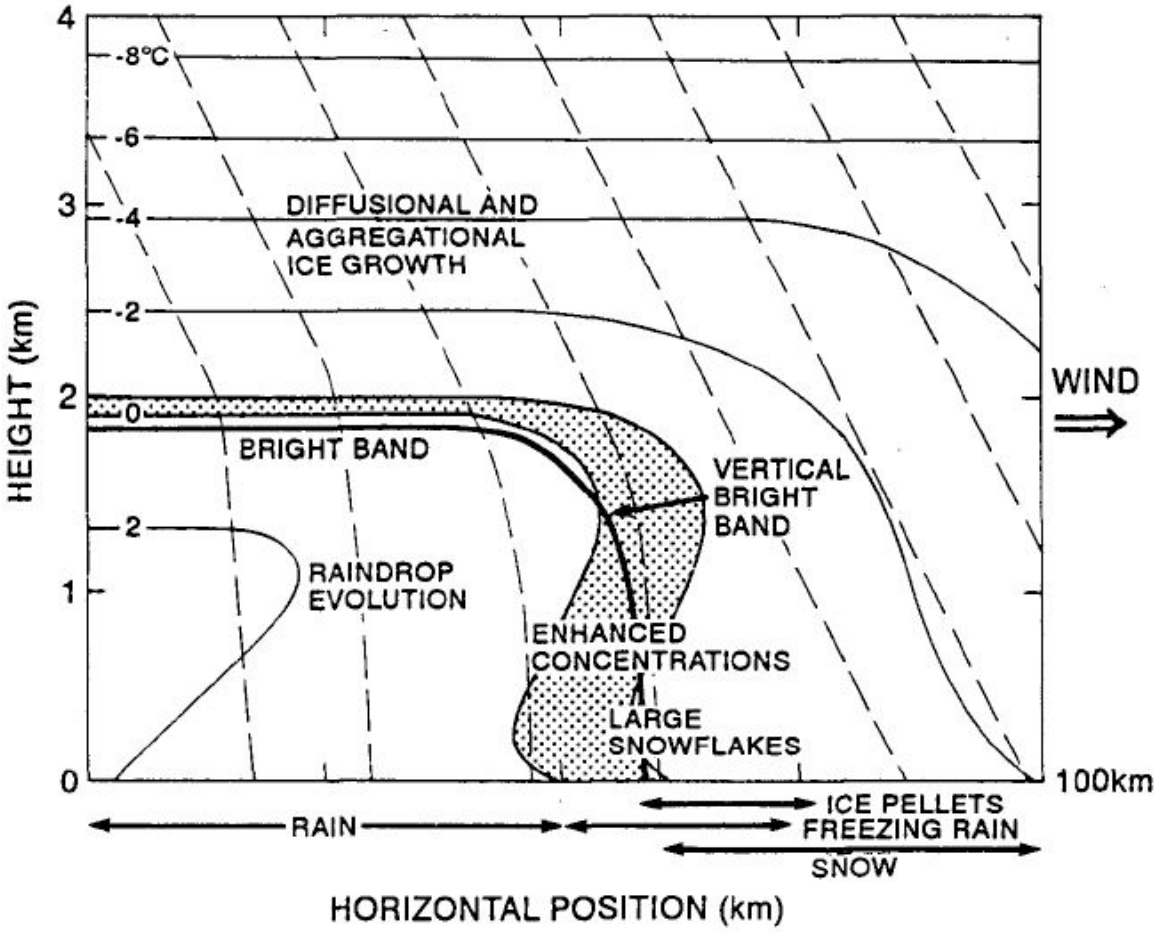

FIG. 6. Schematic vertical cross section illustrating some of the microphysical processes occurring within and adjacent to the precipitation-type transition region. The dotted area indicates the region with temperatures very close to 0°C.

Fig. 4.8. From Stewart et al. (1992).

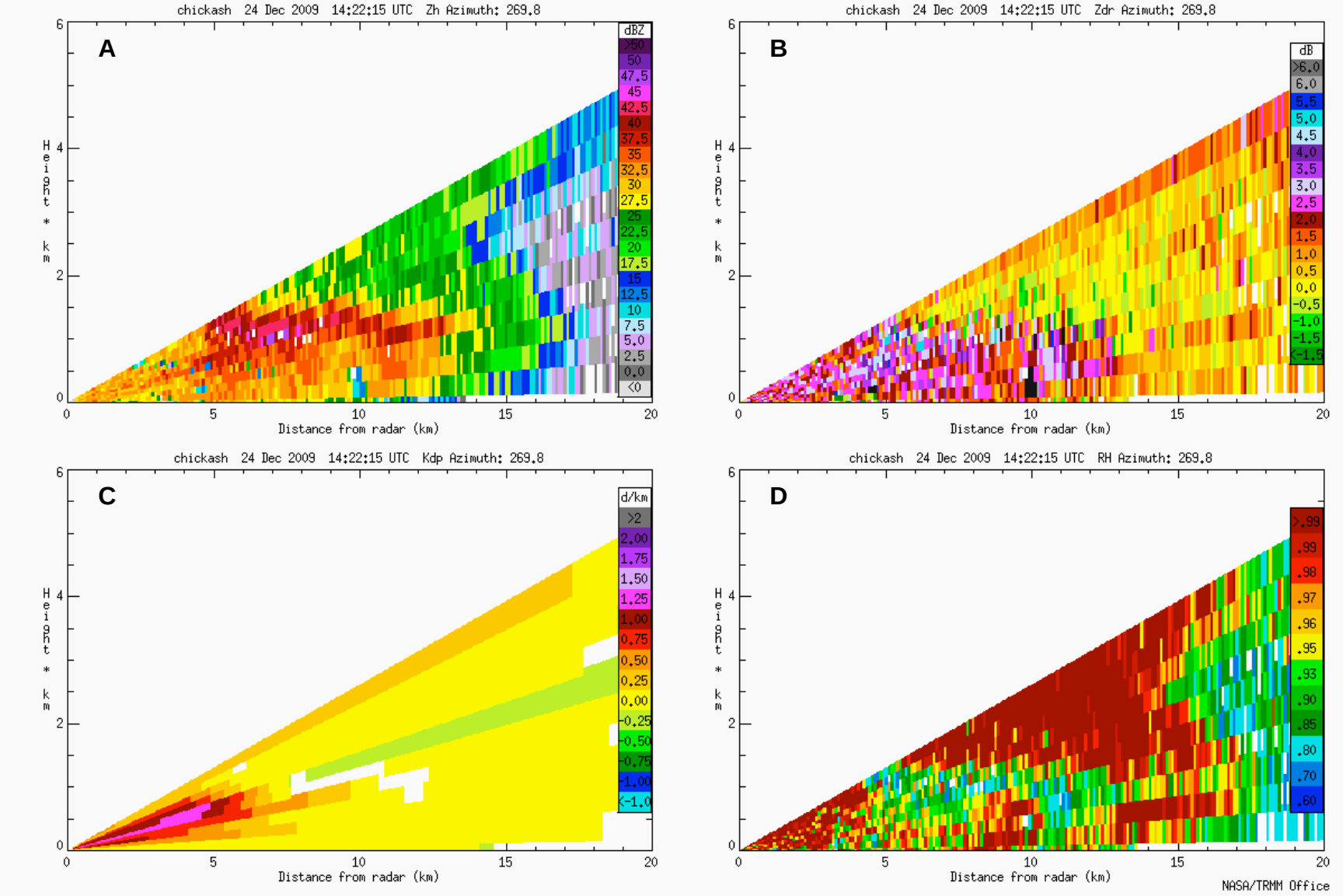

Fig. 4.9. CASA KSAO vertical cross section scan of Z_H (a), Z_{DR} (b), K_{DP} (c), and ρ_{HV} (d) through the vertical bright band, separating colder air with snow to the west (beyond 12 km) and warmer temperatures with a transition to rain at closer ranges to the radar.

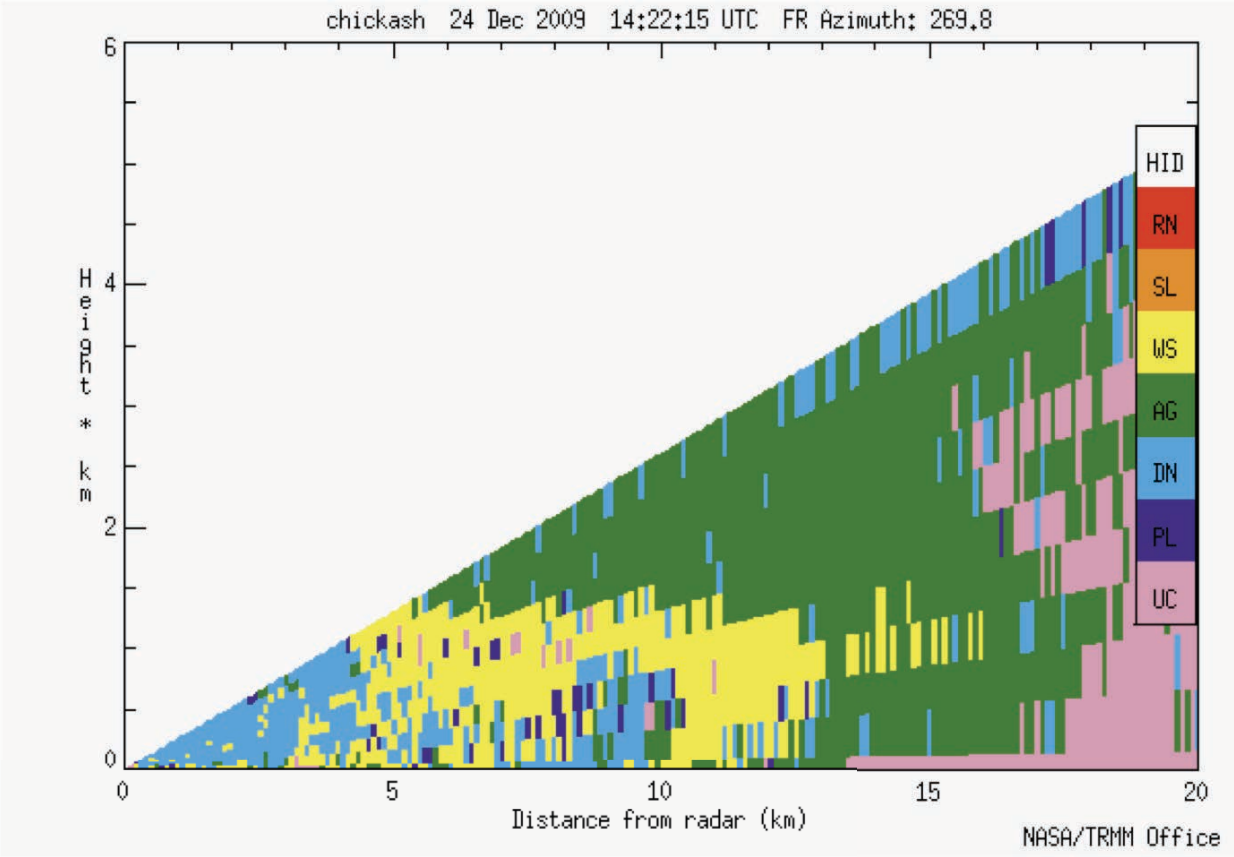

Fig. 4.10. CASA KSAO vertical cross section scan of hydrometeor classification between plates, dendrites, wet snow, dry aggregated snowflakes, and unclassified echo through a vertical bright band shown in Fig. 4.9 where the melting layer intersected the ground. Dendrites are erroneously classified close to the radar between 0-10 km range near the surface because only frozen or melting species were allowed in this classification algorithm step. Rain, freezing rain, and sleet were actually falling east of transition zone precipitation band in this region while aggregated snowflakes are correctly identified to the west, beyond the vertical bright band between 13-18 km.

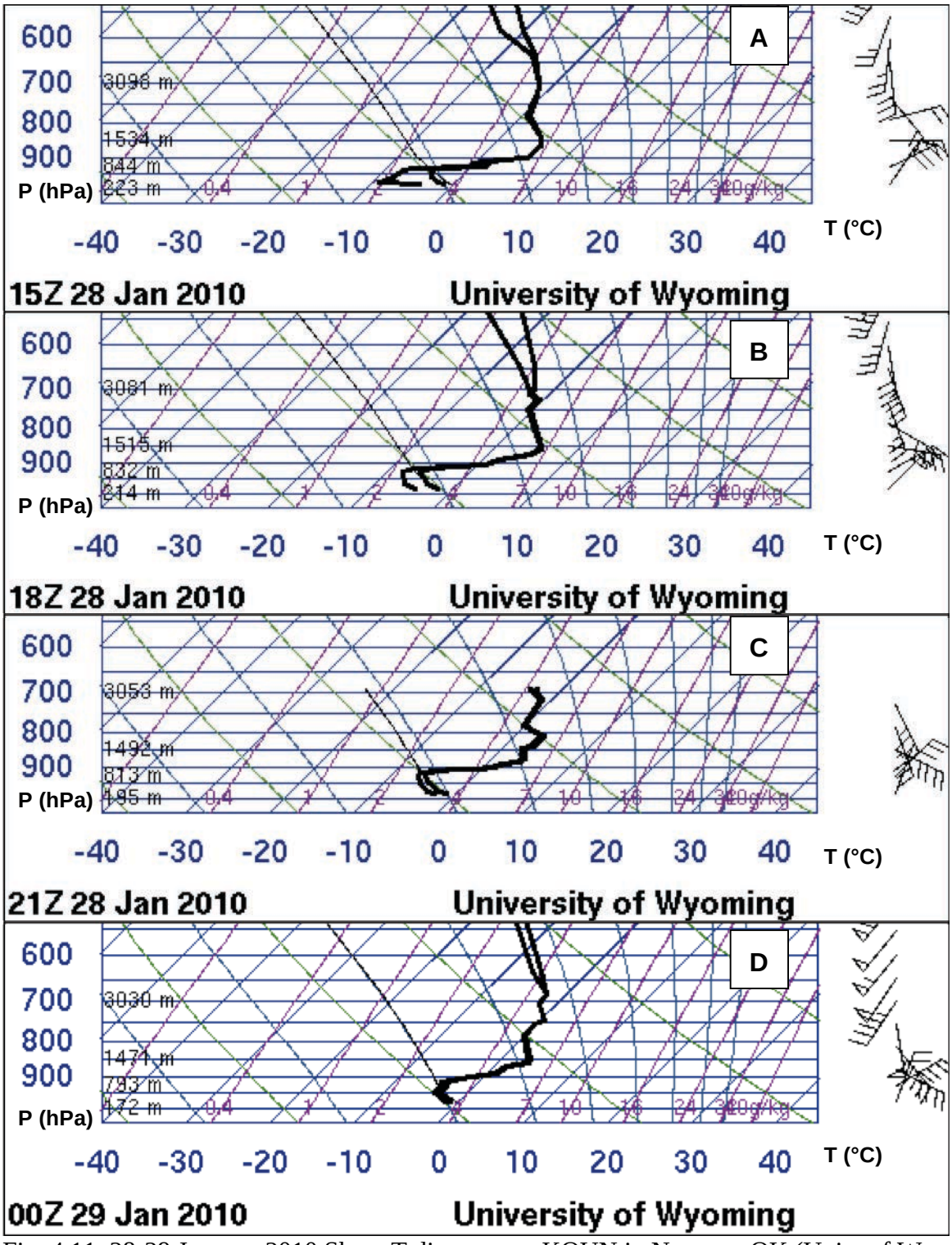

Fig. 4.11. 28-29 January 2010 Skew-T diagrams at KOUN in Norman, OK (Univ. of Wyoming).

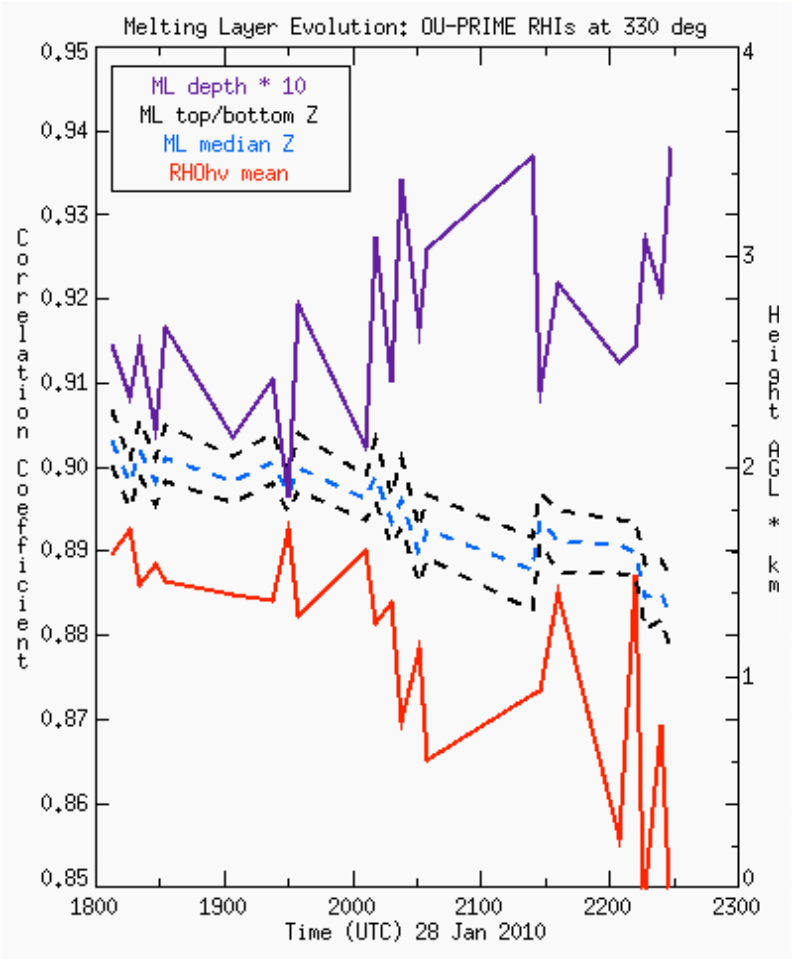

Fig. 4.12. Time evolution of the melting level depth multiplied by 10 (purple), melting level top/bottom height (black, dashed), melting level median height (blue, dashed) and mean ρ_{HV} of melting level pixels determined by the hydrometeor classification algorithm for OU-PRIME 330° RHIs. Surface precipitation type changed from freezing rain to sleet around 21 UTC.

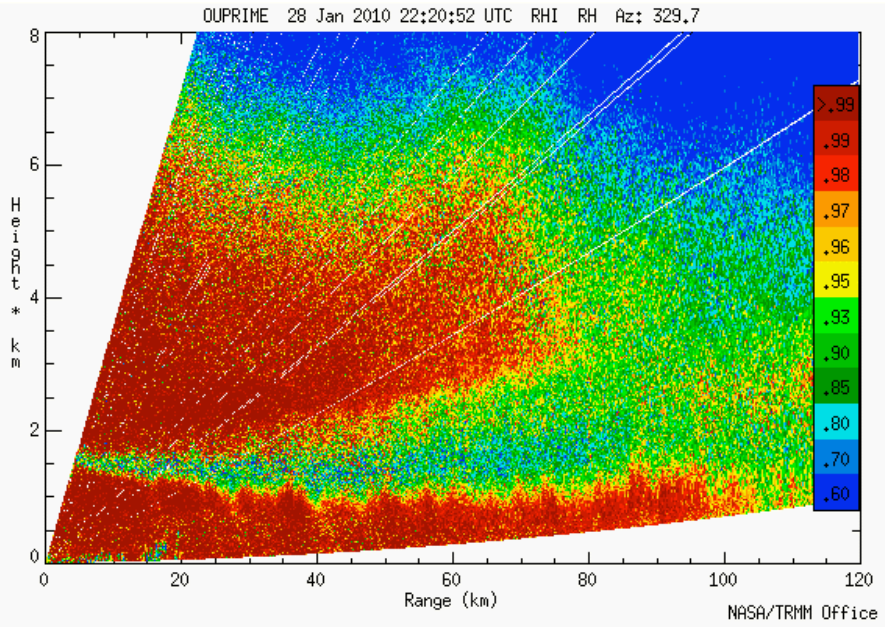

Fig. 4.13. OU-PRIME vertical cross section scan of ρ_{HV} about 1 hour after the transition from freezing rain to sleet at the surface.

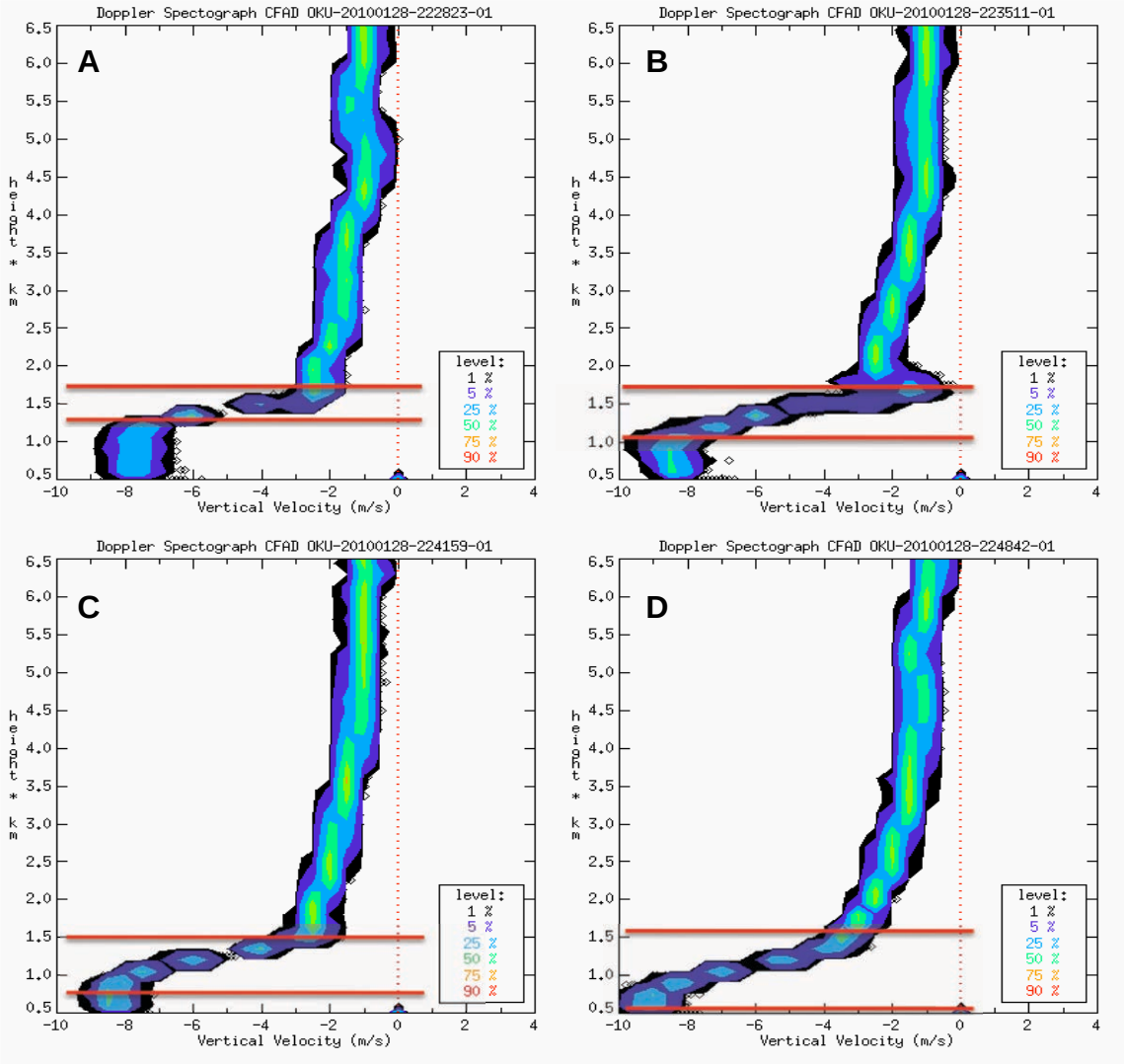

Fig. 4.14. Contoured Frequency by Altitude Diagrams (CFAD) of vertical velocity (w) from vertically-pointing OU-PRIME scans as the melting layer decended and surface precipitation changed from freezing rain to sleet. Frequency levels (%) of w are contoured on top of individual data points (circles). $w = 0$ m s^{-1} shown by red dashed line; $w > 0$ m s^{-1} for updrafts; $w < 0$ m s^{-1} for fall speeds. Red solid lines indicate approximate depth over which fall speeds increase due to hydrometeor melting.

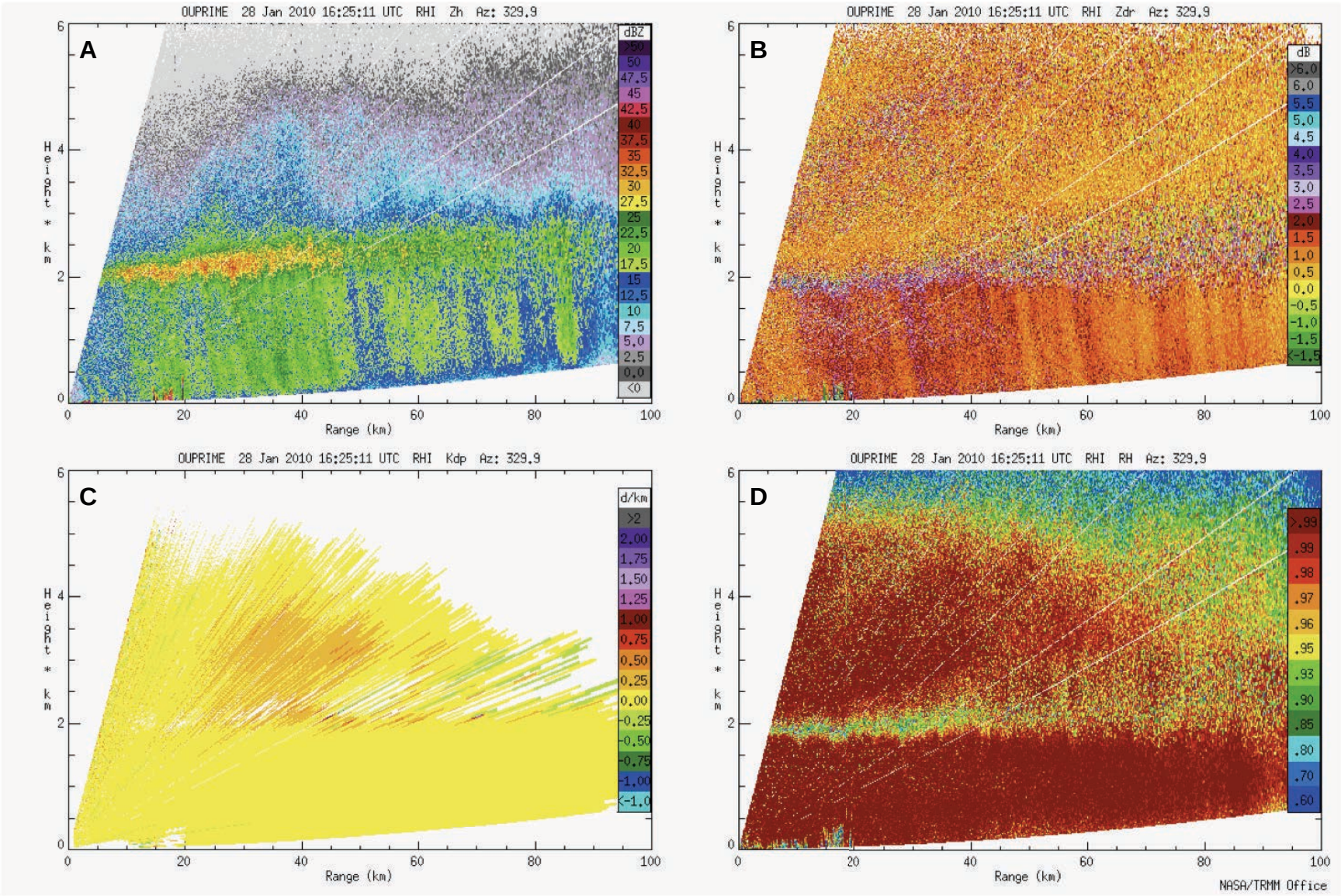

Fig. 4.15. OU-PRIME vertical cross section scan of Z_H (a), Z_{DR} (b), K_{DP} (c), and ρ_{HV} (d) when freezing rain was reported at the surface.

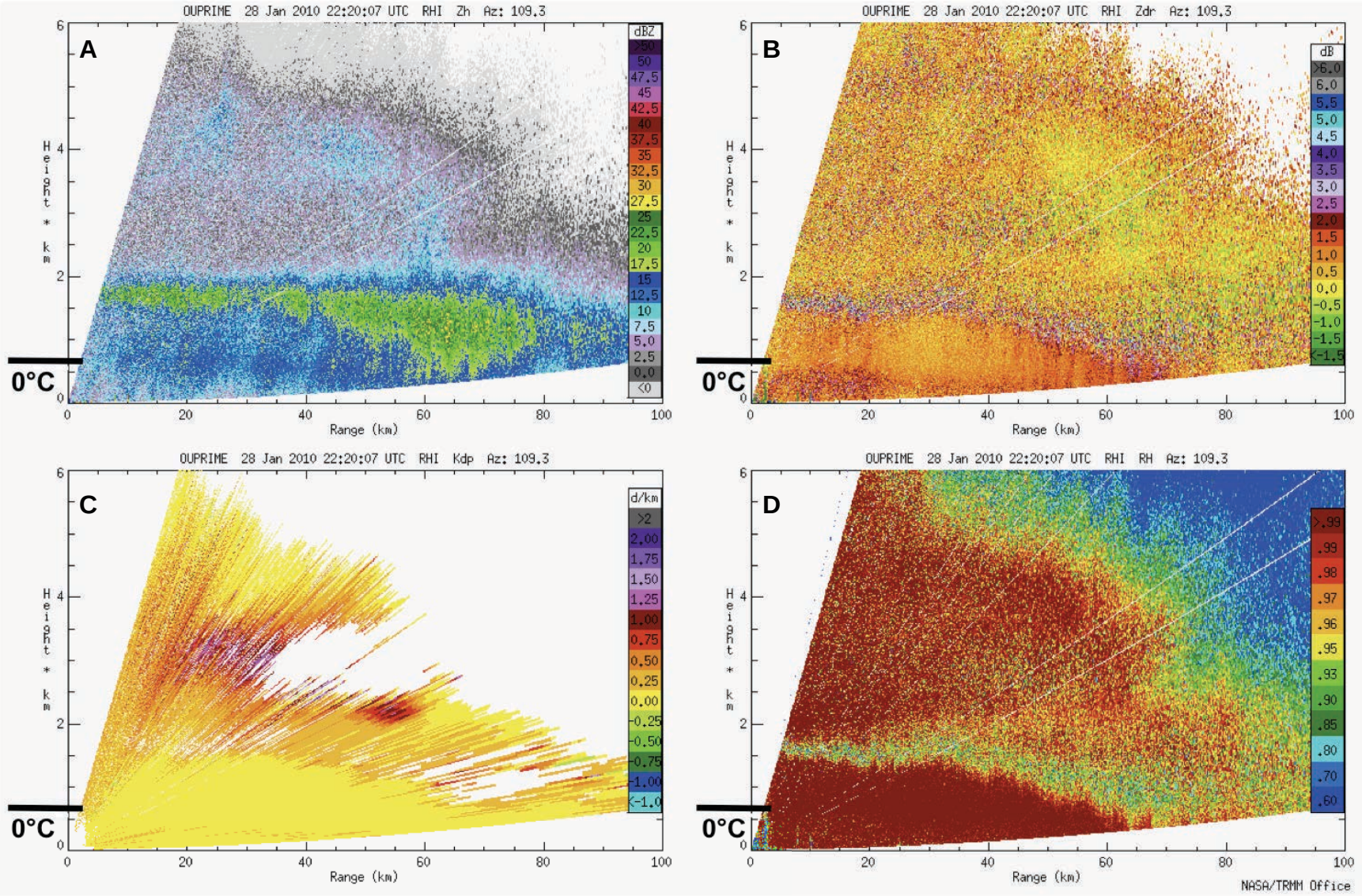

Fig. 4.16. OU-PRIME vertical cross section scan of Z_H (a), Z_{DR} (b), K_{DP} (c), and ρ_{HV} (d) when sleet was reported at the surface with 21 UTC KOUN sounding isotherms.

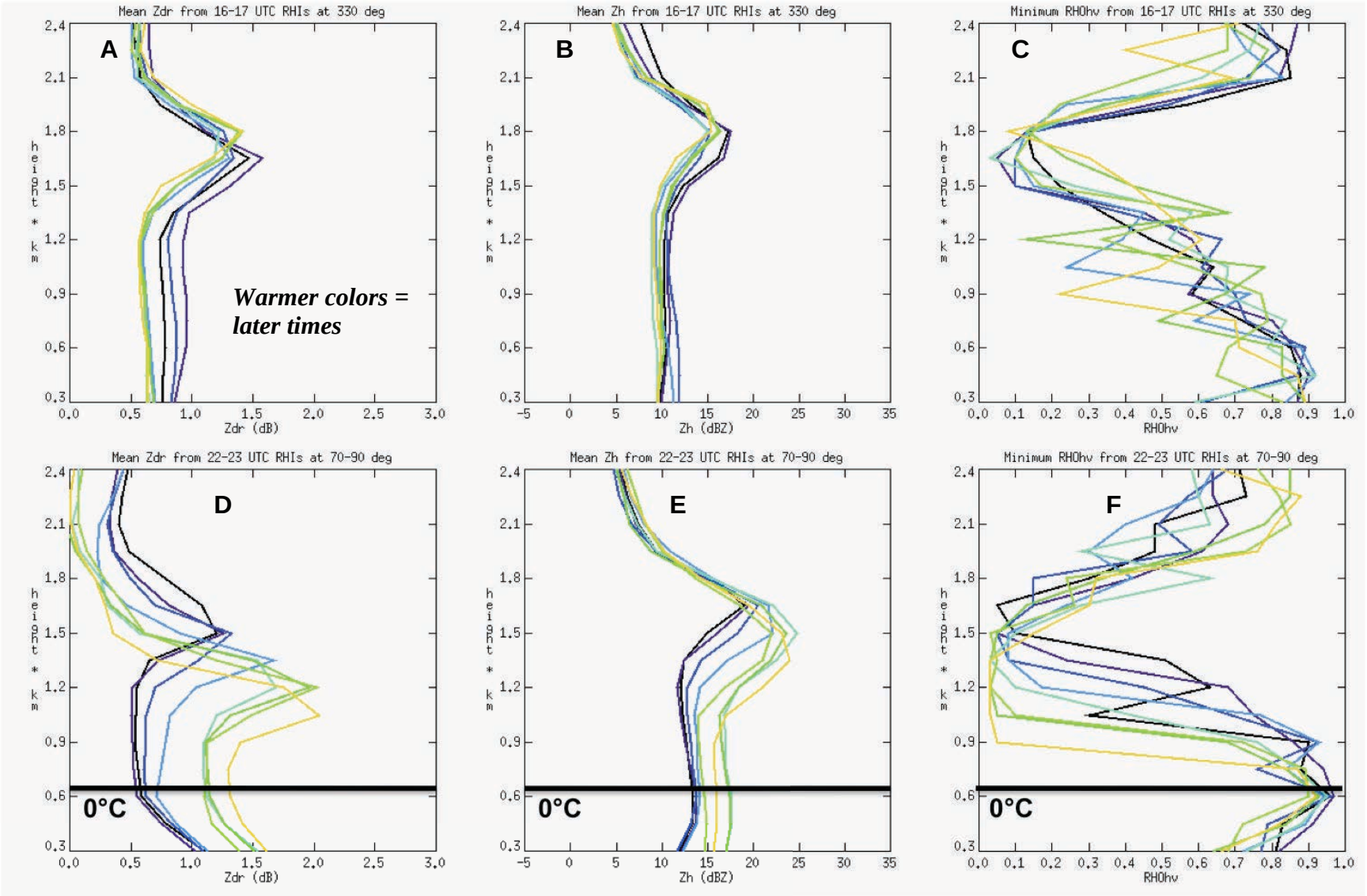

Fig. 4.17. Vertical trends of mean Z_{DR} (a, d), mean Z_H (b, e), and minimum ρ_{HV} (c, f) along particular RHI azimuths during hours when stratiform freezing rain (upper panels) or sleet (lower panels) were reported at the surface with 21 UTC KOUN sounding isotherms.

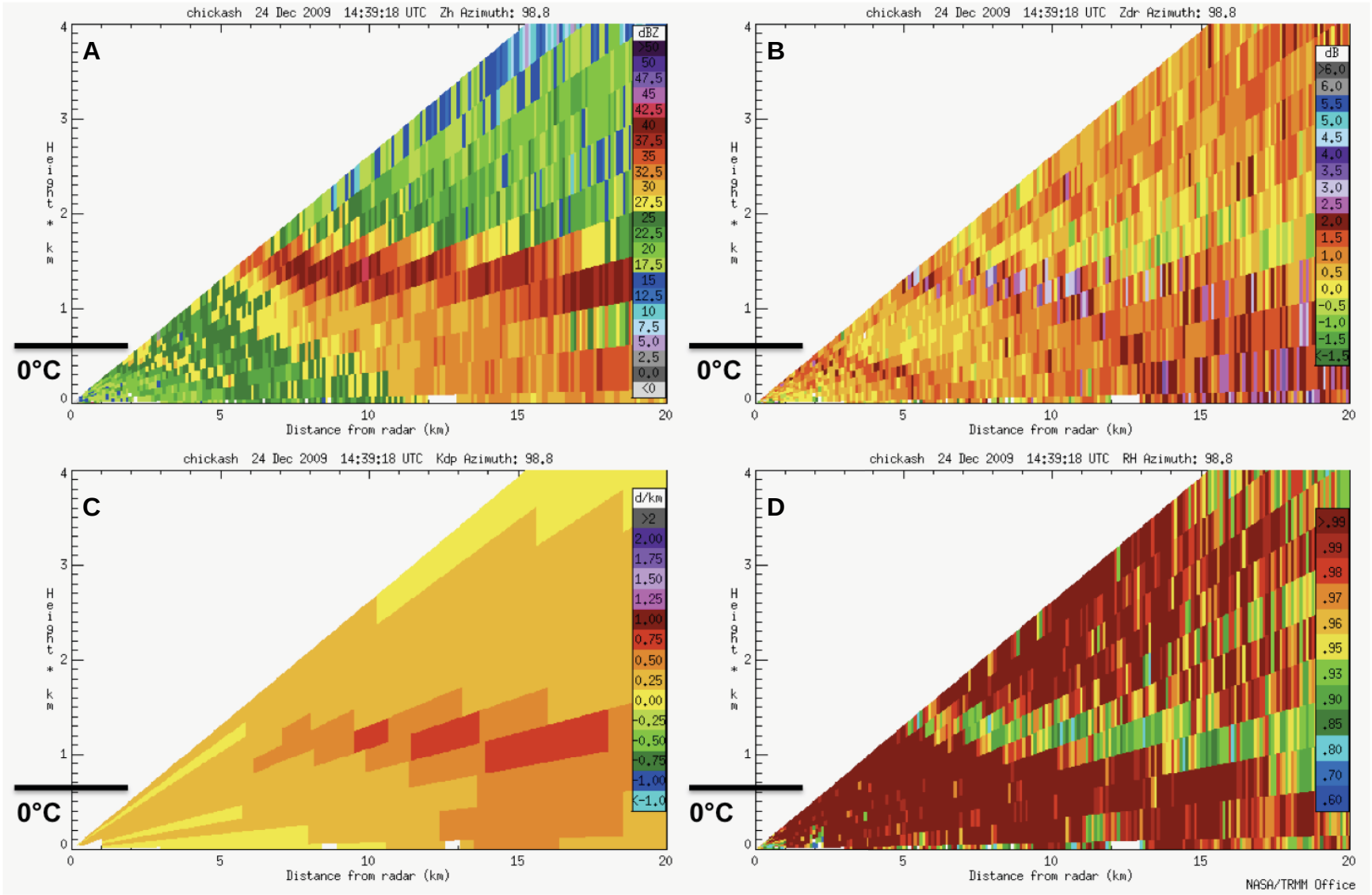

Fig. 4.18. CASA KSAO vertical cross section scan of Z_H (a), Z_{DR} (b), K_{DP} (c), and ρ_{HV} (d) when a refreezing signature was identified within 0-8 km of the radar ahead of the vertical bright band intersecting the ground near 20 km, which was propagating westward. Shown with 12 UTC KOUN sounding isotherms.

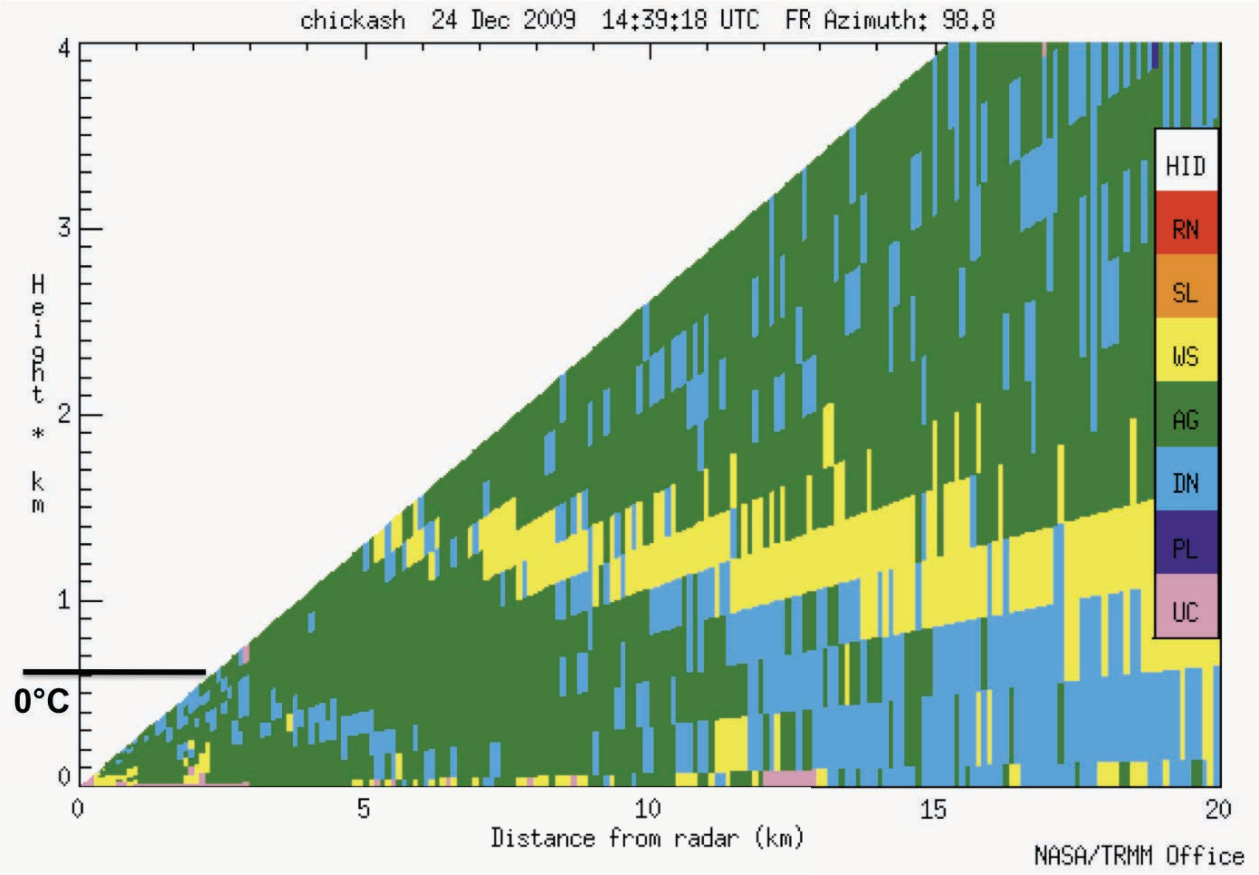

Fig. 4.19. CASA KSAO vertical cross section scan of hydrometeor classification between plates, dendrites, dry aggregated snowflakes, wet snow, and unclassified echo when a refreezing signature was identified within 0-8 km of the radar. Shown with 12 UTC KOUN sounding isotherms. Dendrites are erroneously classified below the melting layer and within the refreezing zone since this version of classification only included frozen and melting hydrometeors.

CHAPTER FIVE

Summary and Conclusions

5.1 Review of winter hydrometeor classification algorithm development and performance at various wavelengths

Despite anomalous propagation, differential attenuation, and some non-Rayleigh scattering effects, this radar-based winter hydrometeor classification algorithm performed well for the C-band OU-PRIME, X- and S-band CSU-CHILL, and X-band CASA IP1 radars. To achieve this, detailed electromagnetic scattering simulations of the most common precipitation types found in winter storms, excluding graupel, were conducted at each wavelength (X-, C-, and S-band) for the first time. Theoretical results from this exercise were used to develop a variable weighting system for the algorithm that capitalizes on the strengths of specific dual-polarimetric variables in differentiating between certain classes of hydrometeors. A melting layer detection algorithm was also implemented, which identifies wet snowflakes without the use of external temperature.

These modifications were applied to the warm-season convective precipitation classification algorithm originally developed by Dolan and Rutledge (2009) to develop a more versatile classification algorithm applicable to winter precipitation. The algorithm was tested on three different winter storms in both Colorado and Oklahoma. It was found that a single hydrometeor classification methodology produced robust results at X-, C-, and S-band for these cold-season, continental precipitation systems. However, the algorithm's performance was slightly more robust and reliable at shorter wavelengths because of its dependence on K_{DP}.

5.2 Hydrometeor classification between pristine and aggregated ice crystals

Dendrites, dry aggregated snow, and wet snow were confidently detected from polarimetric radar variables without the use of external temperature. The melting layer detection algorithm was necessary to constrain rain and sleet below this level. Plate crystals were difficult to discriminate from dendrites based on scattering simulations, and were rarely detected by the algorithm in practice. This could either be because plates do not actually occur very often, were not present in our three case studies, or because these two crystal types are hard to distinguish with radar. More in-situ observations are necessary to validate these findings.

There is motivation to distinguish plates from dendrites because only the latter indicate that the environment is saturated with respect to water. This provides a necessary but insufficient criterion for the existence of super cooled liquid water. Without any reports of supercooled drops or in-situ measurements of temperature and humidity within the cloud, we cannot draw any conclusions about this aircraft-icing hazard within or around the dendritic growth zone. However, this hydrometeor classification algorithm could be used in concert with aircraft observations and cloud radar data to derive a relationship between these two phenomena.

Additionally, prolific aggregation of dendritic crystals (not plates) can enhance surface precipitation rates and delay or prevent complete melting if snowflakes become very large and the temperature inversion is weak (Kennedy and Rutledge 2011, Thériault et al. 2006). The prevalence of semi-melted particles below the melting layer in subfreezing temperatures also promotes the production of ice pellets as opposed to freezing rain, which have drastically different socioeconomic impacts. In this way, the dominant ice crystal habit aloft is very important for discerning the surface precipitation type (Rauber et al. 2001).

5.3 Hydrometeor classification between rain, freezing rain, and sleet

Homogeneous populations of rain, freezing rain, or sleet cannot be distinguished with radar alone because the ranges of expected polarimetric radar (PR) variables derived from electromagnetic scattering simulations significantly overlap. While Z_H, Z_{DR}, and K_{DP} should decrease from rain to freezing rain, and especially from rain to sleet because of the combined effects of decreased density, decreased dielectric factor, and more irregular fall behavior, these lower magnitude PR values could simply be attributed to light rain (Kumjian and Ryzhkov 2010). Freezing rain is only rain that glaciates on the ground, so radar identification of this hydrometeor type is futile. Atmospheric soundings are used in this algorithm to indicate whether freezing rain or sleet might be *possible* where T < 0°C below the melting layer.

However, observations from this study document that a dual-polarized radar with high spatial resolution can accurately identify the transition from liquid drops to ice pellets. Persistent, robust ρ_{HV}, Z_{DR}, and Z_H patterns occur in a horizontally oriented fashion just above the ground. These signatures extend over the exact depth of the surface cold layer indicated by atmospheric soundings only during times when sleet is reported by automated surface observing stations (ASOS). K_{DP} did not exhibit persistent meaningful trends in this region, but sometimes showed a positive enhancement where Z_{DR} also increased. A finer-scale K_{DP} calculation methodology is needed to capture the true refreezing trend of this variable.

It is hypothesized that this refreezing signature is produced by a modulation of the drop size distribution such that smaller drops freeze into ice pellets first (Thériault et al. 2006). The diversity between large, oblate, liquid drops and small, ice pellets could create the noticeable reduction in ρ_{HV}. Since these frozen particles will have slightly lower density, a lower dielectric factor, and will tumble as they fall, their contribution to Z_{DR} and Z_H may be effectively masked in

the presence of the larger, unfrozen particles which primarily determine Z_H and Z_{DR}. Ice pellets can grow both by refreezing of individual drops as well as collisions between ice pellets with nearby supercooled liquid drops. The latter process leads to a local reduction in total number concentration (Thériault et al. 2010). Combined with the lower dielectric factor of ice, this may help explain the reduction in Z_H often seen below the initial Z_H maximum as well as the relatively low magnitude change in Z_H altogether. ρ_{HV} and Z_{DR} are independent of number concentration so their trends are observed to continue toward the surface so long as the freezing induced size-sorting process continues. These refreezing signature hypotheses should be tested with a bin microphysical model, in-situ observations, and more detailed electromagnetic scattering simulations. More detailed analysis of other mixed-winter precipitation systems should be conducted to determine whether the refreezing signature tends to precede, coincide, or appear after sleet is reported at the ground.

5.4 Melting layer variability during transition from freezing rain to sleet

Fall speed spectra from vertically pointing radars and the melting layer detection algorithm for scanning radars both captured the melting layer variability during the transition from freezing rain to sleet. With higher spatiotemporal resolution than soundings or model output, these radar analysis methods helped reveal the production of a deep isothermal layer due to microscale latent heating/cooling effects (Stewart et al. 1992, Heymsfield et al. 2004). Vertical bright band structures, associated with a surface precipitation type transition where the melting layer intersects the ground, were also frequently observed. These melting layer trends could be used as indicators of microphysical processes in a more sophisticated hydrometeor classification algorithm or at least consulted in a nowcasting decision process.

5.5 Suggestions for future algorithm development and applications

A more advanced hydrometeor classification algorithm with two-dimensional membership beta functions (Zrnic et al. 2001) and texture fields (Ryzhkov et al. 2005) that emphasize the spatial variability of dual-polarimetric fields could improve the automatic detection of wet snow and is most likely necessary to automatically detect the refreezing process. In addition to the suggestions already presented, planned future work with this algorithm includes the development of a graupel category as well as testing during lake-effect snowstorms with the Valparaiso University C-band polarimetric radar and cases when plate crystals were known to occur. These next steps would improve the algorithm for applications in the operational sector. Methodologies developed here can also be applied to a multiple-wavelength hydrometeor classification algorithm for radars that operate simultaneously at more than one frequency and for various radars that are collocated. X-band radars are more prone to attenuation as well as non-Rayleigh scattering effects and cannot sense hydrometeors at as far ranges from the radar as S-band systems. However, shorter wavelength radars are more sensitive to meteorological fluctuations in the differential propagation phase and therefore the specific differential phase. For these reasons, a dual-wavelength HCA would help capitalize on the strengths of each operating frequency demonstrated in this thesis and previous studies.

Furthermore, the horizontal wind fields from the CASA radars could be used in a triple-Doppler wind synthesis to derive vertical velocities in clouds with and without organized regions of dendrites (Dolan and Rutledge 2010). This could possibly help verify whether a critical updraft speed is necessary for prolific dendritic crystal growth (Auer and White 1982, Rauber and Tokay 1991). The subtle updrafts within the dendritic growth zone could also be studied with vertically pointing radar data when the ascending velocity exceeds crystal terminal velocity.

Finally, information about the distributions and frequencies of various hydrometeor types gained from this algorithm could be used in the future to enhance ice water content calculations, quantitative precipitation estimation, and numerical modeling parameterizations (Vivekanandan et al. 1994, Mitchell 1996, Cotton et al. 2011).

REFERENCES

Aden, A.L., M. Kerker, 1951: Scattering of Electromagnetic Waves from Two Concentric Spheres. *J. Appl. Phys*. **22**: 1242-1246.

Andsager, K., K.V. Beard, N.F. Laird, 1999: Laboratory Measurements of Axis Ratios for Large Raindrops. *J. Atmos. Sci.*, **56**, 2673–2683.

Auer, A.H., D.L. Veal, 1970: The Dimension of Ice Crystals in Natural Clouds. *J. Atmos. Sci.*, **27**, 919–926.

Auer, A.H., Jr., and J.M. White, 1982: The Combined Role of Kinematics, Thermodynamics and Cloud Physics Associated with Heavy Snowfall Episodes. *Journal of the Meteorological Society of Japan*, **60(1),** 500-507.

Austin, P.M., A.C. Bemis, 1950: A QUANTITATIVE STUDY OF THE "BRIGHT BAND" IN RADAR PRECIPITATION ECHOES. *J. Meteor.*, **7**, 145–151.

Bader, M. J., S.A. Clough, G.P. Cox, 1987: Aircraft and dual polarization radar observations of hydrometeors in light stratiform precipitation. *Q.J.R. Meteorol. Soc*., **113**: 491–515.

Balakrishnan, N., D.S. Zrnic, 1990: Use of Polarization to Characterize Precipitation and Discriminate Large Hail. *J. Atmos. Sci*., **47**, 1525–1540.

Barber, P., and C. Yeh, 1975: Scattering of electromagnetic waves by arbitrary shaped dielectric bodies, *Appl. Opt.*, **14**, 2864-1872

Barthazy, E., W. Henrich, A. Waldvogel, 1988: Size distribution of hydrometeors through the melting layer, *Atmospheric Research*, **47–48**,193-208.

Baumgardner, D., and Coauthors, 2012: In Situ, Airborne Instrumentation: Addressing and Solving Measurement Problems in Ice Clouds. *Bull. Amer. Meteor. Soc.*, **93**, ES29–ES34.

Beard, K.V., A.R. Jameson, 1983: Raindrop Canting. *J. Atmos. Sci.*, **40**, 448–454.

Beard, K.V., C.Chuang, 1987: A new model for the equilibrium shape of raindrops. *J. Atmos. Sci*., **44**, 1509–1524.

Boodoo, S., D. Hudak, N. Donaldson, M. Leduc, 2010: Application of Dual-Polarization Radar Melting-Layer Detection Algorithm. *J. Appl. Meteor. Climatol.*, **49**, 1779–1793.

Brandes, E.A., K. Ikeda, 2004: Freezing-Level Estimation with Polarimetric Radar. *J. Appl. Meteor.*, **43**, 1541–1553.

Brandes, E.A., K. Ikeda, G. Zhang, M. Schönhuber, R.M. Rasmussen, 2007: A Statistical and Physical Description of Hydrometeor Distributions in Colorado Snowstorms Using a Video Disdrometer. *J. Appl. Meteor. Climatol.*, **46**, 634–650.

Bringi, V. N., and V. Chandrasekar, 2001: *Polarimetric Doppler Weather Radar: Principles and Applications*. Cambridge University Press, 636 pp.

Bringi, V. N., Gwo-Jong Huang, V. Chandrasekar, E. Gorgucci, 2002: A Methodology for Estimating the Parameters of a Gamma Raindrop Size Distribution Model from Polarimetric Radar Data: Application to a Squall-Line Event from the TRMM/Brazil

Campaign. *J. Atmos. Oceanic Technol.*, **19**, 633–645.

Bringi, V.N., V. Chandrasekar, D. Zrnić, C. W. Ulbrich, 2003: Comments on "The Need to Represent Raindrop Size Spectra as Normalized Gamma Distributions for the Interpretation of Polarization Radar Observations". *J. Appl. Meteor.*, **42**, 1184–1189.

Bringi, V.N., V. Chandrasekar, J. Hubbert, E. Gorgucci, W.L. Randeu, M. Schoenhuber, 2003: Raindrop Size Distribution in Different Climatic Regimes from Disdrometer and Dual-Polarized Radar Analysis. *J. Atmos. Sci.*, **60**, 354–365.

Boucher, R.J., J.G. Wieler, 1985: Radar Determination of Snowfall Rate and Accumulation. *J. Climate Appl. Meteor.*, **24**, 68–73.

Carey, L.D., and S.A. Rutledge, 1998: Electrical and multiparameter radar observations of a severe hailstorm, *J. Geophys. Res.*, 103(D12), **13**, 979–14,000.

Carey, L.D. and S.A. Rutledge, 2000: The relationship between precipitation and lightning in tropical island convection: A C-band polarimetric radar study. *Mon. Wea. Rev.*, **128**, 2687-2710.

Cifelli, R., W.A. Petersen, L.D. Carey, S.A. Rutledge, and M.A.F. da Silva Dias, 2002: Radar observations of the kinematic, microphysical, and precipitation characteristics of two MCSs in TRMM LBA. *J. Geophys. Res.*, **107**, Doi: 10.1029/2000JD0000264.

Chandrasekar, V., R. Keränen, S. Lim, D. Moisseev, 2011: Recent advances in classification of observations from dual polarization weather radars. *Atmospheric Research*, Available online 14 September 2011, ISSN 0169-8095, 10.1016/j.atmosres.2011.08.014. (http://www.sciencedirect.com/science/article/pii/S0169809511002821)

Cortinas Jr., J.V., B.C. Bernstein, C.C. Robbins, J.W. Strapp, 2004: An Analysis of Freezing Rain, Freezing Drizzle, and Ice Pellets across the United States and Canada: 1976–90. *Wea. Forecasting*, **19**, 377–390.

Cotton, W.R., G.H. Bryan and S.C. van den Heever, 2011: *Storm and Cloud Dynamics*, 2nd Ed., Oxford, Elsevier Academic Press, 809 pp.

Davies-Jones, R.P., 1979: Dual-Doppler Radar Coverage Area as a Function of Measurement Accuracy and Spatial Resolution. *J. Appl. Meteor.*, **18**, 1229–1233.

Depue, T.K., P.C. Kennedy, S.A. Rutledge, 2007: Performance of the Hail Differential Reflectivity (HDR) Polarimetric Radar Hail Indicator. *J. Appl. Meteor. Climatol.*, **46**, 1290–1301.

Dolan, B., S.A. Rutledge, 2009: A Theory-Based Hydrometeor Identification Algorithm for X-Band Polarimetric Radars. *J. Atmos. Oceanic Technol.*, **26**, 2071–2088.

Dolan, B., S.A. Rutledge, 2010: Using CASA IP1 to Diagnose Kinematic and Microphysical Interactions in a Convective Storm. *Mon. Wea. Rev.*, **138**, 1613–1634.

Dolan, B., S.A. Rutledge, S. Lim, V. Chandrasekar, M. Thurai, *submitted*: A Robust C-band Hydrometeor Algorithm and Application to a Long Term Polarimetric Radar Dataset. *Mon. Wea. Rev., submitted.*

Elmore, K.L., 2011: The NSSL Hydrometeor Classification Algorithm in Winter Surface

Precipitation: Evaluation and Future Development. *Wea. Forecasting*, **26**, 756–765.

Evans, K.F. and J. Vivekanandan, 1990: Multiparameter radar and microwave radiative transfer modeling of nonspherical atmospheric ice particles, *IEEE Trans. Geosci. and Remote Sens.,* **28**,423-437.

Fabry, F., W. Szyrmer, 1999: Modeling of the Melting Layer. Part II: Electromagnetic. *J. Atmos. Sci.*, **56**, 3593–3600.

Foster, T.C., J. Hallett, 2008: Enhanced alignment of plate ice crystals in a non-uniform electric field, *Atmospheric Research,* **90(1),** 41-53.

Fujiyoshi, Y., G. Wakahama, 1985: On Snow Particles Comprising an Aggregate. *J. Atmos. Sci.*, **42**, 1667–1674.

Fujiyoshi, Y., 1986: Melting Snowflakes. *J. Atmos. Sci.*, **43**, 307–311.

Fukuta, N., T. Takahashi, 1999: The Growth of Atmospheric Ice Crystals: A Summary of Findings in Vertical Supercooled Cloud Tunnel Studies. *J. Atmos. Sci.*, **56**, 1963–1979.

Giangrande, S.E., A.V. Ryzhkov, 2005: Calibration of Dual-Polarization Radar in the Presence of Partial Beam Blockage. *J. Atmos. Oceanic Technol.*, **22**, 1156–1166.

Giangrande, S.E., J.M. Krause, A.V. Ryzhkov, 2008: Automatic Designation of the Melting Layer with a Polarimetric Prototype of the WSR-88D Radar. *J. Appl. Meteor. Climatol.*, **47**, 1354–1364.

Gibson, S.R., R.E. Stewart, 2007: Observations of ice pellets during a winter storm, *Atmospheric Research,* **85(1),** 64-76.

Gibson, S. R., R. E. Stewart, and W. Henson, 2009: On the variation of ice pellet characteristics, *J. Geophys. Res*., **114**, D09207

Gunn, K.L.S. and T.W.R. East, 1954: The microwave properties of precipitation particles. *Q.J.R. Meteorol. Soc*., **80**: 522–545.

Hendry, A., G.C. McCormick, B.L. Barge, 1976: The Degree of Common Orientation of Hydrometeors Observed by Polarization Diversity Radars. *J. Appl. Meteor.*, **15**, 633–640.

Herzegh, P.H., A.R. Jameson, 1992: Observing Precipitation through Dual-Polarization Radar Measurements. *Bull. Amer. Meteor. Soc.*, **73**, 1365–1374.

Heymsfield, A., 1972: Ice Crystal Terminal Velocities. *J. Atmos. Sci.*, **29**, 1348–1357.

Heymsfield, A.J., A. Bansemer, C. Schmitt, C. Twohy, M.R. Poellot, 2004: Effective Ice Particle Densities Derived from Aircraft Data. *J. Atmos. Sci.*, **61**, 982–1003.

Hogan, R.J., A.J. Illingworth, H. Sauvageot, 2000: Measuring Crystal Size in Cirrus Using 35- and 94-GHz Radars. *J. Atmos. Oceanic Technol.*, **17**, 27–37.

Holroyd, III, E. W., 1971: The meso- and microscale structure of Great Lakes snowstorm bands: A synthesis of ground measurements, radar data, and satellite observations. Ph.D. dissertation, State University of New York at Albany, 148 pp.

Hubbert, J., V.N. Bringi, 1995: An Iterative Filtering Technique for the Analysis of Copolar Differential Phase and Dual-Frequency Radar Measurements. *J. Atmos. Oceanic Technol.*, **12**, 643–648.

Illingworth, A.J., J. W. F. Goddard, and S.M. Cherry, 1987: Polarization radar studies of precipitation development in convective storms. *Q.J.R. Meteorol. Soc.*, **113**: 469–489.

Illingworth, A.J., I. J. Caylor, 1989: Polarization Radar Estimates of Raindrop Size Spectra and Rainfall Rates. *J. Atmos. Oceanic Technol.*, **6**, 939–949.

Jameson, A. R., 1983: Microphysical Interpretation of Multi-Parameter Radar Measurements in Rain. Part I: Interpretation of Polarization Measurements and Estimation of Raindrop Shapes. *J. Atmos. Sci.*, **40**, 1792–1802.

Jiusto, J. E., H. K. Weickmann, 1973: Types of Snowfall. *Bull. Amer. Meteor. Soc.*, **54**, 1148–1162.

Junyent, F., V. Chandrasekar, D. McLaughlin, E. Insanic, N. Bharadwaj, 2010: The CASA Integrated Project 1 Networked Radar System. *J. Atmos. Oceanic Technol.*, **27**, 61–78.

Kajikawa, M., 1982: Observations of the falling motion of early snowflakes. Part I: Relationship between the free-fall pattern and the number and shape of component snow crystals. *J. Meteor. Soc. Japan*, **60**, 797–803.

Keenan, T. D., L. D. Carey, D. S. Zrnić, P. T. May, 2001: Sensitivity of 5-cm Wavelength Polarimetric Radar Variables to Raindrop Axial Ratio and Drop Size Distribution. *J. Appl. Meteor.*, **40**, 526–545.

Kennedy, P.C., S.A. Rutledge, W.A. Petersen, V.N. Bringi, 2001: Polarimetric Radar Observations of Hail Formation. *J. Appl. Meteor.*, **40**, 1347–1366.

Kennedy, P.C., S.A. Rutledge, 2011: S-Band Dual-Polarization Radar Observations of Winter Storms. *J. Appl. Meteor. Climatol.*, **50**, 844–858.

Knight, C.A., N.C. Knight, 1970: The Falling Behavior of Hailstones. *J. Atmos. Sci.*, **27**, 672–681.

Knight, C.A., 1979: Observations of the Morphology of Melting Snow. *J. Atmos. Sci.*, **36**, 1123–1130.

Kouketsu, T. and H. Uyeda, 2010: Validation of Hydrometeor Classification Method for X-band Polarimetric Radar – Comparison with Ground Observation of Solid Hydrometeor, Preprints, , Sibiu, Romania, *6th European Conference on Radar in Meteorology and Hydrology*

Kumjian, M.R., A.V. Ryzhkov, 2008: Polarimetric Signatures in Supercell Thunderstorms. *J. Appl. Meteor. Climatol.*, **47**, 1940–1961.

Kumjian, M.R., A.V. Ryzhkov, 2010: The Impact of Evaporation on Polarimetric Characteristics of Rain: Theoretical Model and Practical Implications. *J. Appl. Meteor. Climatol.*, **49**, 1247–1267.

León, L., V.N. Bringi and B. Dolan, 2011: Wet Ice Specific Attenuation Retrieval and Correction for X-band using a Piece-wise Forward Correction Method. Preprints, *35th Conf. on Radar Meteorology*, Pittsburg, PA, Amer. Meteor. Soc., P3.26 [Available online at https://ams.confex.com/ams/35Radar/webprogram/Paper191470.html]

Liu, H., V. Chandrasekar, 2000: Classification of Hydrometeors Based on Polarimetric Radar Measurements: Development of Fuzzy Logic and Neuro-Fuzzy Systems, and In Situ

Verification. *J. Atmos. Oceanic Technol.*, **17**, 140–164.

Lo, K.K., R.E. Passarelli, 1982: The Growth of Snow in Winter Storms:. An Airborne Observational Study. *J. Atmos. Sci.*, **39**, 697–706.

Locatelli, J.D., and P.V. Hobbs (1974), Fall Speeds and Masses of Solid Precipitation Particles, *J. Geophys. Res.*, **79(15),** 2185–2197.

Magono, C., and T. Nakamura, 1965: Aerodynamic studies of falling snowflakes. *J. Meteor. Soc. Japan*, **43**, 139–147.

Matrosov, S.Y., R.F. Reinking, I.V. Djalalova, 2005: Inferring Fall Attitudes of Pristine Dendritic Crystals from Polarimetric Radar Data. *J. Atmos. Sci.*, **62**, 241–250.

Matrosov, S. Y., R.Cifelli, P.C. Kennedy, S.W. Nesbitt, S.A. Rutledge, V. N. Bringi, B.E. Martner, 2006: A Comparative Study of Rainfall Retrievals Based on Specific Differential Phase Shifts at X- and S-Band Radar Frequencies. *J. Atmos. Oceanic Technol.*, **23**, 952–963.

Matrosov, S.Y., G.G. Mace, R. Marchand, M.D. Shupe, A.G. Hallar, I.B. McCubbin, 2012: Observations of Ice Crystal Habits with a Scanning Polarimetric W-Band Radar at Slant Linear Depolarization Ratio Mode. *J. Atmos. Oceanic Technol.*, **29**, 989–1008.

McLaughlin, D., and Coauthors, 2009: Short-Wavelength Technology and the Potential For Distributed Networks of Small Radar Systems. *Bull. Amer. Meteor. Soc.*, **90**, 1797–1817.

Mitchell, D.L., 1996: Use of Mass- and Area-Dimensional Power Laws for Determining Precipitation Particle Terminal Velocities. *J. Atmos. Sci.*, **53**, 1710–1723.

Moismann L., 1995: An improved method for determining the degree of snow crystal riming by vertical Doppler radar. *Atmos. Res*., **37**, 305-323.

Nygaard, K., B. Egil, J.E. Kristjánsson, L. Makkonen, 2011: Prediction of In-Cloud Icing Conditions at Ground Level Using the WRF Model. *J. Appl. Meteor. Climatol.*, **50**, 2445–2459.

Ohtake, T. and T. Henmi, 1970: Radar reflectivity of aggregated snowflakes. *Proc. of the 14th Conf. on Radar Meteorology*, 209–210.

Park, Hyang Suk, A.V. Ryzhkov, D.S. Zrnić, Kyung-Eak Kim, 2009: The Hydrometeor Classification Algorithm for the Polarimetric WSR-88D: Description and Application to an MCS. *Wea. Forecasting*, **24**, 730–748.

Pruppacher, H.R., R.L. Pitter, 1971: A Semi-Empirical Determination of the Shape of Cloud and Rain Drops. *J. Atmos. Sci.*, **28**, 86–94.

Pruppacher, H.R., and J.D. Klett, 1997: *Microphysics of Clouds and Precipitation*, 2nd Ed., Kluwer Academic Publishers, Dordereht, The Netherlands, 954 pp.

Ralph, F.M., and Coauthors, 2005: Improving Short-Term (0–48 h) Cool-Season Quantitative Precipitation Forecasting: Recommendations from a USWRP Workshop. *Bull. Amer. Meteor. Soc.*, **86**, 1619–1632.

Rauber, R.M., A. Tokay, 1991: An Explanation for the Existence of Supercooled Water at the Top of Cold Clouds. *J. Atmos. Sci.*, **48**, 1005–1023.

Rauber, R.M., L.S. Olthoff, M.K. Ramamurthy, K.E. Kunkel, 2001: Further Investigation of a Physically Based, Nondimensional Parameter for Discriminating between Locations of Freezing Rain and Ice Pellets. *Wea. Forecasting*, **16**, 185–191.

Reinking, R.F., 1975: Formation of Graupel. *J. Appl. Meteor.*, **14**, 745–754.

Rhinehart, R.E., 2004: *Radar for Meteorologists*, 4th Ed., Rhinehart Publications, Nevada, MO, 482 pp.

Ryan, B.F., 2000: A Bulk Parameterization of the Ice Particle Size Distribution and the Optical Properties in Ice Clouds. *J. Atmos. Sci.*, **57**, 1436–1451.

Ryzhkov, A.V., D.S. Zrnic, B.A. Gordon, 1998: Polarimetric Method for Ice Water Content Determination. *J. Appl. Meteor.*, **37**, 125–134.

Ryzhkov, A.V., D.S. Zrnic, 1998: Discrimination between Rain and Snow with a Polarimetric Radar. *J. Appl. Meteor.*, **37**, 1228–1240.

Ryzhkov, A.V., D.S. Zrnic, 1998: Polarimetric Rainfall Estimation in the Presence of Anomalous Propagation. *J. Atmos. Oceanic Technol.*, **15**, 1320–1330.

Ryzhkov, A.V., 2001: Interpretation of Polarimetric Radar Covariance Matrix for Meteorological Scatterers: Theoretical Analysis. *J. Atmos. Oceanic Technol.*, **18**, 315–328.

Ryzhkov, A.V., T.J. Schuur, D.W. Burgess, P.L. Heinselman, S.E. Giangrande, D.S. Zrnic, 2005: The Joint Polarization Experiment: Polarimetric Rainfall Measurements and Hydrometeor Classification. *Bull. Amer. Meteor. Soc.*, **86**, 809–824.

Ryzhkov, A.V., S.E. Giangrande, V.M. Melnikov, T.J. Schuur, 2005: Calibration Issues of Dual-Polarization Radar Measurements. *J. Atmos. Oceanic Technol.*, **22**, 1138–1155.

Ryzhkov, A.V., 2007: The Impact of Beam Broadening on the Quality of Radar Polarimetric Data. *J. Atmos. Oceanic Technol.*, **24**, 729–744.

Schuur, T.J., H. Park, A.V. Ryzhkov, H.D. Reeves, 2012: Classification of Precipitation Types during Transitional Winter Weather Using the RUC Model and Polarimetric Radar Retrievals. *J. Appl. Meteor. Climatol.*, **51**, 763–779.

Seliga, T. A., V.N. Bringi, 1976: Potential Use of Radar Differential Reflectivity Measurements at Orthogonal Polarizations for Measuring Precipitation. *J. Appl. Meteor.*, **15**, 69–76.

Smith, W.L., P. Minnis, C. Fleeger, D. Spangenberg, R. Palikonda, L. Nguyen, 2012: Determining the Flight Icing Threat to Aircraft with Single-Layer Cloud Parameters Derived from Operational Satellite Data. *J. Appl. Meteor. Climatol.*, **51**, 1794–1810.

Spek, A.L. J., C.M. H. Unal, D.N. Moisseev, H. W. J. Russchenberg, V. Chandrasekar, Y. Dufournet, 2008: A New Technique to Categorize and Retrieve the Microphysical Properties of Ice Particles above the Melting Layer Using Radar Dual-Polarization Spectral Analysis. *J. Atmos. Oceanic Technol.*, **25**, 482–497.

Spengler, J.D., N.R. Gokhale, 1972: Freezing of Freely Suspended, Supercooled Water Drops in a Large Vertical Wind Tunnel. *J. Appl. Meteor.*, **11**, 1101–1107.

Stephens, G.L., 2005: Cloud Feedbacks in the Climate System: A Critical Review. *J. Climate*, **18**, 237–273.

Stewart, R.E., J.D. Marwitz, J.C. Pace, R.E. Carbone, 1984: Characteristics through the Melting Layer of Stratiform Clouds. *J. Atmos. Sci.*, **41**, 3227–3237.

Stewart, R.E., R.W. Crawford, N.R. Donaldson, T.B. Low, B.E. Sheppard, 1990: Precipitation and Environmental Conditions during Accretion in Canadian East Coast Winter Storms. *J. Appl. Meteor.*, **29**, 525–538.

Stewart, R. E., C.A. Lin, S.R. Macpherson, 1990: The Structure of a Winter Storm Producing Heavy Precipitation over Nova Scotia. *Mon. Wea. Rev.*, **118**, 411–426.

Stewart, R.E., 1992: Precipitation Types in the Transition Region of Winter Storms. *Bull. Amer. Meteor. Soc.*, **73**, 287–296.

Straka, J.M., D.S. Zrnić, A.V. Ryzhkov, 2000: Bulk Hydrometeor Classification and Quantification Using Polarimetric Radar Data: Synthesis of Relations. *J. Appl. Meteor.*, **39**, 1341–1372.

Takahashi, T., N. Fukuta, 1988: Observations of the Embryos of Graupel. *J. Atmos. Sci.*, **45**, 3288–3297.

Takahashi, T., T. Tajiri, Y. Sonoi, 1999: Charges on Graupel and Snow Crystals and the Electrical Structure of Winter Thunderstorms. *J. Atmos. Sci.*, **56**, 1561–1578.

Thurai, M., and V.N. Bringi, 2005: Drop axis ratios from 2D video disdrometer, J. Atmos. Oceanic Technol., 22, 966–978

Thériault, J.M., R.E. Stewart, J.A. Milbrandt, and M.K. Yau, 2006: On the simulation of winter precipitation types, *J. Geophys. Res*., **111**, D18202

Thériault, J.M., R.E. Stewart, W. Henson, 2010: On the Dependence of Winter Precipitation Types on Temperature, Precipitation Rate, and Associated Features. *J. Appl. Meteor. Climatol.*, **49**, 1429–1442.

Trapp, R.J., D.M. Schultz, A.V. Ryzhkov, R.L. Holle, 2001: Multiscale Structure and Evolution of an Oklahoma Winter Precipitation Event. *Mon. Wea. Rev.*, **129**, 486–501.

Ulbrich, C.W., 1983: Natural Variations in the Analytical Form of the Raindrop Size Distribution. *J. Climate Appl. Meteor.*, **22**, 1764–1775.

Vivekanandan, J., W.M. Adams, V.N. Bringi, 1991: Rigorous Approach to Polarimetric Radar Modeling of Hydrometeor Orientation Distributions. *J. Appl. Meteor.*, **30**, 1053–1063.

Vivekanandan, J., R. Raghavan, and V.N. Bringi, 1993: Polarimetric radar modeling of mixtures of precipitation particles. *IEEE Transactions on Geoscience and Remote Sensing*, **31,** 1017-1030.

Vivekanandan, J., V.N. Bringi, M. Hagen, and P. Meischner, 1994: Polarimetric radar studies of atmospheric ice particles. *IEEE Transactions on Geoscience and Remote Sensing*, **32,** 1-10.

Waldvogel, A., 1974: The N_0 Jump of Raindrop Spectra. *J. Atmos. Sci.*, **31**, 1067–1078.

Wang, Y., V. Chandrasekar, 2009: Algorithm for Estimation of the Specific Differential Phase. *J. Atmos. Oceanic Technol.*, **26**, 2565–2578.

Waterman, P.C., 1965: "Matrix formulation of electromagnetic scattering," Proceedings of the

IEEE , **vol.53, no.8**, 805- 812.

Williams, R.E., D.J. Smalley, M.F. Donovan, R.G. Hallowell, K.T. Hood, B.J. Bennett, R. Evaristo, A. Stepanek, T. Bals-Elsholz, J. Cobb, and J.M. Ritzman, 2011: Dual-Polarized Radar Winter Storm Studies Supporting Development of NEXRAD-Based Aviation Hazards Products, Preprints, *35th Conf. on Radar Meteorology*, Pittsburg, PA, Amer. Meteor. Soc., P13.302

Willis, P.T., 1984: Functional Fits to Some Observed Drop Size Distributions and Parameterization of Rain. *J. Atmos. Sci.*, **41**, 1648–1661.

Wolde, M., G. Vali, 2001: Polarimetric Signatures from Ice Crystals Observed at 95 GHz in Winter Clouds. Part I: Dependence on Crystal Form. *J. Atmos. Sci.*, **58**, 828–841.

Wolfe, J.P., J.R. Snider, 2012: A Relationship between Reflectivity and Snow Rate for a High-Altitude S-Band Radar. *J. Appl. Meteor. Climatol.*, **51**, 1111–1128.

Yuter, S.E., R.A. Houze, 1995: Three-Dimensional Kinematic and Microphysical Evolution of Florida Cumulonimbus. Part II: Frequency Distributions of Vertical Velocity, Reflectivity, and Differential Reflectivity. *Mon. Wea. Rev.*, **123**, 1941–1963.

Zawadzki, I., F. Fabry, W. Szyrmer, 2001: Observations of supercooled water and secondary ice generation by a vertically pointing X-band Doppler radar, *Atmospheric Research*, **59–60**, 343-359.

Zhang, G., S. Luchs, A.V. Ryzhkov, M. Xue, L. Ryzhkova, Q. Cao, 2011: Winter Precipitation Microphysics Characterized by Polarimetric Radar and Video Disdrometer Observations in Central Oklahoma. *J. Appl. Meteor. Climatol.*, **50**, 1558–1570.

Zrnic, D.S., N. Balakrishnan, C.L. Ziegler, V.N. Bringi, K. Aydin, T. Matejka, 1993: Polarimetric Signatures in the Stratiform Region of a Mesoscale Convective System. *J. Appl. Meteor.*, **32**, 678–693.

Zrnić, D.S., T.D. Keenan, L.D. Carey, P. May, 2000: Sensitivity Analysis of Polarimetric Variables at a 5-cm Wavelength in Rain. *J. Appl. Meteor.*, **39**, 1514–1526.

Zrnić, D.S., A.V. Ryzhkov, J. Straka, Y. Liu, J. Vivekanandan, 2001: Testing a Procedure for Automatic Classification of Hydrometeor Types. *J. Atmos. Oceanic Technol.*, **18**, 892–913.